

ABSTRACT

BERNSTEIN, ANDREW SCOTT. Numerical Techniques for Hydrodynamic and Morphodynamic Modeling. (Under the direction of Alina Chertock).

In this dissertation, we consider numerical techniques for modeling and computationally solving a hydrodynamic system, represented by the system of shallow water equations used to model the flows of coastal areas and rivers, and a morphodynamic system, represented by the shallow water equations with an Exner equation to govern sediment transport. We begin by deriving the equations for both the shallow water system and Exner equation from physical principles, and then we consider a number of formulations one can use to model the movement of sediment within the Exner equation. We then discuss finite volume methods and their use in solving systems of hyperbolic balance laws, particularly the shallow water equations with Exner equation.

In Part I, we implement a second-order central-upwind scheme for the 1-D shallow water equations with discontinuous bottom topography. The scheme is well-balanced, able to exactly numerically preserve a chosen steady state, and positivity preserving, ensuring that the height of the water never becomes negative which represents a non-physical state. This central-upwind scheme relies on a discontinuous piecewise linear reconstruction of the bottom topography function, and, thus, it is suitable for functions when the bottom contains large jumps and can be extended to models with moving, time-dependent bottom topography which will be studied in Part II. We then present the performance of the scheme, demonstrating the numerical scheme remains smooth while handling a small perturbation of steady state and accurately converging to the solution of a Riemann problem with both a unique solution or with multiple solutions.

In Part II, we implement second-order central-upwind schemes for the 1-D shallow water equations with Exner equation. A straightforward implementation of the numerical scheme in Part I, produces diffusive numerical results, leading us to investigate the eigenvalues of the entire system, as the largest and smallest eigenvalues of the system are used in the evolution of the numerical scheme. Our conclusion is that most often the water waves and sediment waves propagate with speeds of different magnitudes, causing numerical diffusion to be produced within the numerical scheme. After determining which eigenvalues are associated with the shallow water equations and which are associated with the Exner equation, we use this information to modify our numerical scheme. These modifications include the use of Strang splitting [81] in the time evolution and a staggered spatial discretization for the numerical representation of the bottom topography. Using a mixture of these modifications with the original numerical scheme, we implement four different numerical schemes. We then present the performance of the numerical schemes and further demonstrate one of the schemes on a number of examples

for various levels of interaction between the water and sediment as well as different speeds for the water flow. The chosen numerical scheme is then extended into two dimensions which we use in numerically solving the 2-D shallow water equations with 2-D Exner equation.

© Copyright 2018 by Andrew Scott Bernstein

All Rights Reserved

Numerical Techniques for Hydrodynamic and Morphodynamic Modeling

by
Andrew Scott Bernstein

A dissertation submitted to the Graduate Faculty of
North Carolina State University
in partial fulfillment of the
requirements for the Degree of
Doctor of Philosophy

Applied Mathematics

Raleigh, North Carolina

2018

APPROVED BY:

Mansoor Haider

Zhilin Li

Tien Khai Nguyen

Alina Chertock
Chair of Advisory Committee

DEDICATION

To my family for all your support, especially for my wife, Amanda.

BIOGRAPHY

Andrew Bernstein was born and raised in Silver Spring, Maryland, a suburb of the Washington D.C. metropolitan area. After graduating from high school, he attended Montgomery College in Rockville, MD, earning an A.S. in Mathematics and Physics. From there he attended the University of Maryland in College Park, MD, earning a B.S. in Mathematics and a B.A. in Economics. He continued his studies in graduate school at North Carolina State University in Raleigh, NC, earning a M.S. in Applied Mathematics and a Ph.D. upon the successful completion of this dissertation.

ACKNOWLEDGEMENTS

I would like to thank my advisor, Dr. Alina Chertock, for all her support and guidance throughout my graduate career. I would also like to thank our collaborators, Dr. Alexander Kurganov for his contributions and insightful discussions as well as Dr. Tong Wu. Thank you to Dr. Gavin Conant, Dr. Mansoor Haider, Dr. Zhilin Li, and Dr. Khai Nguyen for serving on my dissertation committee and for your feedback and time and to the Mathematics Department at NC State for their financial support during my time at State.

Finally, I would like to thank all my family and friends who have supported me throughout my time at State, especially Chris, Tim, Cleveland, Mary, Steven and Luke. Most importantly I would like to thank Amanda, without whom I would not be here. Sitting next to you in Modeling was the best decision I ever made.

TABLE OF CONTENTS

LIST OF TABLES	viii
---------------------------------	-------------

LIST OF FIGURES	ix
----------------------------------	-----------

Chapter 1 INTRODUCTION	1
1.1 Motivation	1
1.2 Shallow Water Equations	2
1.2.1 Derivation of First Equation: Conservation of Mass	3
1.2.2 Derivation of Second and Third Equation: Conservation of Momentum	5
1.2.3 Hyperbolic System of Conservation and Balance Laws	8
1.2.4 Steady States of Shallow Water Equations	9
1.3 Sediment Transport Equation	11
1.3.1 Derivation of Sediment Transport Equation	12
1.3.2 Sediment Transport Formulations	14
1.3.2.1 Du Boys (1879)	15
1.3.2.2 Meyer-Peter-Müller (MPM) (1948)	16
1.3.2.3 Fernandez Luque-VanBeek (FLV) (1976)	17
1.3.2.4 Grass (1981)	17
1.3.2.5 Nielsen (1992)	17
1.3.2.6 Modified Grass (2012)	17
1.4 Finite Volume Methods	18
1.4.1 Alternatives to the Central-Upwind Scheme	22
1.5 1-D Second Order Semi-Discrete Central-Upwind Scheme	22
1.6 2-D Second Order Semi-Discrete Central-Upwind Scheme	24
1.7 Outline of the Dissertation	27

I Hydrodynamic: Shallow Water Equations with Discontinuous Bottom Topography 28

Chapter 2 A Well-Balanced, Positivity Preserving Central-Upwind Scheme for the 1-D Shallow Water System of Equations	29
2.1 A Modified Second-Order Semi-Discrete Central-Upwind Scheme	30
2.1.1 Reconstruction of \mathbf{U}	31
2.1.2 Piecewise Linear Reconstruction of B	32
2.1.3 Local Speeds of Propagation	32
2.2 Well-Balanced Quadrature for the Geometric Source Terms	32
2.3 Positivity Preserving Property	34
2.3.1 Positivity Correction for \tilde{w}	34
2.3.1.1 Velocity Desingularization	35
2.3.2 Time Evolution and the Draining Time-Step	35
2.4 Numerical Examples	36
2.4.1 Example 1—Small Perturbation of Steady State	36

2.4.2	Example 2—Riemann Problem with Unique Solution	37
2.4.3	Example 3—Riemann Problem with Multiple Solutions	39
2.5	Conclusion	39

II Morphodynamic: Exner Equation to Govern Bed Load Sediment Transport 41

Chapter 3	1-D Shallow Water Equations with Exner Equation	42
3.1	Eigenvalues for the Jacobian of the Shallow Water System with Exner Equation	43
3.2	Time Evolution	45
3.2.1	Splitting Approach	46
3.2.2	Non-Splitting Approach	48
3.3	Spatial Discretization	49
3.3.1	Non-Staggered Discretized Grid	49
3.3.2	Staggered Discretized Grid	49
3.4	Numerical Scheme for the Splitting Approach with the Bottom Evolved on a Non-Staggered Discretized Grid (S-NSG)	51
3.4.1	Hydrodynamic Subsystem	51
3.4.2	Morphodynamic Subsystem	53
3.4.3	Time Evolution of S-NSG	54
3.4.3.1	Time Evolution of S-NSG When the Splitting Time-Step Is Chosen Using the Morphodynamic Time-Step (S-NSG-M)	55
3.4.3.2	Time Evolution of S-NSG When the Splitting Time-Step Is Chosen Using the Hydrodynamic Time-Step (S-NSG-H)	56
3.5	Numerical Scheme for the Splitting Approach with the Bottom Evolved on a Staggered Discretized Grid (S-SG)	56
3.5.1	Hydrodynamic Subsystem	57
3.5.2	Morphodynamic Subsystem	59
3.5.3	Time Evolution of S-SG	61
3.5.3.1	Time Evolution of S-SG When the Splitting Time-Step Is Chosen Using the Morphodynamic Time-Step (S-SG-M)	61
3.5.3.2	Time Evolution of S-SG When the Splitting Time-Step Is Chosen Using the Hydrodynamic Time-Step (S-SG-H)	62
3.6	Numerical Scheme for the Non-Splitting Approach with the Bottom Evolved on a Non-Staggered Discretized Grid (NS-NSG)	63
3.6.1	Time Evolution of NS-NSG	65
3.7	Numerical Scheme for the Non-Splitting Approach with the Bottom Evolved on a Staggered Discretized Grid (NS-SG)	65
3.7.1	Time Evolution of NS-SG.	69
3.8	Numerical Examples	69
3.8.1	Example 1 – Comparison of Numerical Formulations	69
3.8.2	Example 2 – Test of Order	70
3.8.3	Example 3 – Sediment Mound Interacting Slowly with the Water Flow . .	72
3.8.4	Example 4 – Sediment Mound Interacting Quickly with the Water Flow .	74

3.8.5	Example 5 – Sediment Mound Interacting Slowly with a Large Velocity Water Flow	75
3.8.6	Example 6 – Small Discontinuity in Sediment Bed	76
3.9	Conclusion	77
Chapter 4 2-D Shallow Water Equations with Exner Equation		79
4.1	Eigenvalues for the Jacobian of the 2D Shallow Water System with Exner Equation	80
4.2	A Modified Second-Order Semi-Discrete Central-Upwind Scheme in Two Dimen- sions	82
4.2.1	Numerical Fluxes	83
4.2.2	Reconstruction	85
4.2.3	Well-Balanced Quadrature for the Geometric Source Terms	86
4.2.4	Local Speeds of Propagation	87
4.2.5	Time Evolution	87
4.3	Numerical Example in 2-D – Evolution of Conical Sediment Dune Interacting Slowly with the Water Flow	87
4.4	Conclusion	90
Chapter 5 Conclusions and Future Work		91
References		93
Appendices		103
Appendix A	Third Order Strong Stability Preserving Runge Kutta Method	104
Appendix B	Adaptive Time Step Strategy	106

LIST OF TABLES

Table 3.1	Example 1: Computation time for various formulations.	72
Table 3.2	Example 2: L^1 Error and Order of Convergence.	72

LIST OF FIGURES

Figure 1.1	Shallow Water Domain.	3
Figure 1.2	Left: Central (staggered) control volume. Right: Upwind control volume. . .	19
Figure 1.3	Central-Upwind Control Volume.	21
Figure 2.1	Example 1: Solution (w) computed by the well-balanced and non-well-balanced central upwind schemes using $N = 400$ (top row) and $N = 1600$ (bottom row) uniform cells. Right column: zoom into the region $x \in [0.395, 0.5]$	38
Figure 2.2	Example 2: Solution (h on the left and u on the right) computed using $\Delta x = 0.004$ and 0.001 and compared with the reference solution.	39
Figure 2.3	Example 3: Solution (h on the left and u on the right) computed by the proposed central-upwind scheme using $\Delta x = 0.004$, 0.001 , and 0.00004	40
Figure 2.4	Example 3: Solution (h on the left and u on the right) computed by the central-upwind scheme from [50] using $\Delta x = 0.004$, 0.001 , and 0.00004	40
Figure 3.1	Non-staggered discretized grid for $\bar{\mathbf{U}}$ and \bar{B}	50
Figure 3.2	Staggered discretized grid consisting of $\bar{\mathbf{U}}$ (blue) centered at the cell center and of \bar{B} (black dashed) centered at the cell interface.	50
Figure 3.3	Example 1: Initial conditions at $t = 0$ with $N = 400$	70
Figure 3.4	Example 1: NS-SG, S-SG-M, and S-SG-H solutions (B) computed using $N = 400$ at $t = 2.1$. Right zoom into the region $x \in [0.8, 1.4]$	71
Figure 3.5	Example 1: NS-NSG, S-NSG-M, and S-NSG-H solutions (B) computed using $N = 400$ at $t = 2.1$. Right zoom into the region $x \in [1.0, 1.25]$	71
Figure 3.6	Example 2: Solution (h in upper left, u in upper right, and B on bottom) computed with $N = 50$, $N = 100$, $N = 200$, $N = 400$ at $t = 1.05$	73
Figure 3.7	Example 3: Solution (B) computed with $N = 50$, $N = 100$, $N = 200$, $N = 400$, and approximate solution at $t = 238709$	74
Figure 3.8	Example 4: Solutions (B) computed at $t = 0$ with $N = 400$ and at $t = 238$ with $N = 100$, $N = 200$, and $N = 400$ using water wave speed for the sediment (left) and using the sediment wave speed for the sediment (right). . .	75
Figure 3.9	Example 5: Solution (B) computed with $N = 400$ at $t = 1904$	76
Figure 3.10	Example 6: Solution (B) computed with $N = 200$ at $t = 0$ and $t = 900000$. . .	77
Figure 4.1	Example 1: Approximate solution for the angle of spread.	88
Figure 4.2	Example 1: Solution (B) computed at $t = 0$ (left) and $t = 360000$ (right) with $\Delta x = 50$ and $\Delta y = 50$	89
Figure 4.3	Example 1: Solution (B) computed at $t = 0$ (left) and $t = 360000$ (right) with $\Delta x = 50$ and $\Delta y = 50$	89
Figure 4.4	Example 1: Evolution of Conical Dune (B) at $t = 0$, $t = 90000$, $t = 180000$, $t = 360000$ and approximate spread angle with $\Delta x = 50$ and $\Delta y = 50$	90

Chapter 1

INTRODUCTION

1.1 Motivation

In recent years the modeling of sediment transport has been of interest to those in the hydraulics community for its use in environmental and engineering problems. One example is that sediment transport can influence the construction of harbors since sediment entering the harbor can damage the layout of the harbor, and dredging the harbor can be expensive. In addition, sediment building up can cause reservoirs to lose a significant amount of their capacity. Looking at U.S. reservoirs in 1973, Cunge et al. [19] stated that, by 1973, 33% of the reservoirs built before 1935 had lost between 25% to 50% of their original capacity. The modeling of sediment transport can also be of use in the construction of underwater oil wells. Underwater oil wells, when built too low above the ocean floor, run the risk of sediment covering the wells. As a result, the wells are built taller than needed, a costly expenditure.

The modeling of sediment transport incorporates a balance between the modeling of flowing water and that of the sediment. The water flow is modeled using the Saint-Venant system of shallow water equations which was introduced over 140 years ago in [20] and is still used in modeling flow in rivers, lakes, and coastal areas. In this thesis, we use both the one-dimensional (1-D) and two-dimensional (2-D) Saint-Venant systems, with the 2-D system given as

$$\begin{pmatrix} h \\ hu \\ hv \end{pmatrix}_t + \begin{pmatrix} hu \\ hu^2 + \frac{g}{2}h^2 \\ huv \end{pmatrix}_x + \begin{pmatrix} hv \\ huv \\ hv^2 + \frac{g}{2}h^2 \end{pmatrix}_y = \begin{pmatrix} 0 \\ -ghB_x \\ -ghB_y \end{pmatrix}, \quad (1.1)$$

where x, y are spatial vectors, t is the time, $B(x, y)$ is the bottom topography elevation, $h(x, y, t)$ is the fluid depth above the bottom, $u(x, y, t)$ is the velocity in the x -direction, $v(x, y, t)$ is the

velocity in the y -direction and g is a constant for gravity.

Since the Saint-Venant system of shallow water equations (1.1) does not incorporate sediment and has a bottom $B(x, y)$ that is independent of time, we use an additional equation to govern the sediment transport. Sediment transport is mainly characterized into two main categories: bed load transport and suspended load transport, which refer to the sediment on the bottom topography and sediment moving within the water column, respectively. If a model incorporates both of these processes, it is said to cover the total transport. A third category which is less commonly accounted for is saltation, which is when single grains jump a short distance over the bed, settling back onto it. This is a mixture of the bed load and suspension transport. Due to the complexity and different natures of the processes for bed load and suspended load transport many models focus on only one of these processes. In this thesis, we will not consider suspension load transport, instead focusing on bed load transport. For the transport of the sediment layer we will be using a bed load updating equation called an Exner equation [23] in 1-D and 2-D, with the 2-D Exner equation given by

$$B_t + \xi \frac{\partial q_{b1}}{\partial x} + \xi \frac{\partial q_{b2}}{\partial y} = 0, \quad (1.2)$$

where the variable $\xi = \frac{1}{1 - \epsilon}$ is a constant with ϵ representing the porosity of the sediment layer. The closer ϵ is to zero the larger the particles that comprise the sediment. We also define $q_{b1}(h, u, v)$ to be the sediment transport discharge fluxes in the x -direction and $q_{b2}(h, u, v)$ to be the sediment transport discharge fluxes in the y -direction. These sediment fluxes depend on various water and sediment properties with a multitude of models used to represent them, a few of which are defined in Section 1.3.2.

1.2 Shallow Water Equations

In this section, we will briefly describe the derivation of the 2-D shallow water equations and their properties. For the shallow water equations, we will assume that fluid is in a channel of unit width, and the depth is much smaller than the width of the channel. In terms of velocity, we assume the vertical velocity of the fluid $\omega(x, y, t)$ is negligible, and that the velocities $u(x, y, t)$ and $v(x, y, t)$ are roughly constant throughout the cross section of the channel. We define the vector of velocities to be $\mathbf{u}(x, y, t) = (u(x, y, t), v(x, y, t), \omega(x, y, t))$. The general picture to have in mind is given in Figure 1.1.

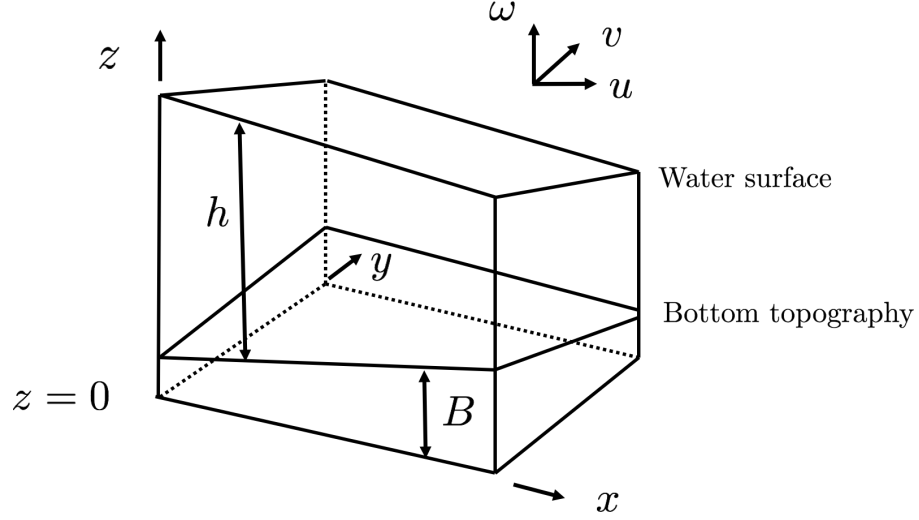


Figure 1.1: Shallow Water Domain.

1.2.1 Derivation of First Equation: Conservation of Mass

To balance the mass on a control volume Ω with boundary $\partial\Omega$, we let ρ be the fluid density, $\mathbf{u} \in \mathbb{R}^m$ be the fluid velocities, and \mathbf{n} be the outward normal vector on $\partial\Omega$. The balance of mass on a control volume Ω is given by

$$\underbrace{\frac{\partial}{\partial t} \int_{\Omega} \rho \, dV}_{\text{The rate of change of total mass in } \Omega} = - \underbrace{\int_{\partial\Omega} (\rho \mathbf{u}) \cdot \mathbf{n} \, dA}_{\text{The net mass flux across the boundary of } \Omega}. \quad (1.3)$$

We can now apply the Divergence Theorem to the right hand side of (1.3) to rewrite the outward flux through the surface as the divergence over the region,

$$\frac{\partial}{\partial t} \int_{\Omega} \rho \, dV = - \int_{\Omega} \nabla \cdot (\rho \mathbf{u}) \, dV. \quad (1.4)$$

Assuming that ρ is smooth, we can move the derivative to the inside of the integral and rewrite (1.4) as

$$\int_{\Omega} \left[\frac{\partial \rho}{\partial t} + \nabla \cdot (\rho \mathbf{u}) \right] dV = 0. \quad (1.5)$$

Since we chose our region Ω arbitrarily, we can rewrite (1.5) as

$$\frac{\partial \rho}{\partial t} + \nabla \cdot (\rho \mathbf{u}) = 0. \quad (1.6)$$

Equation (1.6) is a general formula for conservation of mass. In order to derive the conservation of mass equation for the 2-D shallow water equations we need to apply boundary conditions at the bottom $z = B(x, y)$ and the free surface $z = h(x, y, t) + B(x, y)$, recalling that in the shallow water equations the bottom B is fixed in time.

At the bottom $z = B(x, y)$, we have

$$\text{No normal flow: } u \frac{\partial B}{\partial x} + v \frac{\partial B}{\partial y} + \omega = 0. \quad (1.7)$$

At the surface the solution is slightly more complicated as the free surface may be moving. Therefore, at the free surface $z = h(x, y, t) + B(x, y)$, we have

$$\text{No relative normal flow: } \frac{\partial(h+B)}{\partial t} + u \frac{\partial(h+B)}{\partial x} + v \frac{\partial(h+B)}{\partial y} - \omega = 0. \quad (1.8)$$

We want depth averaged values for our equation, so we integrate (1.6) over the depth from $z = B(x, y)$ to $z = h(x, y, t) + B(x, y)$. Note for simplicity in our notation we will suppress the dependance on x, y , and t . Then,

$$\begin{aligned} \int_B^{h+B} \frac{\partial \rho}{\partial t} dz + \int_B^{h+B} \nabla \cdot (\rho \mathbf{u}) dz &= 0, \\ \int_B^{h+B} \frac{\partial \rho}{\partial t} dz + \int_B^{h+B} \left(\frac{\partial(\rho u)}{\partial x} + \frac{\partial(\rho v)}{\partial y} + \frac{\partial(\rho \omega)}{\partial z} \right) dz &= 0, \\ \int_B^{h+B} \frac{\partial \rho}{\partial t} dz + \int_B^{h+B} \left(\frac{\partial(\rho u)}{\partial x} + \frac{\partial(\rho v)}{\partial y} \right) dz + (\rho \omega)|_{z=h+B} - (\rho \omega)|_{z=B} &= 0. \end{aligned} \quad (1.9)$$

Since the functions that are being differentiated and the limits or integration are continuous and have continuous partial derivatives, we can apply the Leibniz integral rule to (1.9) to obtain

$$\begin{aligned} \frac{\partial}{\partial t} \int_B^{h+B} \rho dz &- \left(\rho|_{z=h+B} \frac{\partial(h+B)}{\partial t} - \rho|_{z=B} \frac{\partial B}{\partial t} \right) \\ &+ \frac{\partial}{\partial x} \int_B^{h+B} \rho u dz - \left(\rho u|_{z=h+B} \frac{\partial(h+B)}{\partial x} - \rho u|_{z=B} \frac{\partial B}{\partial x} \right) \\ &+ \frac{\partial}{\partial y} \int_B^{h+B} \rho v dz - \left(\rho v|_{z=h+B} \frac{\partial(h+B)}{\partial y} - \rho v|_{z=B} \frac{\partial B}{\partial y} \right) \\ &+ \rho \omega|_{z=h+B} - \rho \omega|_{z=B} = 0. \end{aligned} \quad (1.10)$$

Using our boundary conditions (1.7) and (1.8) and since the bottom B is fixed in time, the evaluations at the boundary for $\rho, \rho u, \rho v$, and $\rho \omega$ in (1.11) equal zero. Cancelling these terms

and evaluating the remaining integrals, we have

$$\begin{aligned} \frac{\partial}{\partial t} (\rho(h+B) - \rho B) + \frac{\partial}{\partial x} (\rho u(h+B) - \rho u B) + \frac{\partial}{\partial y} (\rho v(h+B) - \rho v B) &= 0, \\ \frac{\partial}{\partial t} (\rho h) + \frac{\partial}{\partial x} (\rho h u) + \frac{\partial}{\partial y} (\rho h v) &= 0. \end{aligned} \quad (1.11)$$

The density ρ depends on the pressure, temperature, and salinity of the fluid. We assume that the temperature and salinity are constant in our domain, and, since our fluid is water, it is incompressible. Therefore, ρ also does not depend on the pressure; thus, ρ can be taken as a constant. We factor ρ out of (1.11), and the first equation of the 2-D shallow water equation system is given by

$$\frac{\partial}{\partial t} (h) + \nabla \cdot (h \mathbf{u}) = 0. \quad (1.12)$$

1.2.2 Derivation of Second and Third Equation: Conservation of Momentum

To balance the momentum on a control volume Ω with boundary $\partial\Omega$, we again let ρ be the fluid density, $\mathbf{u} \in \mathbb{R}^m$ be the fluid velocities, and \mathbf{n} be the outward normal vector on $\partial\Omega$. The balance of momentum on a control volume Ω is given by

$$\underbrace{\frac{\partial}{\partial t} \int_{\Omega} \rho \mathbf{u} \, dV}_{\substack{\text{The rate of change} \\ \text{of total momentum in } \Omega}} = - \underbrace{\int_{\partial\Omega} (\rho \mathbf{u}) \mathbf{u} \cdot \mathbf{n} \, dA}_{\substack{\text{The net momentum flux across} \\ \text{the boundary of } \Omega}} + \underbrace{\int_{\partial\Omega} (pI - II) \cdot \mathbf{n} \, dA}_{\substack{\text{The surface forces} \\ \text{acting on } \partial\Omega}} + \underbrace{\int_{\Omega} \rho \mathbf{g} \, dV}_{\substack{\text{The volume forces} \\ \text{acting on } \Omega}}, \quad (1.13)$$

where \mathbf{g} is the body force, p is the pressure, I is the identity matrix, and II is the viscous stress tensor given by

$$II = \begin{bmatrix} \tau^{xx}, \tau^{xy}, \tau^{xz} \\ \tau^{yx}, \tau^{yy}, \tau^{yz} \\ \tau^{zx}, \tau^{zy}, \tau^{zz} \end{bmatrix}. \quad (1.14)$$

We can now combine the two surface integrals and apply the Divergence Theorem on them to get

$$\frac{\partial}{\partial t} \int_{\Omega} \rho \mathbf{u} \, dV = \int_{\Omega} \nabla \cdot [(\rho \mathbf{u}) \mathbf{u} + \rho(pI - II) + \rho \mathbf{g}] \, dV. \quad (1.15)$$

Assuming that ρ is smooth, we move the derivative to the inside of the integral, and rewrite (1.15) as

$$\int_{\Omega} \left[\frac{\partial(\rho \mathbf{u})}{\partial t} + \nabla \cdot [(\rho \mathbf{u}) \mathbf{u} + (pI - II) + \rho \mathbf{g}] \right] \, dV = 0. \quad (1.16)$$

Since we chose our region Ω arbitrarily, we can rewrite (1.16) as

$$\frac{\partial(\rho \mathbf{u})}{\partial t} + \nabla \cdot [(\rho \mathbf{u}) \mathbf{u} + (pI - II) + \rho \mathbf{g}] = 0. \quad (1.17)$$

Equation (1.17) is a general formula for conservation of momentum. In order to derive the equations specific to the 2-D shallow water equations we need to apply a few assumptions. The first is that the only body force acting on the system is the force of gravity. Thus $\mathbf{g} = (g_1, g_2, g_3) \equiv (0, 0, -g)$ where g is the acceleration due to gravity, a constant value. Secondly, from the assumption that the vertical velocity is small and can be neglected, we have $\frac{D}{Dt}\omega = \frac{\partial \omega}{\partial t} + \mathbf{u} \cdot \nabla \omega = 0$, where $\frac{D}{Dt}$ denotes the total derivative which computes the time rate of change of any quantity for a portion of material moving with a velocity \mathbf{u} . Lastly, we assume that the flow is inviscid, meaning that the viscous stress tensor II is zero.

The system in (1.17) can now be written as

$$\begin{bmatrix} \rho u \\ \rho v \\ \rho \omega \end{bmatrix}_t + \begin{bmatrix} \rho u u + p \\ \rho v u \\ \rho \omega u \end{bmatrix}_x + \begin{bmatrix} \rho u v \\ \rho v v + p \\ \rho \omega v \end{bmatrix}_y + \begin{bmatrix} \rho u \omega \\ \rho v \omega \\ \rho \omega \omega + p \end{bmatrix}_z = \begin{bmatrix} 0 \\ 0 \\ -\rho g \end{bmatrix}. \quad (1.18)$$

By expanding the derivatives in (1.18) and using the equation for conservation of mass (1.6), we rewrite (1.18) as

$$\rho u_t + \rho u u_x + \rho v u_y + \rho \omega u_z + p_x = 0, \quad (1.19)$$

$$\rho v_t + \rho u v_x + \rho v v_y + \rho \omega v_z + p_y = 0, \quad (1.20)$$

$$\rho \omega_t + \rho u \omega_x + \rho v \omega_y + \rho \omega \omega_z + p_z = -\rho g. \quad (1.21)$$

Since we assume that the vertical velocity ω is small and thus the vertical component of acceleration given by the material derivative $\frac{D}{Dt}\omega = 0$, we can rewrite (1.21) as

$$\begin{aligned} \rho \omega_t + \rho u \omega_x + \rho v \omega_y + \rho \omega \omega_z + p_z &= -\rho g, \\ \rho \frac{D\omega}{Dt} + p_z &= -\rho g, \\ p_z &= -\rho g. \end{aligned} \quad (1.22)$$

At the free surface $z = h + B$, the pressure is equal to the pressure from the atmosphere, $p = p_{atm}$. For convenience we will take p_{atm} to be zero. Now, integrating (1.22) and applying the pressure boundary condition at the free surface, we get $p(h + B) = 0$. Thus, we arrive at

the hydrostatic pressure relation

$$p = \rho g[(h + B) - z], \quad (1.23)$$

which represents the pressure exerted by a liquid. Note from (1.23) that the deeper you go under the surface, the greater the pressure will be. From the relation (1.23) we find a formula for the other pressure terms p_x and p_y in (1.19) and (1.20), respectively,

$$p_x = \rho g(h + B)_x, \quad (1.24)$$

$$p_y = \rho g(h + B)_y. \quad (1.25)$$

We further simplify (1.19) and (1.20), by noting that p_x and p_y are independent of z , and thus the left hand side must be as well. Therefore, the z velocity terms will vanish, and u and v are independent of z . We rewrite (1.19) and (1.20), plugging in (1.24) and (1.25), to obtain

$$\rho u_t + \rho u u_x + \rho v u_y = -\rho g(h + B)_x, \quad (1.26)$$

$$\rho v_t + \rho u v_x + \rho v v_y = -\rho g(h + B)_y. \quad (1.27)$$

To express (1.26) and (1.27) in a conservative form similar to (1.11) for the conservation for mass, we rewrite the system, starting with (1.26), by first multiplying it by the fluid height h and adding (1.11) multiplied by u , to obtain

$$h(\rho u_t + \rho u u_x + \rho v u_y) + u(\rho h)_t + u(\rho h u)_x + u(\rho h v)_y = h(-\rho g(h + B)_x), \quad (1.28)$$

$$(\rho h)u_t + u(\rho h)_t + (\rho h u)_x + u(\rho h u)_x + (\rho h v)_y + u(\rho h v)_y = -\rho g h(h + B)_x. \quad (1.29)$$

As was stated with the conservation of mass equation, ρ can be taken as a constant and factored out. Once factored out, we separate the right hand side into the h_x and B_x terms and rewrite the left hand side, recognizing a number of chain rules. Thus, we have

$$h u_t + u h_t + (h u)_x + u(h u)_x + (h v)_y + u(h v)_y = -g h h_x - g h B_x, \quad (1.30)$$

$$(h u)_t + (h u^2)_x + (h u v)_y = -\left(\frac{1}{2} g h^2\right)_x - g h B_x, \quad (1.31)$$

$$(h u)_t + (h u^2 + \frac{1}{2} g h^2)_x + (h u v)_y = -g h B_x. \quad (1.32)$$

Equation (1.32) represents the second of the 2-D shallow water equations: conservation of momentum in the x -direction.

In a similar way, we find the third equation by multiplying (1.27) by the fluid height h and

adding (1.11) multiplied by v to obtain

$$h(\rho v_t + \rho uv_x + \rho vv_y) + v(\rho h)_t + v(\rho hu)_x + v(\rho hv)_y = h(-\rho g(h + B)_y), \quad (1.33)$$

$$(\rho h)v_t + v(\rho h)_t + (\rho hv)_x + u(\rho hv)_x + (\rho hv)_y + v(\rho hv)_y = -\rho gh(h + B)_x. \quad (1.34)$$

Again, ρ can be taken as a constant and factored out. Once factored out, we separate the right hand side into the h_y and B_y terms and rewrite the left hand side, recognizing a number of chain rules. Thus, we have

$$hv_t + vh_t + (hv)u_x + u(hv)_x + (hv)v_y + v(hv)_y = -ghh_y - ghB_y, \quad (1.35)$$

$$(hv)_t + (huv)_x + (hv^2)_y = -\left(\frac{1}{2}gh^2\right)_y - ghB_y, \quad (1.36)$$

$$(hv)_t + (huv)_x + (hv^2 + \frac{1}{2}gh^2)_y = -ghB_y. \quad (1.37)$$

Equation (1.37) represents the third of the 2-D shallow water equations: conservation of momentum in the y -direction.

1.2.3 Hyperbolic System of Conservation and Balance Laws

In the previous subsections, we derived the individual equations for the 2-D system of shallow water equations given by (1.12), (1.32), and (1.37), resulting in the system given in (1.1). The system of shallow water equations, belongs to the category of hyperbolic systems of the form,

$$\frac{\partial}{\partial t} \mathbf{U}(x, y, t) + \frac{\partial}{\partial x} \mathbf{F}(\mathbf{U}(x, y, t)) + \frac{\partial}{\partial y} \mathbf{G}(\mathbf{U}(x, y, t)) = \mathbf{S}(x, y, t). \quad (1.38)$$

In the general case, $\mathbf{U} \in \mathbb{R}^m$ is an m -dimensional vector of conserved variables, that is variables whose quantities are neither created nor destroyed. $\mathbf{F}(\mathbf{U}) \in \mathbb{R}^m$ and $\mathbf{G}(\mathbf{U}) \in \mathbb{R}^m$ are referred to as flux functions with $\mathbf{S}(x, y, t)$ being the source term. If the bottom topography is flat, then $B_x = 0$ and $B_y = 0$ in (1.1). Thus, \mathbf{S} is zero, and a system written in the form of (1.38), is called a conservation law when $\mathbf{S}(x, y, t) = 0$. A conservation law in quasilinear form is given by

$$\mathbf{U}_t + \frac{\partial \mathbf{F}}{\partial \mathbf{U}} \mathbf{U}_x + \frac{\partial \mathbf{G}}{\partial \mathbf{U}} \mathbf{U}_y = 0, \quad (1.39)$$

where $\frac{\partial \mathbf{F}}{\partial \mathbf{U}}, \frac{\partial \mathbf{G}}{\partial \mathbf{U}}$ are Jacobian matrices of size $m \times m$ in the general case. We say the system of conservation laws (1.39) is hyperbolic if any real combination $\alpha \frac{\partial \mathbf{F}}{\partial \mathbf{U}} + \beta \frac{\partial \mathbf{G}}{\partial \mathbf{U}}$ has real eigenvalues and is diagonalizable.

The shallow water equations and conservation laws are important to many applications in science and engineering which deal with conserved quantities such as mass, momentum, and

energy, and thus can be modeled with PDEs of this form. Difficulties in solving these equations arise that are both inherent to the system and caused by solving the system numerically. The first difficulties may arise in solving (1.39) as the solutions to the system may have complicated structures such as shocks and rarefactions. Possible discontinuities in the solution may also develop in finite time, even if the initial conditions were smooth. Where the solution is discontinuous, the PDE is not satisfied in the classical sense, so we work with the integral form of the equations (1.5) and (1.16). A second difficulty, when dealing with the integral form of the system, is that we have weak solutions which are non-unique. Since the equations are only a model of reality, the challenge is to be able to choose a physically relevant solution.

When the source term in (1.38) is nonzero ($\mathbf{S} \neq 0$), the conservation laws are instead referred to as balance laws. Since most physical applications of the shallow water equations do not deal with a perfectly flat bottom where bottom derivatives are zero, they are usually represented as a balance law. This addition of a nonzero source term may make numerically solving the system a more complicated task. To help with numerically solving the balance laws a special set of solutions called steady-state solutions are used. These steady state solutions, which are solutions that do not change in time, i.e. their time derivatives are zero, are physically relevant and important for numerical methods. A good numerical method should be able to capture steady states and small perturbations of steady states. A numerical method which is able to capture a particular steady state is referred to as well balanced and will be further discussed section 1.4. In the following subsection, we will derive a formula for steady states of the shallow water equations.

1.2.4 Steady States of Shallow Water Equations

The 2-D system of shallow water equations (1.1) has both smooth and non-smooth steady state solutions. In this section, we derive some of these steady state solutions. At steady state all the time derivatives are zero, and therefore (1.1) reduces to

$$\begin{cases} (hu)_x + (hv)_y &= 0, \\ (hu^2 + \frac{1}{2}gh^2)_x + (huv)_y &= -ghB_x, \\ (huv)_x + (hv^2 + \frac{1}{2}gh^2)_y &= -ghB_y. \end{cases} \quad (1.40)$$

One solution to the first equation of (1.40) is $(hu)_x = 0$ and $(hv)_y = 0$. Since the spatial derivatives are both zero, this implies

$$hu = \text{constant} \quad \text{and} \quad hv = \text{constant}. \quad (1.41)$$

Looking at the second equation of (1.40) we can expand using the chain rule to obtain

$$u(hu)_x + (hu)u_x + gh h_x + u(hv)_y + (hv)u_y = -ghB_x. \quad (1.42)$$

From (1.41), we have that $(hu)_x = 0$ and $(hv)_y = 0$, and using this and rearranging (1.42) we have

$$\cancel{u(hu)_x}^0 + (hu)u_x + gh h_x + \cancel{u(hv)_y}^0 + (hv)u_y + ghB_x = 0, \quad (1.43)$$

$$h(uu_x + gh_x + gB_x + vu_y) = 0, \quad (1.44)$$

$$uu_x + gh_x + gB_x + vu_y = 0. \quad (1.45)$$

Since u is the velocity in the x -direction, $u_y = 0$. Therefore, (1.45) can be rewritten as

$$uu_x + gh_x + gB_x + \cancel{vu_y}^0 = 0, \quad (1.46)$$

$$\left(\frac{1}{2}u^2 + gh + gB\right)_x = 0, \quad (1.47)$$

$$\left(\frac{1}{2}u^2 + g(h + B)\right)_x = 0. \quad (1.48)$$

Therefore, this implies that

$$\frac{1}{2}u^2 + g(h + B) = \text{constant}. \quad (1.49)$$

We now consider the third equation of (1.40) which we expand using the chain rule to obtain

$$v(hu)_x + (hu)v_x + v(hv)_y + (hv)v_y + gh h_y = -ghB_y. \quad (1.50)$$

From (1.41) we have $(hu)_x = 0$ and $(hv)_y = 0$, and, using this and rearranging (1.50), we find that

$$\cancel{v(hu)_x}^0 + (hu)v_x + \cancel{v(hv)_y}^0 + (hv)v_y + gh h_y + ghB_y = 0, \quad (1.51)$$

$$h(uu_x + gh_x + gB_x + vu_y) = 0, \quad (1.52)$$

$$uv_x + vv_y + gh_y + gB_y = 0. \quad (1.53)$$

Since v is the velocity in the y -direction we have $v_x = 0$. Therefore, (1.53) can be rewritten as

$$uv_x + vv_y + gh_y + gB_y = 0, \quad (1.54)$$

$$\left(\frac{1}{2}v^2 + gh + gB\right)_y = 0, \quad (1.55)$$

$$\left(\frac{1}{2}v^2 + g(h + B)\right)_y = 0. \quad (1.56)$$

The third equation of (1.40) therefore implies that

$$\frac{1}{2}v^2 + g(h + B) = \text{constant}. \quad (1.57)$$

Putting together equations (1.41), (1.48), and (1.56), the 2-D shallow water system (1.1) admits steady state solutions satisfying

$$\begin{aligned} hu &= \text{constant}, \\ hv &= \text{constant}, \\ \frac{1}{2}u^2 + g(h + B) &= \text{constant}, \\ \frac{1}{2}v^2 + g(h + B) &= \text{constant}. \end{aligned} \quad (1.58)$$

One of the most important steady states satisfying (1.58) is the stationary steady state, which is also called the "lake-at-rest steady state". This steady state describes a motionless lake and is satisfied when

$$u = 0, \quad v = 0, \quad w := h + B = \text{constant}, \quad (1.59)$$

where w is defined to be the water surface.

1.3 Sediment Transport Equation

The 2-D shallow water equations (1.1) govern the flow of water, assuming that the bottom topography or sediment is fixed in time. In the physical world, we know that this is not always the case. Bedrock may appear fixed in the short term but may be moved over time, and a bottom made of sand can be in constant flux depending on how powerful the flow of water is. To incorporate the movement of the bottom, we need to add an additional equation to (1.1) which models the sediment transport. This equation (1.2), referred to as an Exner equation from Austrian meteorologist and sedimentologist Felix Maria Exner, will be used to model

the mass transport of the sediment and will resemble the mass transport equation for the water (1.12). One main difference between the mass transport equation for the water and the Exner equation is that in (1.12) the water flux is always represented by hu in the x -direction and hv in the y -direction, while in (1.2) the sediment fluxes (q_{b_1}, q_{b_2}) in the Exner equation can be represented by various formulations. These sediment flux formulations can depend on various physical parameters such as sediment grain size, and angle of elevation of the bottom topography. This will be discussed in Section 1.3.2 and examples can be found in [10, 30, 66, 67, 69, 75].

In sediment transport formulations, the mass of the sediment or total load for the sediment flux can be written in two parts that incorporate the bed load transport q_b and the suspended load transport q_s . The bed load transport incorporates the sediment being transported on the bed surface either by friction or gravity. The suspension transport incorporates the sediment that is picked up by the water and transported above the bed. The sediment moves within the water flow and may or may not be deposited back onto the bed. Thus we have that the total load for sediment flux is given by

$$q_{tot} = q_b + q_s. \quad (1.60)$$

While the total load sediment flux is made up of both the bed load and suspended sediment fluxes, one flux often dominates the other based on the environment. For slow moving water flows and beds with larger sediment, bed load transport will dominate as the water will not lift much sediment into the water flow. Suspended load transport will dominate in faster moving water flows and when the sediment is fine enough to be put into suspension. In a general, or typical, marine environment, bed load transport will dominate when sediment grains are coarser than approximately 0.2 mm, and suspended load transport will dominate for sediment grains finer than 0.2 mm [79].

In the following subsections, we derive the Exner equation for the sediment transport and discuss a number of empirically derived models for the sediment transport fluxes. These sediment transport flux formulations are obtained using bed load transport sediment fluxes q_b .

1.3.1 Derivation of Sediment Transport Equation

To balance the sediment mass on a control volume Ω with boundary $\partial\Omega$, we represent sediment density by ρ_s , sediment velocities by $\mathbf{u}_b \in \mathbb{R}^m$, and let \mathbf{n} be the outward normal vector on $\partial\Omega$.

The balance of sediment mass on a control volume Ω is then given by

$$\underbrace{\frac{\partial}{\partial t} \int_{\Omega} \rho_s(1 - \epsilon) dV}_{\text{The rate of change of total mass in } \Omega} = - \underbrace{\int_{\partial\Omega} [\rho_s(1 - \epsilon) \mathbf{u}_b] \cdot \mathbf{n} dA}_{\text{The net mass flux across the boundary of } \Omega}, \quad (1.61)$$

where $\rho_s(1 - \epsilon)$ is the packing density and ϵ is the porosity of the sediment [19]. We now apply the Divergence Theorem to the right hand side of (1.61), rewriting the outward flux through the surface to equal the divergence over the region,

$$\frac{\partial}{\partial t} \int_{\Omega} \rho_s(1 - \epsilon) dV = \int_{\Omega} \nabla \cdot [\rho_s(1 - \epsilon) \mathbf{u}_b] dV. \quad (1.62)$$

Assuming that $\rho_s(1 - \epsilon)$ is smooth, we can move the derivative to the inside and rewrite (1.62) as

$$\int_{\Omega} \left[\frac{\partial[\rho_s(1 - \epsilon)]}{\partial t} + \nabla \cdot [\rho_s(1 - \epsilon) \mathbf{u}_b] \right] dV = 0. \quad (1.63)$$

Since we chose our region Ω arbitrarily, we rewrite (1.63) as

$$\frac{\partial[\rho_s(1 - \epsilon)]}{\partial t} + \nabla \cdot [\rho_s(1 - \epsilon) \mathbf{u}_b] = 0. \quad (1.64)$$

Equation (1.64) is a general formula for conservation of sediment mass. In order to derive the 2-D Exner equation for sediment mass transport, we need to apply boundary conditions at the bed level, $z = B(x, y, t)$, where the sediment interacts with the water, and at the bottom topography reference level, $z = 0$, where the sediment is assumed to be fixed. In our boundary conditions, we assume the sediment is incompressible. Thus, p_s is constant and the sediment velocity is $\mathbf{u}_b = (u_b, v_b, \omega_b)$ where u_b, v_b , and ω_b are the sediment velocities in the x -direction, y -direction and z -direction, respectively.

At the reference level $z = 0$, let the sediment velocity $\mathbf{u}_b = (u_b, v_b, \omega_b)$. Then we have

$$u_b = v_b = \omega_b = 0. \quad (1.65)$$

At the bed level $z = B(x, y, t)$, we have no relative normal flow, so

$$\frac{\partial B}{\partial t} + u_b \frac{\partial B}{\partial x} + v_b \frac{\partial B}{\partial y} + \omega_b = 0. \quad (1.66)$$

To obtain depth averaged values for our equation, we integrate (1.64) over the depth of the sediment from $z = 0$ to $z = B(x, y, t)$. Note for simplicity in our notation we will suppress the

dependance on x , y , and t . Then,

$$\begin{aligned}
& \int_0^B \frac{\partial[\rho_s(1-\epsilon)]}{\partial t} dz + \int_0^B \nabla \cdot [\rho_s(1-\epsilon)\mathbf{u}_b] dz = 0, \\
& \int_0^B \frac{\partial[\rho_s(1-\epsilon)]}{\partial t} dz + \int_0^B \left(\frac{\partial[\rho_s(1-\epsilon)u_b]}{\partial x} + \frac{\partial[\rho_s(1-\epsilon)v_b]}{\partial y} + \frac{\partial[\rho_s(1-\epsilon)\omega_b]}{\partial z} \right) dz = 0, \\
& \int_0^B \frac{\partial[\rho_s(1-\epsilon)]}{\partial t} dz + \int_0^B \left(\frac{\partial[\rho_s(1-\epsilon)u_b]}{\partial x} + \frac{\partial[\rho_s(1-\epsilon)v_b]}{\partial y} \right) dz \\
& \quad + [\rho_s(1-\epsilon)\omega_b]|_{z=B} - [\rho_s(1-\epsilon)\omega_b]|_{z=0} = 0.
\end{aligned} \tag{1.67}$$

To simplify, we may factor out ρ_s , since it is a constant by assumption, and apply the Leibniz integral rule to (1.67) to obtain

$$\begin{aligned}
& \frac{\partial}{\partial t} \int_0^B (1-\epsilon) dz - (1-\epsilon)|_{z=B} \frac{\partial B}{\partial t} \\
& + \frac{\partial}{\partial x} \int_0^B (1-\epsilon)u_b dz - (1-\epsilon)u_b|_{z=B} \frac{\partial B}{\partial x} \\
& + \frac{\partial}{\partial y} \int_0^B (1-\epsilon)v_b dz - (1-\epsilon)v_b|_{z=B} \frac{\partial B}{\partial y} \\
& + \rho\omega|_{z=B} - \rho\omega|_{z=0} = 0.
\end{aligned} \tag{1.68}$$

Using the boundary conditions given in (1.65) and (1.66), the evaluations at the boundaries in (1.68) equal zero. Canceling these terms and evaluating the remaining integrals results in

$$\begin{aligned}
& \frac{\partial}{\partial t} [(1-\epsilon)B] + \frac{\partial}{\partial x} q_{b1} + \frac{\partial}{\partial y} q_{b2} = 0, \\
& \frac{\partial}{\partial t} B + \xi \frac{\partial}{\partial x} q_{b1} + \xi \frac{\partial}{\partial y} q_{b2} = 0.
\end{aligned} \tag{1.69}$$

We recall that $\xi = \frac{1}{1-\epsilon}$, and we let $q_{b1} = \int_0^B (1-\epsilon)u_b$ be the bed load sediment transport flux in the x -direction, and $q_{b2} = \int_0^B (1-\epsilon)v_b$ be the bed load sediment transport flux in the y -direction. The values for q_{b1} and q_{b2} are not always straight forward and can be calculated in a number of different ways. In the following sections, we will look at various ways of formulating the sediment transport flux.

1.3.2 Sediment Transport Formulations

This subsection discusses various formulations for the sediment transport fluxes $\mathbf{q}_b = (q_{b1}, q_{b2})$. First, we review the terms and physical meaning behind the variables used in the various

sediment transport fluxes. In general, hydrodynamic forcing agents, i.e the currents and waves, will affect the sediment movement primarily through the friction they exert on the sediment bed which is referred to as the bed shear stress τ_0 . Usually, τ_0 can be written in terms of the hydrodynamic unknowns as

$$\tau_0 = g\rho_w R_h |S_f|, \quad (1.70)$$

where $g\rho_w$ is the specific weight of the fluid, R_h is the hydraulic ratio which can be approximated by h , and S_f is the friction term for Manning's law given by

$$S_f = \frac{g\eta^2 |u| u}{R_h^{4/3}}, \quad (1.71)$$

with η representing Manning's coefficient. We then use τ_0 to define the Shields parameter θ (1936) which is a non-dimensional number used to calculate the initiation of sediment motion in a fluid. The Shields parameter is given by the following:

$$\theta = \frac{\tau_0}{g(\rho_s - \rho_w)d}, \quad (1.72)$$

where ρ_s is the density of the sediment, ρ_w is the density of the fluid (in our case, water), and d is the diameter of the sediment grains.

In addition, we make use of the threshold bed shear stress τ_{cr} and threshold Shields parameter θ_{cr} . The threshold or critical values are an indication of the amount of force required before a sediment grain starts moving. Like the normal Shields parameter, the threshold Shields parameter is the ratio of the force exerted by the bed shear stress acting to move a grain of sediment and the submerged weight of the grain counteracting it given by the following formula:

$$\theta_{cr} = \frac{\tau_{cr}}{g(\rho_s - \rho_w)d}. \quad (1.73)$$

Also note that we use the notation d_{50} to represent the size of a grain in the 50th percentile of all the grains that make up the sediment.

1.3.2.1 Du Boys (1879)

The first sediment transport formula was proposed by Du Boys in 1879. Du Boys divided the sediment into n layers with layer 1 being directly under the water, layer $(n - 1)$ directly above a fixed immobile bed, and layer n being the fixed bed. The thickness of the layers is assumed to be d_{50} with the velocity increasing linearly. If layer $(n - 1)$ starts moving with velocity Δu , then layer $(n - 2)$ will move with speed Δu in respect to the layer under it, for an absolute velocity of $2\Delta u$. Extending this up, layer one on the surface just below the water will move

with speed $(n - 1)\Delta u$. We then have the total discharge per unit width is given by

$$q_b = \frac{1}{2}(n - 1)\Delta u(nd_{50}). \quad (1.74)$$

We now have a formula for q_b , but the number of layers n is unknown, so we want to rewrite this in terms of known quantities. To accomplish this, Du Boys used a tractive force method which says that the tractive forces or shear forces, moving a particle on the channel bed will not exceed those resisting the particle motion, i.e. shear stress of the flow is equivalent to the friction at the bed ($\tau_0 = \tau_{cr}$). From the theory, we have

$$\tau_0 = \theta(\rho_s - \rho_w)gnd_{50}, \quad (1.75)$$

where the friction is proportional to the submerged weight of the overlying grains. From our assumption of a tractive force method, there is only one layer (the immobile bed layer), so $n = 1$ and $\tau_0 = \theta(\rho_s - \rho_w)gd_{50}$. Therefore, in general, when $(n - 1)$ layers are in motion $\tau_0 = n\tau_{cr}$, which implies $n = \frac{\tau_0}{\tau_{cr}}$. Plugging into (1.75), we obtain a formula for bed load sediment transport given by

$$q_b = \left(\frac{\Delta u d_{50}}{2\tau_{cr}^2} \right) \tau_0(\tau_0 - \tau_{cr}). \quad (1.76)$$

1.3.2.2 Meyer-Peter-Müller (MPM) (1948)

The MPM model is a well know empirical model proposed after a series of tests in Zurich in 1948 [67]. Meyer-Peter and Müller related bed load sediment flux and shear stress by the dimensionless formulation

$$q_b = 8\sqrt{\left(\frac{\rho_s}{\rho_w} - 1\right)}gd^3(\theta - \theta_{cr})^{3/2}. \quad (1.77)$$

The MPM model is typically used for the transport of sediment in rocky rivers rather than sandy areas and assumes a flat bed. It is important to this model that the shear stress τ and the shield parameter θ are defined well as the $(\theta - \theta_{cr})$ term will prevent motion while $\theta < \theta_{cr}$. In the MPM model, we have $\theta_{cr} = 0.047$ and $d_{50} = 0.4429$ mm. However both these numbers may change as the sediment properties change.

1.3.2.3 Fernandez Luque-VanBeek (FLV) (1976)

The FLV model proposed in 1976 [66] is an empirically derived model of a similar form to (1.77) given by

$$q_b = 5.7 \sqrt{\left(\frac{\rho_s}{\rho_w} - 1\right)} g d^3 (\theta - \theta_{cr})^{3/2}. \quad (1.78)$$

In their experiments, FLV used smaller sediment particles, and introduced a downward slope of up to 22° .

1.3.2.4 Grass (1981)

One of the simplest models derived for sediment flux was proposed by Grass in his book from 1981 [30]:

$$q_b = A_g \mathbf{u} \|\mathbf{u}\|_2^{m-1}, \quad 1 \leq m \leq 4, \quad (1.79)$$

where $m = 3$ is the usual value for the exponent. The value of $A \in [0, 1]$ is an experimentally determined constant that takes into account the sediment properties such as the size of the sediment and the viscosity of the fluid. If A is zero, there is no sediment transport, and the system (1.1)-(1.2) reduces down to just the shallow water equations. When A is small, there is a weak interaction between the sediment and the water, and when A is large (approaching 1), there is a strong interaction between the sediment and the water. One thing to note about this model is that there is no threshold necessary to initiate motion as there are in the other models in this section. This means that sediment bed load transport will begin with the fluid motion.

1.3.2.5 Nielsen (1992)

In 1992, Nielsen [69] proposed a model similar to that in (1.77) given by

$$q_b = 12 \sqrt{\left(\frac{\rho_s}{\rho_w} - 1\right)} g d^3 (\theta - \theta_{cr}) \sqrt{\theta}, \quad (1.80)$$

where $\theta_{cr} = 0.05$. This model is used for smaller grain sizes than the MPM model.

1.3.2.6 Modified Grass (2012)

In 2005, while investigating suspended load sediment transport, Pritchard and Hogg [75] noted that sediment flux should not depend solely on the water velocity \mathbf{u} . They implemented a flux for the suspension that depended on the water column h in addition to the water velocity u . In 2012, Briganti et al. [10] explored a linear relationship between the water column water height

and the water velocity \mathbf{u} with what we will refer to as a Modified Grass model given by

$$q_b = A_d h \mathbf{u} \|\mathbf{u}\|_2^3, \quad (1.81)$$

where $A_d \in [0, 1]$ is analogous to A in (1.79) and is an experimentally determined constant that takes into account the sediment properties such as the size of the sediment and the viscosity of the fluid. Adding the water column h to the flux helps fix a problem with Grass's model that the maximum velocity on the free surface is where $h = 0$. This is not physically correct, as, when there is no water, there is nothing to move the sediment. Adding h to the sediment flux helps to correct this non-physical result, while allowing the flux to remain large at the bottom as expected when the problem is fully flooded.

1.4 Finite Volume Methods

In this section, we discuss finite volume methods and their use in solving hyperbolic systems of conservation and balance laws such as (1.39). In particular, we will discuss Godunov-type finite-volume projection-evolution methods which were first derived in [28]. With these methods, at each time level, a solution is globally approximated by a piecewise polynomial function, which is then evolved to a new time using the integral form of the system of hyperbolic conservation laws, and projected back onto the original grid. Numerical difficulties that may arise when solving (1.39) with finite volume methods include the possibility of complicated structures in the solutions, such as shocks and rarefactions, and discontinuities in the solution that can develop in finite time, even if the initial conditions are smooth. For simplicity, we will discuss the 1-D system of conservation laws given by

$$\mathbf{U}_t + \mathbf{F}(\mathbf{U})_x = \mathbf{0}, \quad (1.82)$$

where $x \in \mathbb{R}^m$, $t \in \mathbb{R}^+$, $\mathbf{U}(x, t)$ is a vector of conserved quantities, and $\mathbf{F}(\mathbf{U})$ is a vector of flux terms. The first step of the method is to divide the computational domain into non-overlapping intervals. For simplicity, we will divide our domain into uniform intervals called cells, where we denote $C_j = (x_{j-\frac{1}{2}}, x_{j+\frac{1}{2}})$. Therefore, we have that $x_{j+\frac{1}{2}} - x_{j-\frac{1}{2}} = \Delta x$ for all j . Second, if an approximate solution is available at a time level t^n , then we define cell averages to be the average of the integral of a cell j . Thus,

$$\overline{\mathbf{U}}_j^n := \frac{1}{\Delta x} \int_{C_j} \mathbf{U}(x, t^n) dx. \quad (1.83)$$

Generally, the approximate solution at time t^n is reconstructed using a global piecewise polynomial. For example, the simplest reconstruction is the global piecewise constant approximation

of the solution given by

$$\tilde{\mathbf{U}}_j^n(x) := \sum_j \bar{\mathbf{U}}_j^n \chi_{C_j}, \quad (1.84)$$

where χ_{C_j} is the characteristic function of the interval C_j . This reconstruction is only first order accurate. In order to increase the accuracy, we would need to use a higher-order interpolant. A wide variety of reconstructions are available in literature, e.g. [1, 16, 27, 33, 34, 38, 42, 59]. We note that, in general, the solutions are discontinuous at the interfaces of the cells $x = x_{j \pm \frac{1}{2}}$. Using the reconstructed interpolant as the initial data at time $t = t^n$, we may now evolve to the next time level $t = t^{n+1}$ by integrating (1.82) over $C_j \times [t^n, t^{n+1}]$:

$$\begin{aligned} \mathbf{U}_t &= -\mathbf{F}(\mathbf{U})_x, \\ \frac{1}{\Delta x \Delta t} \int_{x_{j-\frac{1}{2}}}^{x_{j+\frac{1}{2}}} \int_{t^n}^{t^{n+1}} \mathbf{U}_t dx dt &= -\frac{1}{\Delta x \Delta t} \int_{x_{j-\frac{1}{2}}}^{x_{j+\frac{1}{2}}} \int_{t^n}^{t^{n+1}} \mathbf{F}(\mathbf{U})_x dx dt, \\ \bar{\mathbf{U}}_j^{n+1} &= \bar{\mathbf{U}}_j^n - \frac{1}{\Delta x} \int_{t^n}^{t^{n+1}} \left[\mathbf{F}(\mathbf{U}(x_{j+\frac{1}{2}}, t) - \mathbf{F}(\mathbf{U}(x_{j-\frac{1}{2}}, t)) \right] dt. \end{aligned} \quad (1.85)$$

The way that (1.85) is calculated will depend on the space-time control volumes that are selected, as seen in Figure 1.2. The first finite volume upwind scheme was proposed by Godunov

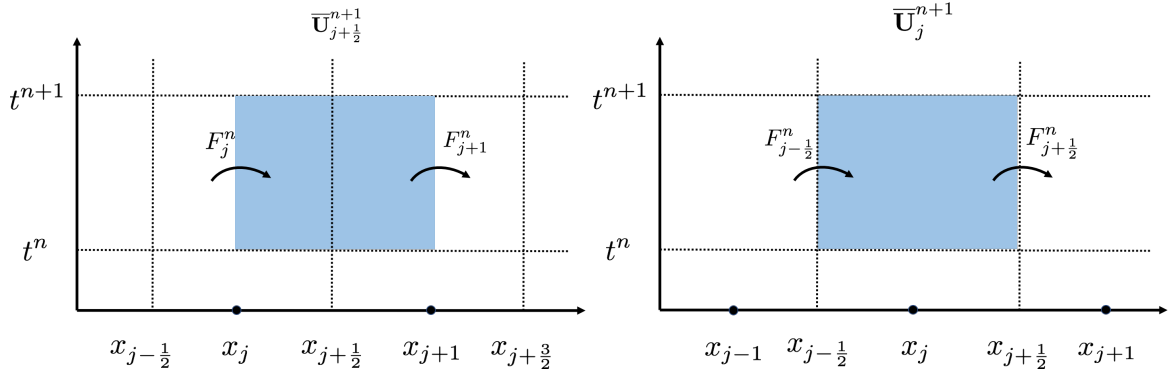


Figure 1.2: Left: Central (staggered) control volume. Right: Upwind control volume.

in [28] in 1959. For upwind schemes, the computation cell is chosen such that $C_j = (x_{j-\frac{1}{2}}, x_{j+\frac{1}{2}})$. Thus, the space-time control volume is given by $[x_{j-\frac{1}{2}}, x_{j+\frac{1}{2}}] \times [t^n, t^{n+1}]$. To solve the upwind scheme, we need to be able to solve or exactly approximately the integrals for the fluxes in (1.85), since the solution $\mathbf{U}(x, t^n)$ is discontinuous at the cell interfaces $x = x_{j \pm \frac{1}{2}}$ by the nature of the reconstruction (1.84). In order to compute the required values at the interfaces $\mathbf{U}(x \pm \frac{\Delta x}{2}, t^n)$, an approximate solution to the generalized Riemann problem is required, e.g.

[4, 9, 16, 27, 28, 42, 59, 84]. The drawback to such schemes is that they are restricted to systems in which Riemann solvers exist, which can be computationally expensive and very hard to obtain analytically. However, if the Riemann solver is available, upwind schemes are highly accurate and less dissipative and diffusive than central schemes, resulting in less smearing at the discontinuities.

First-order central schemes were introduced in 1954 by Lax and Friedrichs [25, 56]. Within the finite volume framework, we will be working with central schemes which are staggered, referred to as central (staggered) schemes, which allow one to evolve the solution without solving Riemann problems exactly or approximately. This works by computing the cell averages over a centered grid that is staggered, given by computational cell $C_{j+\frac{1}{2}} = (x_j, x_{j+1})$, rather than the original computed grid centered at j . The central (staggered) schemes framework of being Riemann-problem-solver-free is of particular importance to solving multi-dimensional problems as Riemann problem solvers do not exist. Central schemes have been developed further in literature including staggered and non-staggered variants, multidimensional generalizations, and higher order methods, as seen in , e.g. [2, 6, 15, 39, 43, 50, 54, 60–62, 64, 65, 68, 71, 72].

Through the use of a higher-order reconstruction instead of the first order reconstruction in (1.84), we can significantly improve the resolution of both upwind and central (staggered) schemes. While the results improve, the cost and difficulty of solving the Riemann problem still remains in upwind schemes, and central schemes may suffer from increased numerical viscosity. In addition to central and upwind schemes, a new class of Godunov-type finite volume methods that combines central and upwind schemes was introduced in [44, 45, 53] and are referred to as central-upwind schemes. These central-upwind schemes are able to combine the Riemann solver free aspect of the central scheme with the high accuracy and low dissipation of an upwind scheme, making them efficient, highly accurate, and applicable to a wide variety of multidimensional hyperbolic systems of conservation and balance laws. The idea behind central-upwind schemes is to use upwinding information at the interfaces, which are the one sided speeds of propagation of waves stemming from the discontinuities at these interfaces. The use of left-sided and right-sided speeds of propagation allow one to design an overall control volume made up of two smaller control volumes as seen in Figure 1.3. The first smaller control volume on the outside edges of Figure 1.3 (colored in blue) will contain the non-smooth nonlinear waves that are generated at the interface. The second smaller control volume located at the center of Figure 1.3 (colored in green) will contain all the smooth parts from the reconstruction. If the stability condition for the problem is chosen in a strong enough manner, we can then guarantee that no waves reach the boundaries of their smaller control volume, and the evolution remains central. Therefore, no Riemann problem solver is required. Central-upwind schemes have become more robust in recent years, being further developed in the literature by [5, 12, 13, 17, 44–49, 51, 52, 55]. In this thesis, we use a second order semi-discrete scheme outlined in section 1.5.

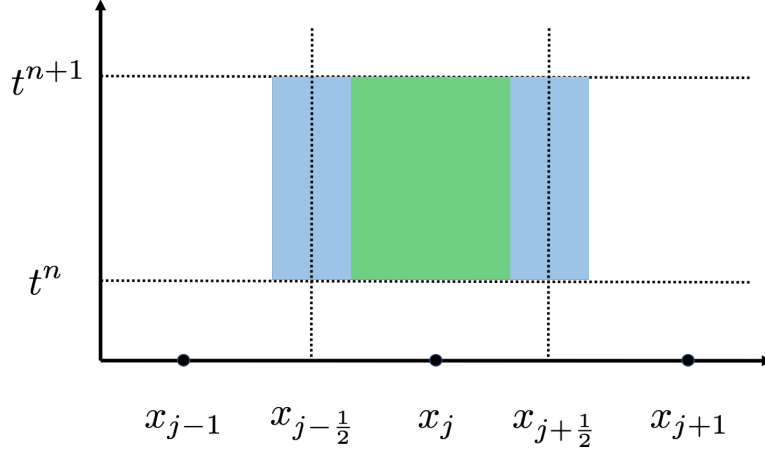


Figure 1.3: Central-Upwind Control Volume.

If the system from (1.82) does not have a zero right hand side, but instead is a balance law with a source term $\mathbf{S}(\mathbf{U})$ in 1-D given by

$$\mathbf{U}_t + \mathbf{F}(\mathbf{U})_x = \mathbf{S}(\mathbf{U}), \quad (1.86)$$

finding a solution is much more complicated. As discussed in section 1.2.3, one special class of solutions of particular importance to balance laws is that of steady states, or solutions that remain constant in time, since many additional solutions are small perturbations of steady states. Capturing these perturbations of steady state solutions can be numerically difficult, as the size of the perturbation may be smaller than the numerical error from the computation, particularly on a coarse grid. One way to overcome this challenge is to refine the grid, but this can be computationally expensive or unfeasible. Another difficulty that may arise is preserving the positivity of the computed solution so that it remains physically relevant as numerical oscillations may cause negative values for non-negative quantities. An example of this would be ensuring that the height of a water column is never negative, as the lowest it could be physically is zero which corresponds to the dry case.

To overcome these difficulties, it is important to design a scheme which is capable of exactly preserving a chosen steady state, referred to as being well-balanced (see eg. [3, 7, 8, 11, 26, 31, 40, 41, 50, 58, 70, 74, 76, 77, 87]), and is able to maintain the positivity of the numerical solution when physically relevant, referred to as positivity preserving (see eg. [3, 7, 8, 11, 26, 50]). If a scheme is well-balanced and positivity preserving, then perturbations of the numerical solution, both small and large, will be resolved in a non-oscillatory manner on a coarse grid.

1.4.1 Alternatives to the Central-Upwind Scheme

This thesis focuses on the development of second order semi-discrete central-upwind schemes in one and two dimensions which will be described fully in the following sections. However, we also wish to briefly discuss other schemes in literature used to solve the shallow water equations with Exner equation to govern sediment transport.

High resolution finite volume methods are used when high accuracy is needed such as when discontinuities and shocks are present. The computed solutions of these methods are second order or higher in accuracy at the smooth parts of the solution, are free of spurious oscillations, obtain high accuracy around discontinuities and shocks, and are computationally efficient. Two particular high resolution finite volume numerical schemes are Monotone Upstream-Centered Schemes for Conservation Laws (MUSCL), see Van Leer [85], and Weighted Essentially Non-Oscillatory (WENO), see Shu [78]. MUSCL schemes are a flux/slope limiter method which limit the solution gradient near shocks and discontinuities. When problems contain shocks and complex smooth solution structures, WENO schemes can provide good solution resolution around discontinuities and provide higher accuracy than second-order schemes. An implementation of a MUSCL method to the shallow water equations with Exner equation can be seen in [22] and an implementation of a WENO method to the shallow water equations with Exner equation can be seen in [35].

In addition to finite volume methods, finite element methods can be used in solving the shallow water equations with Exner equation. Finite element methods have the benefit that they can accommodate general cell shapes and thus can be well-suited for complex domains or topographical features [32]. One particular finite element method used is the Discontinuous Galerkin Method which combines the high-order accuracy and flexibility of elements of finite element methods with the local nature of finite volume methods. An implementation of a Discontinuous Galerkin Method to the shallow water equations with Exner equation can be seen in [83].

1.5 1-D Second Order Semi-Discrete Central-Upwind Scheme

In this section, we describe a 1-D second order semi-discrete central-upwind scheme for the hyperbolic balance law given by

$$\mathbf{U}_t + \mathbf{F}(\mathbf{U})_x = \mathbf{S}(\mathbf{U}). \quad (1.87)$$

First, the computational domain is broken into a uniform grid, for simplicity, with computational cells $C_j := [x_{j-\frac{1}{2}}, x_{j+\frac{1}{2}}]$ of size $|C_j| = \Delta x$, centered at $x = x_j$ for $j = 1, \dots, N$, with N being the number of computational cells. The cell averages are assumed to be known at a given time t and are computed as in (1.83). Applying a second order semi-discrete formulation of the

central upwind scheme to (1.87) results in the following system of ordinary differential equations (ODEs):

$$\frac{d}{dt} \bar{\mathbf{U}}_j(t) = -\frac{\mathbf{H}_{j+\frac{1}{2}}(t) - \mathbf{H}_{j-\frac{1}{2}}(t)}{\Delta x} + \bar{\mathbf{S}}_j(t), \quad (1.88)$$

where $\mathbf{H}_{j\pm\frac{1}{2}}$ are the central-upwind numerical fluxes given by

$$\mathbf{H}_{j+\frac{1}{2}}(t) = \frac{a_{j+\frac{1}{2}}^+ \mathbf{F}(\mathbf{U}_{j+\frac{1}{2}}^-) - a_{j+\frac{1}{2}}^- \mathbf{F}(\mathbf{U}_{j+\frac{1}{2}}^+)}{a_{j+\frac{1}{2}}^+ - a_{j+\frac{1}{2}}^-} + \frac{a_{j+\frac{1}{2}}^+ a_{j+\frac{1}{2}}^-}{a_{j+\frac{1}{2}}^+ - a_{j+\frac{1}{2}}^-} \left[\mathbf{U}_{j+\frac{1}{2}}^+ - \mathbf{U}_{j+\frac{1}{2}}^- \right], \quad (1.89)$$

and the cell averages of the source term are given by

$$\bar{\mathbf{S}}_j(t) \approx \frac{1}{\Delta x} \int_{C_j} \mathbf{S}(\mathbf{U}) dx. \quad (1.90)$$

In (1.89), $\mathbf{U}_{j+\frac{1}{2}}^\pm$ are the left and right point values of the computed solution at the cell interface $x = x_{j+\frac{1}{2}}$. For our scheme to be second-order, the point values should be calculated using piecewise linear reconstructions given by

$$\tilde{\mathbf{U}}(x) = \sum_j [\bar{\mathbf{U}}_j + (\mathbf{U}_x)_j(x - x_j)] \cdot \chi_{C_j}(x), \quad (1.91)$$

obtained at cell interfaces $x = x_{j+\frac{1}{2}}$ by

$$\mathbf{U}_{j+\frac{1}{2}}^+ = \bar{\mathbf{U}}_{j+1} - \frac{\Delta x}{2} (\mathbf{U}_x)_{j+1}, \quad \mathbf{U}_{j+\frac{1}{2}}^- = \bar{\mathbf{U}}_j + \frac{\Delta x}{2} (\mathbf{U}_x)_j. \quad (1.92)$$

In (1.91) and (1.92), $\chi_{C_j}(x)$ is the characteristic function of the interval C_j and $(\mathbf{U}_x)_j$ are the numerical derivatives, which should be computed using a nonlinear limiter in order to minimize oscillations. In our numerical experiments shown in Chapter 2, 3, and 4, we use the generalized minmod limiter (see, e.g., [63, 68, 82, 85]):

$$(\mathbf{U}_x)_j = \text{minmod} \left(\theta \frac{\bar{\mathbf{U}}_j - \bar{\mathbf{U}}_{j-1}}{\Delta x}, \frac{\bar{\mathbf{U}}_{j+1} - \bar{\mathbf{U}}_{j-1}}{2\Delta x}, \theta \frac{\bar{\mathbf{U}}_{j+1} - \bar{\mathbf{U}}_j}{\Delta x} \right), \quad \theta \in [1, 2], \quad (1.93)$$

where the minmod function is defined by

$$\text{minmod}(z_1, z_2, \dots) := \begin{cases} \min_j \{z_j\}, & \text{if } z_j > 0 \quad \forall j, \\ \max_j \{z_j\}, & \text{if } z_j < 0 \quad \forall j, \\ 0, & \text{otherwise.} \end{cases} \quad (1.94)$$

The parameter θ in (1.93) is used to control the amount of numerical viscosity with large θ values resulting in less dissipative results.

The one-sided local speeds of propagation $a_{j+\frac{1}{2}}^\pm$ used in the central-upwind numerical flux from (1.89) are obtained using the largest and smallest eigenvalues of the Jacobian matrix $\frac{\partial \mathbf{F}}{\partial \mathbf{U}}$ where $\lambda_1 < \dots < \lambda_N$ are the eigenvalues. Thus, we have

$$\begin{aligned} a_{j+\frac{1}{2}}^+ &= \max \left\{ \lambda_N \left(\frac{\partial \mathbf{F}}{\partial \mathbf{U}}(\mathbf{U}_{j+\frac{1}{2}}^-) \right), \lambda_N \left(\frac{\partial \mathbf{F}}{\partial \mathbf{U}}(\mathbf{U}_{j+\frac{1}{2}}^+) \right), 0 \right\}, \\ a_{j+\frac{1}{2}}^- &= \min \left\{ \lambda_1 \left(\frac{\partial \mathbf{F}}{\partial \mathbf{U}}(\mathbf{U}_{j+\frac{1}{2}}^-) \right), \lambda_N \left(\frac{\partial \mathbf{F}}{\partial \mathbf{U}}(\mathbf{U}_{j+\frac{1}{2}}^+) \right), 0 \right\}. \end{aligned} \quad (1.95)$$

Lastly, the evolution of the system of ODEs for the central-upwind semi-discretization system (1.88), should be integrated by a sufficiently accurate and stable ODE solver. We use a third order Strong Stability Preserving Runge Kutta (SSP-RK3) method from [29], which is outlined in Appendix A. In order for the computations to be stable, the time step should be chosen with the following CFL condition,

$$\Delta t \leq \delta \frac{\Delta x}{\max_j |a_{j+\frac{1}{2}}^\pm|}, \quad \delta \leq \frac{1}{2}. \quad (1.96)$$

1.6 2-D Second Order Semi-Discrete Central-Upwind Scheme

In this section, we describe a 2-D second order semi-discrete central-upwind scheme for the hyperbolic balance law given by

$$\mathbf{U}_t + \mathbf{F}(\mathbf{U})_x + \mathbf{G}(\mathbf{U})_y = \mathbf{S}(\mathbf{U}). \quad (1.97)$$

First, the computational domain is broken into a uniform grid in the x -direction and y -direction, for simplicity, with computational cells $C_{j,k} := [x_{j-\frac{1}{2}}, x_{j+\frac{1}{2}}] \times [y_{k-\frac{1}{2}}, y_{k+\frac{1}{2}}]$ of size $|C_{j,k}| = \Delta x \Delta y$, centered at (x_j, y_k) for $j = 1, \dots, N$, $k = 1, \dots, M$ with N and M being the number of computational cells in the x -direction and y -direction, respectively. The cell averages are assumed to be known at a given time t and are computed by

$$\bar{\mathbf{U}}_{j,k}(t) \approx \frac{1}{\Delta x \Delta y} \iint_{C_{j,k}} \mathbf{U}(x, y, t) dx dy. \quad (1.98)$$

Applying a second order semi-discrete formulation of the central upwind scheme to (1.98) results in the following system of ordinary differential equations (ODEs):

$$\frac{d}{dt} \bar{\mathbf{U}}_{j,k}(t) = - \frac{\mathbf{H}^x_{j+\frac{1}{2},k}(t) - \mathbf{H}^x_{j-\frac{1}{2},k}(t)}{\Delta x} - \frac{\mathbf{H}^y_{j,k+\frac{1}{2}}(t) - \mathbf{H}^y_{j,k-\frac{1}{2}}(t)}{\Delta y} + \bar{\mathbf{S}}_{j,k}(t), \quad (1.99)$$

where $\mathbf{H}^x_{j\pm\frac{1}{2},k}$ and $\mathbf{H}^y_{j,k\pm\frac{1}{2}}$ are the central-upwind numerical fluxes given by

$$\begin{aligned} \mathbf{H}^x_{j+\frac{1}{2},k}(t) &= \frac{a_{j+\frac{1}{2},k}^+ \mathbf{F}(\mathbf{U}_{j+\frac{1}{2},k}^-) - a_{j+\frac{1}{2},k}^- \mathbf{F}(\mathbf{U}_{j+\frac{1}{2},k}^+)}{a_{j+\frac{1}{2},k}^+ - a_{j+\frac{1}{2},k}^-} + \frac{a_{j+\frac{1}{2},k}^+ a_{j+\frac{1}{2},k}^-}{a_{j+\frac{1}{2},k}^+ - a_{j+\frac{1}{2},k}^-} \left[\mathbf{U}_{j+\frac{1}{2},k}^+ - \mathbf{U}_{j+\frac{1}{2},k}^- \right], \\ \mathbf{H}^y_{j,k+\frac{1}{2}}(t) &= \frac{b_{j,k+\frac{1}{2}}^+ \mathbf{G}(\mathbf{U}_{j,k+\frac{1}{2}}^-) - b_{j,k+\frac{1}{2}}^- \mathbf{G}(\mathbf{U}_{j,k+\frac{1}{2}}^+)}{b_{j,k+\frac{1}{2}}^+ - b_{j,k+\frac{1}{2}}^-} + \frac{b_{j,k+\frac{1}{2}}^+ b_{j,k+\frac{1}{2}}^-}{b_{j,k+\frac{1}{2}}^+ - b_{j,k+\frac{1}{2}}^-} \left[\mathbf{U}_{j,k+\frac{1}{2}}^+ - \mathbf{U}_{j,k+\frac{1}{2}}^- \right], \end{aligned} \quad (1.100)$$

and the cell averages of the source term are given by

$$\bar{\mathbf{S}}_{j,k}(t) \approx \frac{1}{\Delta x \Delta y} \iint_{C_{j,k}} \mathbf{S}(\mathbf{U}) dx dy. \quad (1.101)$$

In (1.100), $\mathbf{U}_{j+\frac{1}{2},k}^\pm$ and $\mathbf{U}_{j,k+\frac{1}{2}}^\pm$ are the left and right point values and bottom and top point values, respectively, of the computed solution at the cell interface $x = x_{j+\frac{1}{2}}, y = y_k$ and $x = x_j, y = y_{k+\frac{1}{2}}$. For our scheme to be second-order the point values should be calculated using piecewise linear reconstructions given by

$$\tilde{\mathbf{U}}(x, y) = \sum_{j,k} [\bar{\mathbf{U}}_{j,k} + (\mathbf{U}_x)_{j,k}(x - x_j) + (\mathbf{U}_y)_{j,k}(y - y_k)] \cdot \chi_{C_{j,k}}(x, y), \quad (1.102)$$

obtained at the midpoint cell interfaces $(x_{j\pm\frac{1}{2}}, y_k)$, and $(x_j, y_{k\pm\frac{1}{2}})$ by

$$\begin{aligned} \mathbf{U}_{j+\frac{1}{2},k}^+ &= \bar{\mathbf{U}}_{j+1,k} - \frac{\Delta x}{2} (\mathbf{U}_x)_{j+1,k}, & \mathbf{U}_{j+\frac{1}{2},k}^- &= \bar{\mathbf{U}}_{j,k} + \frac{\Delta x}{2} (\mathbf{U}_x)_{j,k}, \\ \mathbf{U}_{j,k+\frac{1}{2}}^+ &= \bar{\mathbf{U}}_{j,k+1} - \frac{\Delta y}{2} (\mathbf{U}_y)_{j,k+1}, & \mathbf{U}_{j,k+\frac{1}{2}}^- &= \bar{\mathbf{U}}_{j,k} + \frac{\Delta y}{2} (\mathbf{U}_y)_{j,k}. \end{aligned} \quad (1.103)$$

In (1.102) and (1.103), $\chi_{C_{j,k}}(x, y)$ is the characteristic function of the interval $C_{j,k}$ and $(\mathbf{U}_x)_{j,k}$ and $(\mathbf{U}_y)_{j,k}$ are the numerical derivatives in the x -direction and y -direction, respectively, which should be computed using a nonlinear limiter in order to minimize oscillations. Similar to the

1-D case in Section 1.5, we use the generalized minmod limiter:

$$(\mathbf{U}_x)_{j,k} = \text{minmod} \left(\theta \frac{\bar{\mathbf{U}}_{j,k} - \bar{\mathbf{U}}_{j-1,k}}{\Delta x}, \frac{\bar{\mathbf{U}}_{j+1,k} - \bar{\mathbf{U}}_{j-1,k}}{2\Delta x}, \theta \frac{\bar{\mathbf{U}}_{j+1,k} - \bar{\mathbf{U}}_{j,k}}{\Delta x} \right), \quad \theta \in [1, 2], \quad (1.104)$$

$$(\mathbf{U}_y)_{j,k} = \text{minmod} \left(\theta \frac{\bar{\mathbf{U}}_{j,k} - \bar{\mathbf{U}}_{j,k-1}}{\Delta y}, \frac{\bar{\mathbf{U}}_{j,k+1} - \bar{\mathbf{U}}_{j,k-1}}{2\Delta y}, \theta \frac{\bar{\mathbf{U}}_{j,k+1} - \bar{\mathbf{U}}_{j,k}}{\Delta y} \right), \quad \theta \in [1, 2], \quad (1.105)$$

where the minmod function is defined by

$$\text{minmod}(z_{1,1}, \dots, z_{j,k}) := \begin{cases} \min_{j,k} \{z_{j,k}\}, & \text{if } z_{j,k} > 0 \quad \forall j, k, \\ \max_{j,k} \{z_{j,k}\}, & \text{if } z_{j,k} < 0 \quad \forall j, k, \\ 0, & \text{otherwise.} \end{cases} \quad (1.106)$$

The parameter θ in (1.104) and (1.105) is used to control the amount of numerical viscosity with large θ values resulting in less dissipative results.

The one-sided local speeds of propagation in the x -direction and y -direction, $a_{j+\frac{1}{2},k}^\pm$ and $b_{j,k+\frac{1}{2}}^\pm$, used in the central-upwind numerical flux from (1.100) are obtained using the largest and smallest eigenvalues of the Jacobian matrices $\frac{\partial \mathbf{F}}{\partial \mathbf{U}}$ and $\frac{\partial \mathbf{G}}{\partial \mathbf{U}}$, respectively, where $\lambda_1 < \dots < \lambda_N$ are the eigenvalues. Thus, we have

$$\begin{aligned} a_{j+\frac{1}{2},k}^+ &= \max \left\{ \lambda_N \left(\frac{\partial \mathbf{F}}{\partial \mathbf{U}}(\mathbf{U}_{j+\frac{1}{2},k}^-) \right), \lambda_N \left(\frac{\partial \mathbf{F}}{\partial \mathbf{U}}(\mathbf{U}_{j+\frac{1}{2},k}^+) \right), 0 \right\}, \\ a_{j+\frac{1}{2},k}^- &= \min \left\{ \lambda_1 \left(\frac{\partial \mathbf{F}}{\partial \mathbf{U}}(\mathbf{U}_{j+\frac{1}{2},k}^-) \right), \lambda_1 \left(\frac{\partial \mathbf{F}}{\partial \mathbf{U}}(\mathbf{U}_{j+\frac{1}{2},k}^+) \right), 0 \right\}, \\ b_{j,k+\frac{1}{2}}^+ &= \max \left\{ \lambda_M \left(\frac{\partial \mathbf{G}}{\partial \mathbf{U}}(\mathbf{U}_{j,k+\frac{1}{2}}^-) \right), \lambda_M \left(\frac{\partial \mathbf{F}}{\partial \mathbf{U}}(\mathbf{U}_{j+\frac{1}{2}}^+) \right), 0 \right\}, \\ b_{j,k+\frac{1}{2}}^- &= \min \left\{ \lambda_1 \left(\frac{\partial \mathbf{G}}{\partial \mathbf{U}}(\mathbf{U}_{j,k+\frac{1}{2}}^-) \right), \lambda_1 \left(\frac{\partial \mathbf{F}}{\partial \mathbf{U}}(\mathbf{U}_{j,k+\frac{1}{2}}^+) \right), 0 \right\}. \end{aligned} \quad (1.107)$$

Lastly, the evolution of the system of ODEs for the central-upwind semi-discretization system (1.99), should be integrated by a sufficiently accurate and stable ODE Solver. We use a third order Strong Stability Preserving Runge Kutta (SSP-RK3) method from [29], which is outlined in Appendix A. In order for the computations to be stable, the time step should be chosen with the following CFL condition:

$$\Delta t \leq \delta \min \left\{ \frac{\Delta x}{\max_j |a_{j+\frac{1}{2},k}^\pm|}, \frac{\Delta x}{\max_j |b_{j,k+\frac{1}{2}}^\pm|} \right\}, \quad \delta \leq \frac{1}{4}. \quad (1.108)$$

1.7 Outline of the Dissertation

The remainder of this thesis is as follows. In Chapter 2, we implement a well-balanced, positivity preserving second order semi-discrete central-upwind scheme for the system of 1-D shallow water equations with a discontinuous bottom topography. We then demonstrate the computed results of this scheme, showing that the incorporation of a generally discontinuous reconstruction for the bottom produces robust, accurate, non-oscillatory results. In Chapter 3, we numerically solve the system of 1-D shallow water equations with 1-D Exner equation to govern sediment transport. Due to the nature of the interaction between the water and the sediment, we perform four implementations of a well-balanced second order semi-discrete central-upwind scheme to more accurately solve the system. In Chapter 4, we extend one of the one-dimensional schemes from Chapter 3 to two-dimensions, solving the 2-D shallow water equations with 2-D Exner equation. We then demonstrate the results on a numerical example. In Chapter 5, our conclusions are summarized, and we provide thoughts on future paths for this research.

Part I

Hydrodynamic: Shallow Water Equations with Discontinuous Bottom Topography

Chapter 2

A Well-Balanced, Positivity Preserving Central-Upwind Scheme for the 1-D Shallow Water System of Equations

The contents of this chapter have been submitted to the Bulletin of the Brazilian Mathematical Society [5].

In this chapter, we discuss a second-order central-upwind scheme from Bernstein et al. [5], which is a modification of the central-upwind scheme in [50]. The central-upwind scheme in [50] uses a continuous piecewise linear approximation of the bottom topography function B and is quite robust, although its accuracy may deteriorate when B is not smooth. In that case, the continuous interpolation of B may prevent the scheme from achieving high resolution. The new scheme relies on a *discontinuous* piecewise linear reconstruction of the bottom topography function B , and thus it is suitable for when B contains large jumps and can be extended to models with moving, time-dependent bottom topography functions for B , (which will be studied in Part II). In Section 2.2, we describe how the central-upwind scheme can be modified to be well-balanced, exactly preserving the lake-at-rest steady state, by a special numerical quadrature used for approximating the geometrical source term in the right-hand side (RHS) of the system (2.3). In Section 2.3, we show how the positivity of the computed water depth is achieved by applying a draining time step technique from [8] and a correction from [50]. Finally, in section 2.4, we illustrate the performance of the introduced central-upwind scheme on a number of numerical examples.

2.1 A Modified Second-Order Semi-Discrete Central-Upwind Scheme

To start, the 1-D system of shallow water equations can be written from (1.12) and (1.32) by letting $\mathbf{u} = (u, 0, 0)^\top$, resulting in

$$\begin{pmatrix} h \\ hu \end{pmatrix}_t + \begin{pmatrix} hu \\ hu^2 + \frac{1}{2}gh^2 \end{pmatrix}_x = \begin{pmatrix} 0 \\ -ghB_x \end{pmatrix}. \quad (2.1)$$

In Section 2.2, we discuss how to build the numerical scheme to be well balanced, by exactly preserving the lake-at-rest steady state (1.59). To this end, we choose to work with equilibrium variables, which remain fixed at our chosen steady state. From (1.59) and the first equation of (1.58), two such variables are the water surface $w = h + B$ and the discharge $q = hu$. Following [50], we start by rewriting the system (2.1) in terms of the equilibrium variables $\mathbf{U} = (w, q)^\top$:

$$\begin{pmatrix} w \\ q \end{pmatrix}_t + \begin{pmatrix} q \\ \frac{q^2}{w-B} + \frac{g}{2}(w-B)^2 \end{pmatrix}_x = \begin{pmatrix} 0 \\ -g(w-B)B_x \end{pmatrix}. \quad (2.2)$$

Furthermore, we expand and rewrite the second equation in (2.2) to make it easier to work with in Section 2.2. System (2.2) then becomes,

$$\begin{pmatrix} w \\ q \end{pmatrix}_t + \begin{pmatrix} q \\ \frac{q^2}{w-B} + \frac{g}{2}(w^2 - 2wB) \end{pmatrix}_x = \begin{pmatrix} 0 \\ -gwB_x \end{pmatrix}. \quad (2.3)$$

We introduce a uniform grid $x_\alpha := \alpha\Delta x$ with a finite volume cell denoted by $C_j := [x_{j-\frac{1}{2}}, x_{j+\frac{1}{2}}]$, in which a cell average of the computed solution,

$$\bar{\mathbf{U}}_j(t) \approx \frac{1}{\Delta x} \int_{C_j} \mathbf{U}(x, t) dx, \quad (2.4)$$

is assumed to be known at a given time t . The cell averages are evolved in time based on the following equation:

$$\frac{d}{dt} \bar{\mathbf{U}}_j(t) = -\frac{\mathbf{H}_{j+\frac{1}{2}}(t) - \mathbf{H}_{j-\frac{1}{2}}(t)}{\Delta x} + \bar{\mathbf{S}}_j(t), \quad (2.5)$$

where $\mathbf{H}_{j\pm\frac{1}{2}}$ are the central-upwind numerical fluxes from [45] given by

$$\mathbf{H}_{j+\frac{1}{2}}(t) = \frac{a_{j+\frac{1}{2}}^+ \mathbf{F}(\mathbf{U}_{j+\frac{1}{2}}^-, B_{j+\frac{1}{2}}^-) - a_{j+\frac{1}{2}}^- \mathbf{F}(\mathbf{U}_{j+\frac{1}{2}}^+, B_{j+\frac{1}{2}}^+)}{a_{j+\frac{1}{2}}^+ - a_{j+\frac{1}{2}}^-} + \frac{a_{j+\frac{1}{2}}^+ a_{j+\frac{1}{2}}^-}{a_{j+\frac{1}{2}}^+ - a_{j+\frac{1}{2}}^-} \left[\mathbf{U}_{j+\frac{1}{2}}^+ - \mathbf{U}_{j+\frac{1}{2}}^- \right], \quad (2.6)$$

with $\mathbf{F}(\mathbf{U}, B) := \left(q, qu + \frac{g}{2}(w^2 - 2wB) \right)^\top$. Note, that, in contrast to the general central-upwind scheme in (1.5) and the numerical scheme from [50], the numerical fluxes now make use of B^\pm which are the left and right point values of the computed solution at the cell interface $x = x_{j+\frac{1}{2}}$. The cell averages of the geometric source term are given by

$$\bar{\mathbf{S}}_j(t) \approx \frac{1}{\Delta x} \int_{C_j} \mathbf{S}(\mathbf{U}, B) dx. \quad (2.7)$$

where $\mathbf{S} = (0, -gwB_x)^\top$. For the rest of this chapter, we will drop the notation t for time dependence for simplicity where it is appropriate. The construction of the numerical scheme will be complete once the numerical fluxes in $\mathbf{H}_{j\pm\frac{1}{2}}$ in (2.6) and the source term $\bar{\mathbf{S}}_j$ in (2.7) are computed such that the resulting method is well-balanced and positivity preserving.

2.1.1 Reconstruction of \mathbf{U}

In equation (2.6), $\mathbf{U}_{j\pm\frac{1}{2}}^\pm$ are the left and right point values of the computed solution at the cell interface $x = x_{j+\frac{1}{2}}$. For our scheme to be second-order, the point values should be calculated using piecewise linear reconstructions

$$\tilde{\mathbf{U}}(x) = \sum_j \left[\bar{\mathbf{U}}_j + (\mathbf{U}_x)_j(x - x_j) \right] \cdot \chi_{C_j}(x), \quad (2.8)$$

obtained at cell interfaces $x = x_{j+\frac{1}{2}}$ by

$$\mathbf{U}_{j+\frac{1}{2}}^+ = \bar{\mathbf{U}}_{j+1} - \frac{\Delta x}{2} (\mathbf{U}_x)_{j+1}, \quad \mathbf{U}_{j+\frac{1}{2}}^- = \bar{\mathbf{U}}_j + \frac{\Delta x}{2} (\mathbf{U}_x)_j. \quad (2.9)$$

In (2.8) and (2.9), recall, $\chi_{C_j}(x)$ is the characteristic function of the interval C_j , and $(\mathbf{U}_x)_j$ are the numerical derivatives, which should be computed using a nonlinear limiter in order to minimize oscillations. In all numerical experiments in Section 2.4, we use the generalized minmod limiter given in (1.93) and (1.94).

2.1.2 Piecewise Linear Reconstruction of B

The primary differences in our numerical scheme to the central-upwind scheme in [50] stem from our use of a generally piecewise discontinuous linear reconstruction for the bottom topography B instead of a continuous piecewise linear approximation. This reconstruction is obtained using the same generally piecewise discontinuous linear reconstruction as in (2.8) and (2.9) given by

$$\tilde{B}(x) = \sum_j [B(x_j) + (B_x)_j(x - x_j)] \cdot \chi_{C_j}(x) \quad (2.10)$$

to obtain the point values $B_{j+\frac{1}{2}}^\pm$ at $x = x_{j+\frac{1}{2}}$:

$$B_{j+\frac{1}{2}}^+ = \bar{B}_{j+1} - \frac{\Delta x}{2}(B_x)_{j+1}, \quad B_{j+\frac{1}{2}}^- = \bar{B}_j + \frac{\Delta x}{2}(B_x)_j. \quad (2.11)$$

2.1.3 Local Speeds of Propagation

The one-sided local speeds of propagation $a_{j+\frac{1}{2}}^\pm$ used in the central-upwind numerical flux (2.6) are obtained from the largest and smallest eigenvalues of the Jacobian matrix $\frac{\partial \mathbf{F}}{\partial \mathbf{U}}$ given by

$$\frac{\partial \mathbf{F}}{\partial \mathbf{U}} = \begin{bmatrix} 0 & 1 \\ -\frac{q^2}{(w-B)^2} + \frac{g}{2}(2w - wB) & \frac{2q}{w-B} \end{bmatrix}. \quad (2.12)$$

The characteristic equation reduces to $\lambda^2 - 2u\lambda + u^2 - gh = 0$, which can be solved analytically to obtain the eigenvalues $\lambda_1 = u + \sqrt{gh}$ and $\lambda_2 = u - \sqrt{gh}$. Thus, the one-sided local speeds of propagation are

$$\begin{aligned} a_{j+\frac{1}{2}}^+ &= \max \left\{ u_{j+\frac{1}{2}}^+ + \sqrt{gh_{j+\frac{1}{2}}^+}, u_{j+\frac{1}{2}}^- + \sqrt{gh_{j+\frac{1}{2}}^-}, 0 \right\}, \\ a_{j+\frac{1}{2}}^- &= \min \left\{ u_{j+\frac{1}{2}}^+ - \sqrt{gh_{j+\frac{1}{2}}^+}, u_{j+\frac{1}{2}}^- - \sqrt{gh_{j+\frac{1}{2}}^-}, 0 \right\}. \end{aligned} \quad (2.13)$$

2.2 Well-Balanced Quadrature for the Geometric Source Terms

To ensure the method is well-balanced, exactly preserving our chosen lake-at-rest steady-state ($\bar{q} = 0$ and $\bar{w} = \text{Constant}$), a special quadrature should be used to discretize the second component of the source term $\bar{S}_j^{(2)}$ in (2.7). A proper discretization should guarantee that the right hand side of (2.5) vanishes at the lake-at-rest steady-state by balancing the numerical

fluxes and source term. The numerical fluxes at the discrete level are given by:

$$\begin{aligned}
& \frac{H_{j+\frac{1}{2}}^{(2)} - H_{j-\frac{1}{2}}^{(2)}}{\Delta x} = \\
& \frac{1}{\Delta x} \left[\frac{a^+ \left[\left(\frac{q^2}{w-B} \right)^- + g \left(\frac{1}{2} w^2 - wB \right)^- \right] - a^- \left[\left(\frac{q^2}{w-B} \right)^+ + g \left(\frac{1}{2} w^2 - wB \right)^+ \right]}{a^+ - a^-} \right]_{j+\frac{1}{2}} \\
& + \frac{a_{j+\frac{1}{2}}^+ a_{j+\frac{1}{2}}^-}{a_{j+\frac{1}{2}}^+ - a_{j+\frac{1}{2}}^-} [q^+ - q^-]_{j+\frac{1}{2}} \\
& - \frac{1}{\Delta x} \left[\frac{a^+ \left[\left(\frac{q^2}{w-B} \right)^- + g \left(\frac{1}{2} w^2 - wB \right)^- \right] - a^- \left[\left(\frac{q^2}{w-B} \right)^+ + g \left(\frac{1}{2} w^2 - wB \right)^+ \right]}{a^+ - a^-} \right]_{j-\frac{1}{2}} \\
& + \frac{a_{j-\frac{1}{2}}^+ a_{j-\frac{1}{2}}^-}{a_{j-\frac{1}{2}}^+ - a_{j-\frac{1}{2}}^-} [q^+ - q^-]_{j-\frac{1}{2}}. \tag{2.14}
\end{aligned}$$

Since \bar{q} is a constant zero, $q_{j+\frac{1}{2}}^\pm = q_{j-\frac{1}{2}}^\pm = 0$. Applying this condition to (2.14), we have

$$\begin{aligned}
& \frac{H_{j+\frac{1}{2}}^{(2)} - H_{j-\frac{1}{2}}^{(2)}}{\Delta x} = \\
& \frac{1}{\Delta x} \left[\frac{a^+ \left[\left(\frac{q^2}{w-B} \right)^- + g \left(\frac{1}{2} w^2 - wB \right)^- \right] - a^- \left[\left(\frac{q^2}{w-B} \right)^+ + g \left(\frac{1}{2} w^2 - wB \right)^+ \right]}{a^+ - a^-} \right]_{j+\frac{1}{2}} \\
& + \frac{a_{j+\frac{1}{2}}^+ a_{j+\frac{1}{2}}^-}{a_{j+\frac{1}{2}}^+ - a_{j+\frac{1}{2}}^-} [q^+ - q^-]_{j+\frac{1}{2}} \\
& - \frac{1}{\Delta x} \left[\frac{a^+ \left[\left(\frac{q^2}{w-B} \right)^- + g \left(\frac{1}{2} w^2 - wB \right)^- \right] - a^- \left[\left(\frac{q^2}{w-B} \right)^+ + g \left(\frac{1}{2} w^2 - wB \right)^+ \right]}{a^+ - a^-} \right]_{j-\frac{1}{2}} \\
& + \frac{a_{j-\frac{1}{2}}^+ a_{j-\frac{1}{2}}^-}{a_{j-\frac{1}{2}}^+ - a_{j-\frac{1}{2}}^-} [q^+ - q^-]_{j-\frac{1}{2}}. \tag{2.15}
\end{aligned}$$

In addition, $\bar{w} = \text{Constant}$, therefore $w_{j+\frac{1}{2}}^{\pm} = w_{j-\frac{1}{2}}^{\pm} = \bar{w}_j$, and (2.15) further reduces to

$$\begin{aligned}
\frac{H_{j+\frac{1}{2}}^{(2)}(t) - H_{j-\frac{1}{2}}^{(2)}(t)}{\Delta x} &= \frac{g}{\Delta x} \left[\frac{a^+ [\frac{1}{2}(\bar{w})^2 - \bar{w}B^-] - a^- [\frac{1}{2}(\bar{w})^2 - \bar{w}B^+]}{a^+ - a^-} \right]_{j+\frac{1}{2}} \\
&\quad - \frac{g}{\Delta x} \left[\frac{a^+ [\frac{1}{2}(\bar{w})^2 - \bar{w}B^-] - a^- [\frac{1}{2}(\bar{w})^2 - \bar{w}B^+]}{a^+ - a^-} \right]_{j-\frac{1}{2}}, \\
&= \frac{g}{\Delta x} \left[\frac{(a^+ - a^-) \frac{1}{2} \bar{w}^2}{a^+ - a^-} \right]_{j+\frac{1}{2}} + \frac{g}{\Delta x} \left[\frac{-\bar{w}B^- a^+ + \bar{w}B^+ a^-}{a^+ - a^-} \right]_{j+\frac{1}{2}} \\
&\quad - \frac{g}{\Delta x} \left[\frac{(a^+ - a^-) \frac{1}{2} \bar{w}^2}{a^+ - a^-} \right]_{j-\frac{1}{2}} - \frac{g}{\Delta x} \left[\frac{-\bar{w}B^- a^+ + \bar{w}B^+ a^-}{a^+ - a^-} \right]_{j-\frac{1}{2}}, \\
&= \frac{g\bar{w}_j}{\Delta x} \left[\frac{-B_{j+\frac{1}{2}}^- a_{j+\frac{1}{2}}^+ + B_{j+\frac{1}{2}}^+ a_{j+\frac{1}{2}}^-}{a_{j+\frac{1}{2}}^+ - a_{j+\frac{1}{2}}^-} - \frac{-B_{j-\frac{1}{2}}^- a_{j-\frac{1}{2}}^+ + B_{j-\frac{1}{2}}^+ a_{j-\frac{1}{2}}^-}{a_{j-\frac{1}{2}}^+ - a_{j-\frac{1}{2}}^-} \right].
\end{aligned}$$

Therefore the numerical fluxes and source term will balance, if the second component of the source term is discretized as follows:

$$\bar{S}_j^{(2)} \approx -\frac{g\bar{w}_j}{\Delta x} \left(\frac{a_{j+\frac{1}{2}}^+ B_{j+\frac{1}{2}}^- - a_{j+\frac{1}{2}}^- B_{j+\frac{1}{2}}^+}{a_{j+\frac{1}{2}}^+ - a_{j+\frac{1}{2}}^-} - \frac{a_{j-\frac{1}{2}}^+ B_{j-\frac{1}{2}}^- - a_{j-\frac{1}{2}}^- B_{j-\frac{1}{2}}^+}{a_{j-\frac{1}{2}}^+ - a_{j-\frac{1}{2}}^-} \right). \quad (2.16)$$

2.3 Positivity Preserving Property

To guarantee the positivity of the numerical scheme such that the water height is greater than or equal to zero, we implement two additional changes to the central-upwind scheme in Section 1.5. First, in Section 2.3.1, we will adjust any non-physical negative values obtained in the reconstruction of \tilde{w} . Second, in Section 2.3.2, we implement a draining time-step, which further restricts the time evolution to limit the amount of water leaving a particular cell.

2.3.1 Positivity Correction for \tilde{w}

When \tilde{w} is reconstructed using (2.8), some of the point values $w_{j\pm\frac{1}{2}}^{\pm}$, obtained in (2.9), may be smaller than the corresponding point values $B_{j\pm\frac{1}{2}}^{\pm}$, which will lead to negative point values for h . Following [50], we perform a positivity correction for the reconstruction of \tilde{w} according to

the following simple algorithm:

$$\begin{aligned} \text{if } w_{j+\frac{1}{2}}^- < B_{j+\frac{1}{2}}^-, \text{ then take } (w_x)_j &:= \frac{B_{j+\frac{1}{2}}^- - \bar{w}_j}{\Delta x/2}, \\ \implies w_{j+\frac{1}{2}}^- &= B_{j+\frac{1}{2}}^-, \quad w_{j-\frac{1}{2}}^+ = 2\bar{w}_j - B_{j+\frac{1}{2}}^-, \end{aligned} \quad (2.17)$$

$$\begin{aligned} \text{if } w_{j-\frac{1}{2}}^+ < B_{j-\frac{1}{2}}^+, \text{ then take } (w_x)_j &:= \frac{\bar{w}_j - B_{j-\frac{1}{2}}^+}{\Delta x/2}, \\ \implies w_{j+\frac{1}{2}}^- &= 2\bar{w}_j - B_{j-\frac{1}{2}}^+, \quad w_{j-\frac{1}{2}}^+ = B_{j-\frac{1}{2}}^+, \end{aligned} \quad (2.18)$$

noticing that this correction algorithm works as long as $\bar{w}_j > \bar{B}_j$.

After the point values $w_{j+\frac{1}{2}}^\pm$ are corrected, we compute the point values of the water height as follows:

$$h_{j+\frac{1}{2}}^\pm := w_{j+\frac{1}{2}}^\pm - B_{j+\frac{1}{2}}^\pm. \quad (2.19)$$

2.3.1.1 Velocity Desingularization

In cases where the height of the water column is approximately zero ($h \approx 0$), in order to avoid division by zero (or by a very small number), we desingularize the computation of the velocity point values needed in (2.6) by setting

$$u_{j+\frac{1}{2}}^\pm = \frac{2h_{j+\frac{1}{2}}^\pm q_{j+\frac{1}{2}}^\pm}{(h_{j+\frac{1}{2}}^\pm)^2 + \max\left[(h_{j+\frac{1}{2}}^\pm)^2, \varepsilon^2\right]}, \quad (2.20)$$

where ε is a small desingularization parameter. In all of our numerical examples, we have used $\varepsilon = 10^{-5}$. For more details on different desingularization strategies, see the discussions in [14,50]. For consistency, the desingularized velocities should be used to modify the corresponding values of the discharge by

$$q_{j+\frac{1}{2}}^\pm = h_{j+\frac{1}{2}}^\pm \cdot u_{j+\frac{1}{2}}^\pm.$$

2.3.2 Time Evolution and the Draining Time-Step

The central-upwind semi-discretization given in (2.5) is a system of ODEs which should be integrated by a sufficiently accurate and stable ODE solver. We first note that the bottom topography function B is independent of time, and, therefore, the forward Euler time step for the first component in (2.5) can be written in the following form:

$$\bar{h}_j^{n+1} = \bar{h}_j^n - \frac{\Delta t}{\Delta x} \left(H_{j+\frac{1}{2}}^{(1)} - H_{j-\frac{1}{2}}^{(1)} \right), \quad (2.21)$$

where Δt is the time step constrained by the CFL condition

$$\Delta t \leq \frac{1}{2} \frac{\Delta x}{\max_j |a_{j+\frac{1}{2}}^\pm|}. \quad (2.22)$$

In order to guarantee the positivity of \bar{h}_j^{n+1} , provided $\bar{h}_j^n \geq 0 \ \forall j$, we adopt a draining time-step technique from [7, 8]. To this end, we introduce the draining time step

$$\Delta t_j^{drain} := \frac{\Delta x \bar{h}_j^n}{\max \left(0, H_{j+\frac{1}{2}}^{(1)} \right) + \max \left(0, -H_{j-\frac{1}{2}}^{(1)} \right)}, \quad (2.23)$$

which describes the time when the water contained in cell C_j at the beginning of the time step has left via the outflow fluxes. We now replace the evolution step in (2.21) by

$$\bar{h}_j^{n+1} = \bar{h}_j^n - \frac{\Delta t_{j+\frac{1}{2}} H_{j+\frac{1}{2}}^{(1)} - \Delta t_{j-\frac{1}{2}} H_{j-\frac{1}{2}}^{(1)}}{\Delta x}, \quad (2.24)$$

where the time step $\Delta t_{j+\frac{1}{2}}$ is defined as

$$\Delta t_{j+\frac{1}{2}} = \min \left(\Delta t, \Delta t_i^{drain} \right), \quad i = j + \frac{1}{2} - \frac{\text{sgn} \left(H_{j+\frac{1}{2}}^{(1)} \right)}{2}, \quad (2.25)$$

with Δt satisfying (2.22). Thus, we have $\bar{h}_j^{n+1} \geq 0$, for all j in the numerical scheme by construction.

2.4 Numerical Examples

In this section, we present three numerical examples. In all of the numerical simulations, the bottom topography is reconstructed according to (2.10) with $(B_x)_j$ computed using the minmod limiter with $\theta = 1$. The equilibrium variables w and q are reconstructed using the minmod limiter with either $\theta = 1.3$ (Examples 1 and 2) or $\theta = 1$ (Example 3, in which we select the most diffusive version of the limiter to limit the oscillations). In all of the examples below, we use absorbing boundary conditions on both ends of the domain.

2.4.1 Example 1—Small Perturbation of Steady State

In this problem, taken from [50], we study propagation of a small perturbation of the steady-state solution that contains nearly dry areas. The computational domain is $[-1, 1]$, the gravi-

tational constant $g = 1$, the initial data are

$$w(x, 0) = \begin{cases} 1.001, & 0.1 \leq x \leq 0.2, \\ 1, & \text{otherwise,} \end{cases} \quad u(x, 0) \equiv 0,$$

and the bottom topography is given by

$$B(x) = \begin{cases} 10(x - 0.3), & 0.3 \leq x \leq 0.4, \\ 1 - 0.0025 \sin^2(25\pi(x - 0.4)), & 0.4 \leq x \leq 0.6, \\ -10(x - 0.7), & 0.6 \leq x \leq 0.7, \\ 0, & \text{otherwise.} \end{cases}$$

A small perturbation of the “lake-at-rest” steady state initially located at $x \in [0.1, 0.2]$ is split into two parts propagating in the opposite directions. When the right-going wave propagates over the oscillating part of the bottom, above which the initial water depth is very small ($x \in [0.4, 0.6]$), a complicated surface wave structure is developed. In Figure 2.1, we compare the solutions obtained by the proposed well-balanced central-upwind scheme and its non-well-balanced version, obtained by replacing the well-balanced quadrature (3.86) with the midpoint one,

$$\bar{S}_j^{(2)} \approx -g\bar{w}_j B_x(x_j),$$

and increasing the value of the desingularization parameter ε from 10^{-5} to 10^{-4} . The latter adjustment is needed to improve the efficiency of the non-well-balanced version of the scheme. Both solutions are computed until the final time $t = 1$ using $N = 400$ (top row) and $N = 1600$ (bottom row) uniform cells. As one can see, the non-well-balanced solution is very oscillatory, and the magnitude of oscillations decrease quite slowly when the mesh is refined. More details can be seen in Figure 2.1 (right column) where we zoom into the low water depth region $x \in [0.395, 0.5]$.

2.4.2 Example 2—Riemann Problem with Unique Solution

In this example, we consider the Riemann problem from [57, Test 7], where the system (2.1) is solved with $g = 9.8$ and the following Riemann data:

$$B(x) = \begin{cases} 1.1, & x < 0, \\ 1, & x > 0, \end{cases} \quad h(x, t) = \begin{cases} 1, & x < 0, \\ 0.8, & x > 0, \end{cases} \quad u(x, t) = \begin{cases} 2, & x < 0, \\ 4, & x > 0. \end{cases} \quad (2.26)$$

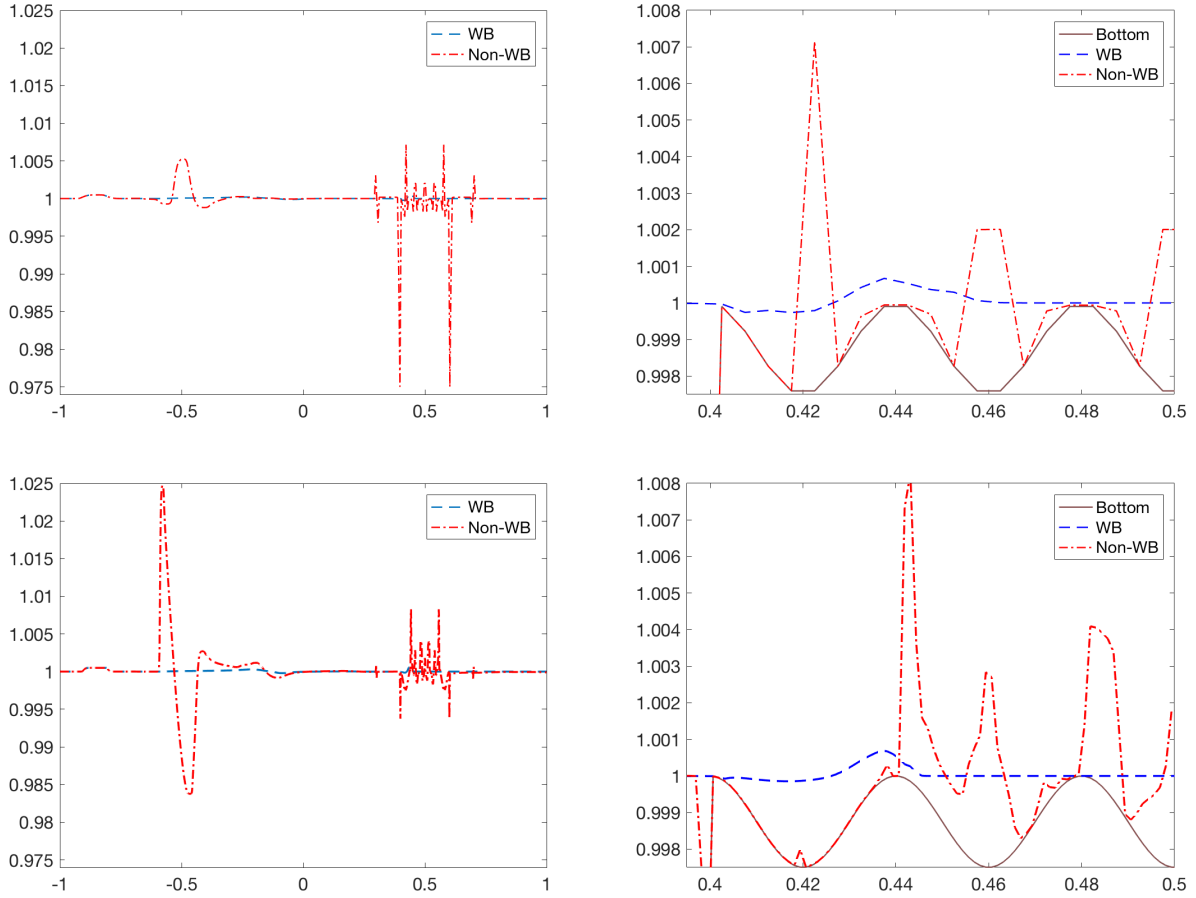


Figure 2.1: Example 1: Solution (w) computed by the well-balanced and non-well-balanced central upwind schemes using $N = 400$ (top row) and $N = 1600$ (bottom row) uniform cells. Right column: zoom into the region $x \in [0.395, 0.5]$.

In [57], the exact solution of the initial value problem (IVP) given by (2.1) and (2.26) was obtained, and it was also shown that the Godunov-type scheme based on the exact solution of the Riemann problem fails at this test.

The central-upwind scheme proposed in this chapter is, on the other hand, capable of accurately capturing the exact solution of the IVP given by (2.1) and (2.26). To demonstrate this, we compute the numerical solution until the final time $t = 0.03$ on two uniform grids with $\Delta x = 0.004$ and 0.001 and compare the obtained solution with a reference one computed with $\Delta x = 0.00004$. We plot the computed water depth h and velocity u in Figure 2.2, where one can clearly observe the convergence towards the reference solution, which agrees very well with the exact one (see [57, Test 7]).

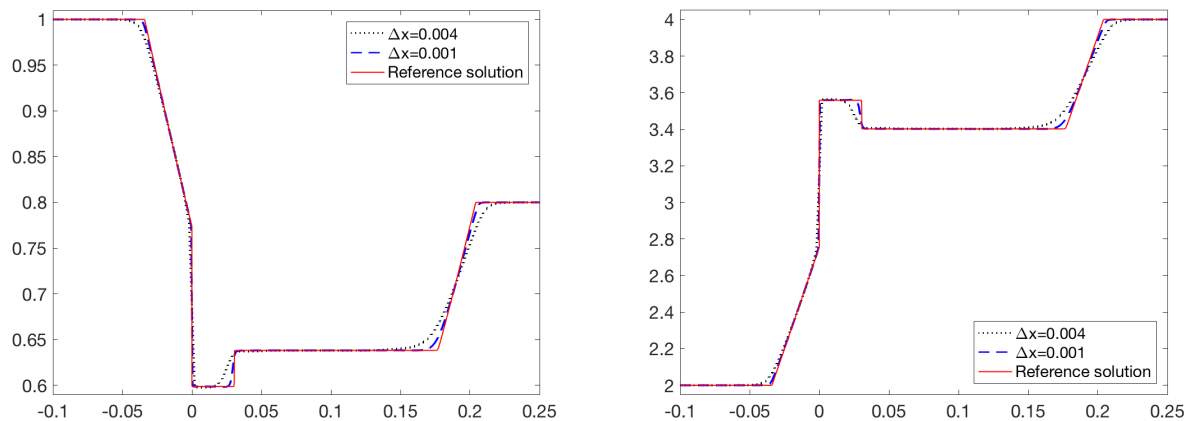


Figure 2.2: Example 2: Solution (h on the left and u on the right) computed using $\Delta x = 0.004$ and 0.001 and compared with the reference solution.

2.4.3 Example 3—Riemann Problem with Multiple Solutions

In the final example, we consider the Riemann problem from [57, Test 6], where the system (2.1) is solved with $g = 9.8$ and different Riemann data:

$$B(x) = \begin{cases} 1, & x < 0, \\ 1.2, & x > 0, \end{cases} \quad h(x, t) = \begin{cases} 0.2, & x < 0, \\ 0.75904946, & x > 0, \end{cases} \quad u(x, t) = \begin{cases} 5, & x < 0, \\ 1.3410741, & x > 0. \end{cases} \quad (2.27)$$

As it was shown in [57], the IVP given by (2.1) and (2.27) admits three distinct analytic solutions, and Godunov-type upwind schemes based on different Riemann problem solvers converge to different analytic solutions. We compute the numerical solution until the final time $t = 0.1$ on three uniform grids with $\Delta x = 0.004$, 0.001, and 0.00004 using both the central-upwind scheme proposed in this chapter and the central-upwind scheme from [50]. The results are plotted in Figures 2.3 and 2.4, respectively. As one can see, the schemes converge to different limits, each of which agrees well with the second and third analytic solutions from [57, Test 6].

2.5 Conclusion

In this chapter, we implemented a second-order, well-balanced, positivity preserving central-upwind scheme for the 1-D shallow water equations with discontinuous bottom topography. The central-upwind scheme presented relies on a discontinuous piecewise linear reconstruction of the bottom topography function B , and thus it is suitable for functions containing large jumps and can be extended to models with moving, time-dependent bottom topography function B . In

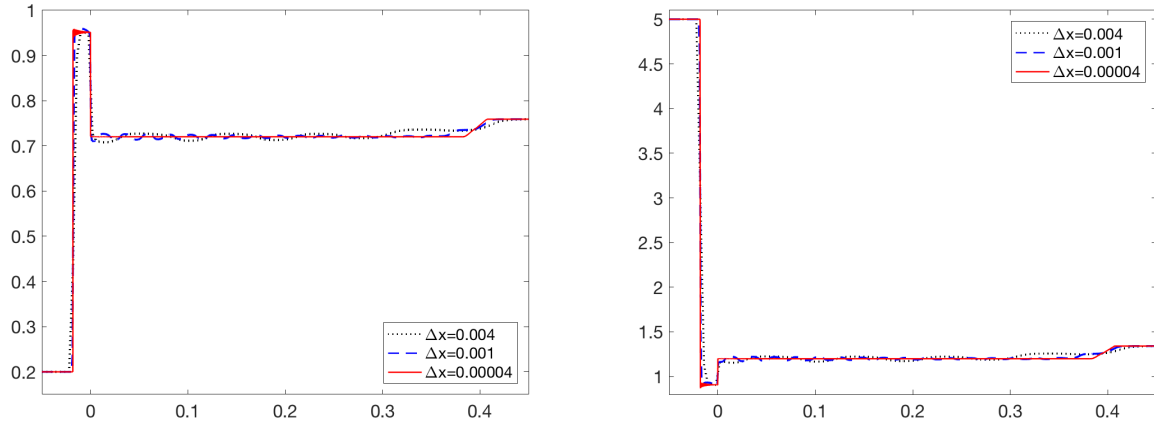


Figure 2.3: Example 3: Solution (h on the left and u on the right) computed by the proposed central-upwind scheme using $\Delta x = 0.004, 0.001$, and 0.00004 .

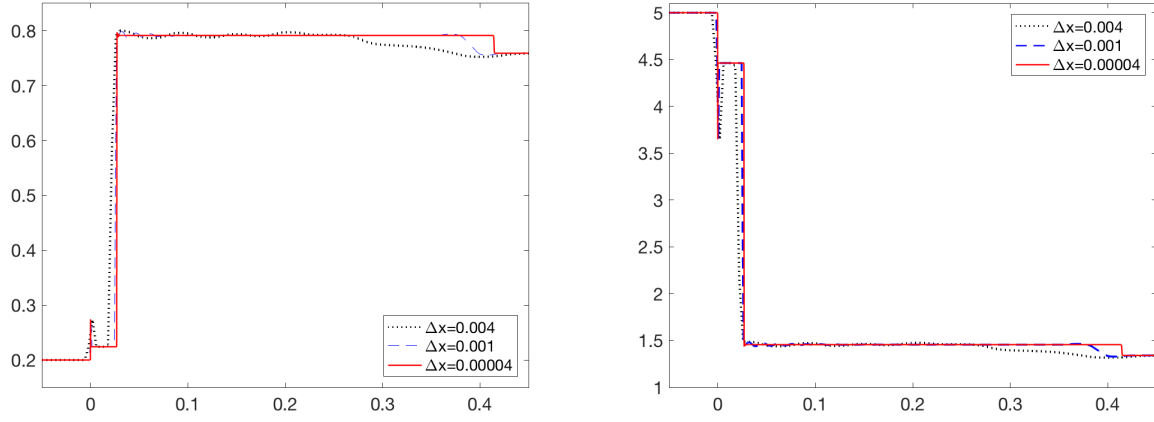


Figure 2.4: Example 3: Solution (h on the left and u on the right) computed by the central-upwind scheme from [50] using $\Delta x = 0.004, 0.001$, and 0.00004 .

Section 2.4, we presented three numerical results for our scheme. In the first, we demonstrated the numerical scheme presented in this chapter is capable of handling a small perturbation of steady state, with the computed solution remaining smooth, compared to the oscillations present in the non well-balanced computed solution. The next two examples illustrate Riemann problems with either a unique solution or multiple solutions. The numerical scheme in this chapter is capable of accurately converging to the exact solution of the initial value problem and to one of the analytic solutions in the last example.

Part II

Morphodynamic: Exner Equation to Govern Bed Load Sediment Transport

Chapter 3

1-D Shallow Water Equations with Exner Equation

In this chapter, we discuss numerical methods to solve the 1-D system of shallow water equations with a 1-D Exner equation to govern sediment transport. Within this chapter some redundancies are left in for the sake of the reader in understanding and implementing these methods.

We start with the 1-D system of shallow water equations represented by

$$\begin{pmatrix} h \\ hu \end{pmatrix}_t + \begin{pmatrix} hu \\ hu^2 + \frac{g}{2}h^2 \end{pmatrix}_x = \begin{pmatrix} 0 \\ -ghB_x \end{pmatrix}, \quad (3.1)$$

with 1-D Exner equation to govern sediment transport given by

$$B_t + (\xi q_b)_x = 0, \quad (3.2)$$

where the variable $\xi = \frac{1}{1-\epsilon}$ is a constant, with ϵ representing the porosity of the sediment layer. The closer to zero ϵ is, the larger the particles that comprise the sediment.

Similarly to Chapter 2, we wish to rewrite (3.1) in terms of the equilibrium variables for the shallow water equations (w, q) . However, since the bottom topography function B is no longer time independent, $h_t \neq w_t$. To rewrite the system, we add (3.2) to the first equation of (3.1), obtaining the equation in terms of w . In addition, we rearrange the second equation of the shallow water system, and (3.1) becomes

$$\begin{pmatrix} w \\ q \end{pmatrix}_t + \begin{pmatrix} q + \xi q_b \\ \frac{q^2}{w-B} + \frac{g}{2}(w^2 - 2wB) \end{pmatrix}_x = \begin{pmatrix} 0 \\ -gwB_x \end{pmatrix}. \quad (3.3)$$

Recall, q_b is the sediment flux, which depends on various water and sediment properties and can be represented by a multitude of models (see Section 1.3.2). For our numerical scheme, the sediment flux represents the bed load sediment transport, and we use the flux proposed by Grass (1.79),

$$q_b = Au (u^2)^{(m-1)/2}, \quad (3.4)$$

where A is a non-dimensional constant which accounts for the effects of sediment grain size and kinematic viscosity. The value of A is in $[0, 1]$, and the closer A is to zero, the weaker the interaction between the sediment and fluid is. The constant A is often computed from experimental data and m represents a constant value $1 \leq m \leq 4$. In our numerical experiments, we will use $m = 3$.

With the addition of the 1-D Exner equation to the 1-D system of shallow water equations, the values for the local speeds of propagation used in our numerical scheme, calculated by the largest and smallest eigenvalues of the Jacobian of the system (3.3) and (3.2), will be different than in the previous chapter. We therefore recalculate the eigenvalues in the following section and show they are real and distinct.

3.1 Eigenvalues for the Jacobian of the Shallow Water System with Exner Equation

For simplicity of the computations we use the primitive variables $\mathbf{U}_p = (h, u, B)^\top$, and $\mathbf{F}_p = (hu, hu^2 + \frac{1}{2}gh^2, Au^3)$ to obtain the Jacobian given by

$$\frac{\partial \mathbf{F}_p}{\partial \mathbf{U}_p} = \begin{bmatrix} u & h & 0 \\ g & u & g \\ 0 & 3\xi Au^2 & 0 \end{bmatrix}. \quad (3.5)$$

The eigenvalues of this system, $\lambda^{(1)} < \lambda^{(2)} < \lambda^{(3)}$, are the roots of the cubic equation

$$P(\lambda, h, u) = \lambda^3 - 2u\lambda^2 + [u^2 - 3\xi Ag u^2 - gh]\lambda + 3\xi Ag u^3 = 0. \quad (3.6)$$

These roots are not easy to compute analytically, but we can prove, that with this formulation of the sediment flux, that the roots of $P(\lambda, h, u)$ are real using a formula for factoring a cubic in [80]. For a cubic equation of the form

$$P(x) = \lambda^3 + a_2\lambda^2 + a_1\lambda + a_0, \quad (3.7)$$

we let

$$Q = \frac{1}{9}(3a_1 - a_2^2), \quad R = \frac{1}{54}(9a_2a_1 - 27a_0 - 2a_2^3), \quad \Theta = \frac{R}{\sqrt{-Q^3}}. \quad (3.8)$$

If we let $D = Q^3 + R^2$ be the polynomial discriminant, which has an opposite sign and differs by a constant to the standard discriminate of a cubic function, then we have three cases to consider. If

1. $D > 0$, then one root is real and two are complex,
2. $D = 0$, then all roots are real and two are equal,
3. $D < 0$, all roots are real and distinct.

In the case $D < 0$, all the roots of (3.7) are real, distinct, and given by

$$\lambda^{(1)} = 2\sqrt{-Q} \cos\left(\frac{1}{3}\Theta\right) - \frac{1}{3}a_1, \quad (3.9)$$

$$\lambda^{(2)} = 2\sqrt{-Q} \cos\left(\frac{1}{3}(\Theta + 2\pi)\right) - \frac{1}{3}a_1, \quad (3.10)$$

$$\lambda^{(3)} = 2\sqrt{-Q} \cos\left(\frac{1}{3}(\Theta + 4\pi)\right) - \frac{1}{3}a_1. \quad (3.11)$$

Using (3.6), the coefficients of the cubic equation are given by

$$a_2 = -2u, \quad a_1 = u^2 - 3\xi A g u^2 - g h, \quad a_0 = 3\xi A g u^3.$$

Substituting this into (3.8) results in

$$\begin{aligned} Q &= \frac{1}{9}(3a_1 - a_2^2), \\ &= \frac{1}{9}(3(u^2 - 3\xi A g u^2 - g h) - (-2u)^2), \\ &= \frac{1}{9}(3u^2 - 9\xi A g u^2 - 3g h - 4u^2), \\ &= -\frac{1}{9}(9\xi A g u^2 + 3g h + u^2), \end{aligned}$$

and

$$\begin{aligned} R &= \frac{1}{54}(9a_2a_1 - 27a_0 - 2a_2^3), \\ &= \frac{1}{54}(9(-2u)(u^2 - 3\xi A g u^2 - g h) - 27(3\xi A g u^3) - 2(-2u)^3), \\ &= \frac{1}{54}(-18u^3 + 54\xi A g u^3 + 18g h u - 81\xi A g u^3 + 16u^3), \\ &= \frac{u}{54}(18g h - 2u^2 - 27\xi A g u^2). \end{aligned}$$

Plugging Q and R into our formula for $D = Q^3 + R^2$, we have

$$D = \frac{g}{108} [8gu^2h^2 - 9g\xi^2A^2u^6 - 4hu^4 - 60hg\xi Au^4 - 4g^2h^3 - 108g^2\xi^3A^3u^8 - 36g^2h^2\xi^2A^2u^4 - 108g^2h\xi^2A^2u^4].$$

In order to show that all the roots are real and distinct, we need to show that $D < 0$, or

$$8gu^2h^2 < 9g\xi^2A^2u^6 + 4hu^4 + 60hg\xi Au^4 + 4g^2h^3 + 108g^2\xi^3A^3u^8 + 36g^2h^2\xi^2A^2u^4 + 108g^2h\xi^2A^2u^4. \quad (3.12)$$

From the physical assumptions on our system that the water height $h \geq 0$, all of the terms in (3.12) are non-negative. Since A is a small constant, we will lump all of the terms with A together to form a non-negative term, A_{all} . Thus,

$$\begin{aligned} 8gu^2h^2 &< 4hu^4 + 4g^2h^3 + A_{all}, \\ 0 &< 4hu^4 + 4g^2h^3 - 8gu^2h^2 + A_{all}, \\ 0 &< 4h(u^4 + g^2h^2 - 2gu^2h) + A_{all}, \\ 0 &< 4h(u^2 - gh)^2 + A_{all}. \end{aligned}$$

Hence, the eigenvalues of $P(\lambda, h, u)$ will be real and distinct.

3.2 Time Evolution

With the eigenvalues for the system in hand, a straightforward implementation of a central-upwind scheme for the system (3.3) and (3.2), as in Section 1.5, which uses the largest and smallest eigenvalues of the Jacobian for the local speeds of propagation in the numerical scheme, leads to numerical difficulties. In particular, the computed solution for the bottom B is overly diffusive on a coarse grid. An example of this will be shown in Example 3.8.4 in Section 3.8. To better understand where the numerical difficulties are coming from, let us first consider the eigenvalues of the system (3.3) and (3.2). As the value for the sediment interaction A is reduced, the eigenvalues $\lambda^{(1)}$ and $\lambda^{(3)}$ become close to the eigenvalue of the 1-D shallow water system (2.3). To estimate the last eigenvalue $\lambda^{(2)}$, we find the approximate value is given by Au^3/B and is close to zero. Typically, we found that $\lambda^{(2)} \ll \max(|\lambda^{(1)}|, |\lambda^{(3)}|)$, corresponding to the most common physical case in which water waves propagate at a much faster speed than the bottom sediment waves [19].

When the central-upwind scheme given in Section 1.5 is implemented, the values of a^\pm are too large, and the second term in the central-upwind numerical fluxes (1.89) results in extra

diffusion. The main idea of the numerical scheme presented here is to replace the local speeds of propagation a^\pm by different local speeds of propagation depending on whether we are evolving the shallow water equations or the Exner equation. When evolving the shallow water equations (3.3), we use the new local speeds of propagation \hat{a}^\pm , and, when evolving the Exner equation (3.2), we use the new local speeds of propagation \hat{c}^\pm . These values are defined to be

$$\hat{a}^+ = \max \left\{ \lambda^{(1)+}, \lambda^{(3)+}, \lambda^{(1)-}, \lambda^{(3)-}, 0 \right\}, \quad (3.13)$$

$$\hat{a}^- = \min \left\{ \lambda^{(1)+}, \lambda^{(3)+}, \lambda^{(1)-}, \lambda^{(3)-}, 0 \right\}, \quad (3.14)$$

and

$$\hat{c}^+ = \max \left\{ \lambda^{(2)+}, \lambda^{(2)-}, 0 \right\}, \quad (3.15)$$

$$\hat{c}^- = \min \left\{ \lambda^{(2)+}, \lambda^{(2)-}, 0 \right\}. \quad (3.16)$$

Recall that the plus/minus notation refers to the left and right point values at the interface of the computational cells.

Now, the new local speeds of propagation for the shallow water equations \hat{a}^\pm will depend only on the largest and smallest eigenvalues associated with the water waves, and the new local speeds of propagation for the Exner equations \hat{c}^\pm will depend only on the largest and smallest eigenvalues associated with the sediment waves. We note that, in literature, see e.g. [18], one practice is to use the eigenvalues of the shallow water system $u \pm \sqrt{gh}$ for the local speeds of propagation of the entire system, instead of the three eigenvalues from (3.3) and (3.2). In general, the results from using the shallow water eigenvalues are not as accurate, often underestimating the eigenvalues of (3.3) and (3.2) and ignoring the different speed for the sediment transport.

To overcome the diffusion of the computed solution of the bottom, we make use of the different speeds of propagation, (3.13)-(3.16), in the evolution of our numerical method, making sure to always use \hat{a}^\pm and \hat{c}^\pm in the central-upwind numerical fluxes when evolving (3.3) and (3.2), respectively. The introduction of \hat{c}^\pm will change how we calculate the time step for our scheme Δt , which is based on the local speeds of propagation for the system. We implement the changes to our scheme using two different approaches, referred to as the splitting approach and the non-splitting approach, which are discussed in the following sections.

3.2.1 Splitting Approach

In the splitting approach, we solve the system (3.3) and (3.2) by separating the system into the shallow water system (3.3) and the Exner equation (3.2) and solving each independently. Our

system will be solved by applying a Strang operator splitting method (see e.g. [81]) outlined below. We start by considering the following two subsystems:

$$\begin{cases} \mathbf{U}_t + \widehat{\mathbf{F}}(\mathbf{U})_x &= \mathbf{S}(\mathbf{U}), \\ B_t &= 0, \end{cases} \quad (3.17)$$

$$\begin{cases} \mathbf{U}_t &= \mathbf{0}, \\ B_t + \xi \frac{\partial q_{b1}}{\partial x} &= 0, \end{cases} \quad (3.18)$$

where $\widehat{\mathbf{F}}(\mathbf{U}) = \left(q + \xi q_b, \frac{q^2}{w-B} + \frac{q}{2}(w^2 - 2wB) \right)^\top$. The subsystem in (3.17) represents the shallow water equations with the bottom held fixed in time, and it will be referred to as the hydrodynamic subsystem. The subsystem in (3.18) represents the Exner equation with the shallow water equations fixed in time, and it will be referred to as the morphodynamic subsystem.

Assuming the solution is available at time t , let \mathcal{S}_w represent the exact solution operators for the 1-D shallow water equations with the bottom fixed in time, (3.17), and let \mathcal{S}_s represent the sediment transport with water fixed in time (3.18) respectively. We evolve the system to the next time level, $t + \Delta t_{spl}$, where Δt_{spl} is called the splitting time step, using an operator splitting algorithm of the first order given by

$$\begin{pmatrix} \mathbf{U}(x, t + \Delta t_{spl}) \\ B(x, t + \Delta t_{spl}) \end{pmatrix} \approx \mathcal{S}_s(\Delta t_{spl}) \mathcal{S}_w(\Delta t_{spl}) \begin{pmatrix} \mathbf{U}(x, t) \\ B(x, t) \end{pmatrix}, \quad (3.19)$$

or of the second order given by

$$\begin{pmatrix} \mathbf{U}(x, t + \Delta t_{spl}) \\ B(x, t + \Delta t_{spl}) \end{pmatrix} \approx \mathcal{S}_w(\Delta t_{spl}/2) \mathcal{S}_s(\Delta t_{spl}) \mathcal{S}_w(\Delta t_{spl}/2) \begin{pmatrix} \mathbf{U}(x, t) \\ B(x, t) \end{pmatrix}. \quad (3.20)$$

We note, in practice, numerical approximations for the exact solution operators \mathcal{S}_w and \mathcal{S}_s are used.

In all our splitting methods, we use second order Strang splitting. When solving using (3.20), we have two sets of intermediate values that will be used. The first set of intermediate values we denote by

$$\mathbf{U}^*(x, t) \approx \mathcal{S}_w(\Delta t_{spl}/2) \begin{pmatrix} \mathbf{U}(x, t) \\ B(x, t) \end{pmatrix}, \quad (3.21)$$

which represents the computed values for \mathbf{U} and B after the hydrodynamic subsystem has been

evolved to $\Delta t_{spl}/2$. The second set of intermediate values, which represents the computed values for \mathbf{U} and B after the morphodynamic subsystem has been evolved to Δt_{spl} , is denoted by

$$\mathbf{U}^{**}(x, t) \approx \mathcal{S}_s(\Delta t_{spl}) \mathcal{S}_w(\Delta t_{spl}/2) \begin{pmatrix} \mathbf{U}(x, t) \\ B(x, t) \end{pmatrix}. \quad (3.22)$$

Because the systems from (3.17) and (3.18) are solved independently, this method only works if the water flow has a negligible effect on the sediment flow and vice versa. A great deal of research has been performed on the splitting approach for solving this system, see e.g. [18, 19, 21, 22, 36, 37, 73]. In most physical cases, as stated in Cunge et al. [19], the water flow is considerably faster than the movement of the sediment. For example, over time a river channel may change its flow location, with the sediment shifting over many years, while the water may flow through a channel on an order of days. Therefore, the assumption that the water and sediment waves have negligible impact on each other fits with real world physical phenomena. A benefit of using a splitting approach is that since the systems are solved separately, we may solve each subsystem, (3.17) and (3.18), using existing methods tailored to each system. This may prove useful when the sediment flux q_b is complicated and does not have an analytic formulation and, therefore, cannot easily be used in the Jacobian. In this case, empirical data can be used to evolve (3.2) in a black box manner.

3.2.2 Non-Splitting Approach

In the non-splitting approach, the system of three equations from (3.3) and (3.2) is solved simultaneously. Assuming the solution is available at time t , let \mathcal{S} represent the exact solution operators for the system of (3.3) and (3.2). Then, we can evolve the system to the next time level $(t + \Delta t)$ by

$$\mathbf{W}(x, t + \Delta t) = \begin{pmatrix} \mathbf{U}(x, t + \Delta t) \\ B(x, t + \Delta t) \end{pmatrix} \approx \mathcal{S}(\Delta t) \begin{pmatrix} \mathbf{U}(x, t) \\ B(x, t) \end{pmatrix}, \quad (3.23)$$

where $\mathbf{W} = (w, q, B)^\top$, noting that \hat{a}^\pm are used in the central-upwind numerical fluxes for the computed solution of $\mathbf{U}(x, t)$, and \hat{c}^\pm are used in the central-upwind numerical flux for the computed solution for $B(x, t)$. In practice, numerical approximations for the exact solution operator \mathcal{S} are used.

In comparison to the splitting approach, less research has been carried out on the non-splitting case as a full solution can be too complex to solve (see the discussion in Cunge et

al. [19]). In part, this is due to the difficult nature of obtaining the eigenvalues of the complete system which are used for the local speeds of propagation and based on how the sediment transport flux in the 1-D Exner equation is defined. If the sediment transport flux is differentiable and can be calculated and incorporated into the Jacobian of the system, as with Grass's formula, the non-splitting approach may have large benefits in solving the case when the water wave speed and the sediment wave speed are similar in magnitude. While rare, this case, as stated in Perdreau and Cunge [73], cannot be handled properly by the splitting approach, as the splitting approach assumes negligible interaction between the water and sediment. The non-splitting approach, however, can handle both the cases where the magnitude of the water wave speed and the sediment wave speed are similar or dissimilar.

3.3 Spatial Discretization

In this section, we discuss the spatial discretization used when solving the numerical schemes, which we will refer to as being solved on a non-staggered discretized grid or on a staggered discretized grid. In both the non-staggered and staggered cases, we divide the computational domain into a uniform grid composed of cells, denoted by $C_j := [x_{j-\frac{1}{2}}, x_{j+\frac{1}{2}}]$, of size $|C_j| = x_{j+\frac{1}{2}} - x_{j-\frac{1}{2}} = \Delta x$ for all $j = 1 \dots N$, where N is the number of cells in the domain. The difference between the non-staggered and staggered discretized grids is where in each cell we define our cell averages $\bar{\mathbf{U}}(t)$ and $\bar{B}(x, t)$.

3.3.1 Non-Staggered Discretized Grid

For the non-staggered discretized grid, if an approximate solution is available at a time level t^n for $\mathbf{U}(x, t)$ and $B(x, t)$, we define the cell averages at the center of each cell $x = x_j$, $\forall j$, and they are computed by

$$\bar{\mathbf{U}}_j^n(t) \approx \frac{1}{\Delta x} \int_{C_j} \mathbf{U}(x, t^n) dx, \quad (3.24)$$

$$\bar{B}_j^n(t) \approx \frac{1}{\Delta x} \int_{C_j} B(x, t^n) dx. \quad (3.25)$$

In this implementation of the spatial discretization, the equations for \mathbf{U} and B are solved on the same spatial grid. An example of this spatial discretization can be seen in Figure 3.1.

3.3.2 Staggered Discretized Grid

On the staggered discretized grid, if an approximate solution is available at a time level t^n for $\mathbf{U}(x, t)$ and $B(x, t)$, we define the cell averages as follows. For $\mathbf{U}(x, t)$, we define the cell average,

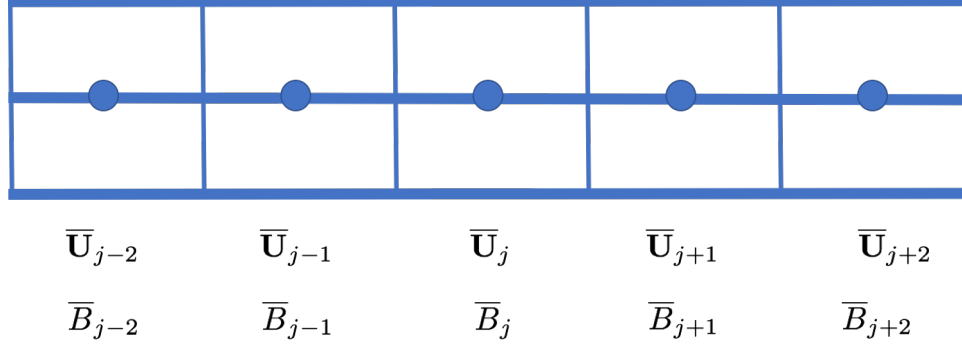


Figure 3.1: Non-staggered discretized grid for $\bar{\mathbf{U}}$ and \bar{B} .

$\bar{\mathbf{U}}_j(t)$, at the center of each cell $x = x_j$, $\forall j$, and, for $B(x, t)$ we define the cell average, $\bar{B}_j(t)$, at the interface of each cell $x = x_{j+\frac{1}{2}}$, $\forall j$. Then, the cell averages are computed by

$$\bar{\mathbf{U}}_j^n(t) \approx \frac{1}{\Delta x} \int_{C_j} \mathbf{U}(x, t^n) dx, \quad (3.26)$$

$$\bar{B}_{j+\frac{1}{2}}^n(t) : \approx \frac{1}{\Delta x} \int_{C_{j+\frac{1}{2}}} B(x, t^n) dx. \quad (3.27)$$

In this implementation of the spatial discretization, the equations for \mathbf{U} and B are solved on different spatial grids. An example of this can be seen in Figure 3.2.

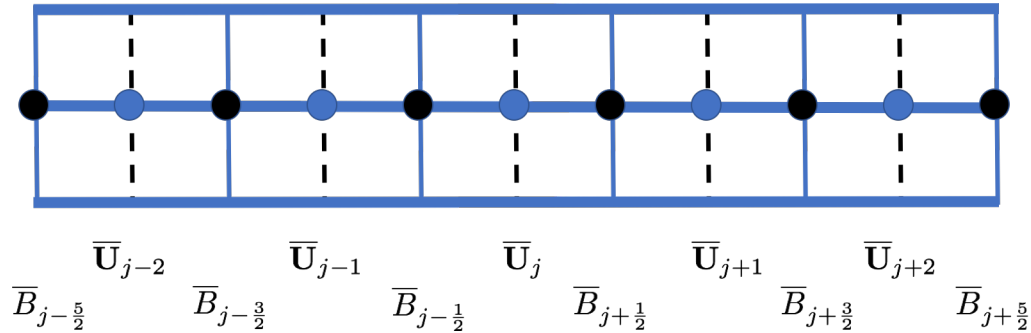


Figure 3.2: Staggered discretized grid consisting of $\bar{\mathbf{U}}$ (blue) centered at the cell center and of \bar{B} (black dashed) centered at the cell interface.

In the following sections, we describe the formulation of four different well-balanced second order central-upwind schemes made from the combination of the splitting approach, non-splitting approach, non-staggered discretized grid, and staggered discretized grid.

3.4 Numerical Scheme for the Splitting Approach with the Bottom Evolved on a Non-Staggered Discretized Grid (S-NSG)

The Formulation S-NSG is based on the splitting approach with the bottom evolved on a non-staggered discretized grid. For this scheme, we use the spatial discretization from Section 3.3.1 where all the functions make use of a non-staggered discretized grid.

3.4.1 Hydrodynamic Subsystem

For the hydrodynamic subsystem (3.17) of the Strang splitting (3.20), we fix the bottom function in time and solve the shallow water equations in terms of equilibrium variables. Starting with the cell averages obtained in (3.24) and (3.25) applying a second order semi-discrete central-upwind formulation to $\bar{\mathbf{U}}_j$, we have the cell averages are evolved in time by

$$\frac{d}{dt} \bar{\mathbf{U}}_j(t) = -\frac{\hat{\mathbf{H}}_{j+\frac{1}{2}}(t) - \hat{\mathbf{H}}_{j-\frac{1}{2}}(t)}{\Delta x} + \bar{\mathbf{S}}_j(t), \quad (3.28)$$

where $\hat{\mathbf{H}}_{j\pm\frac{1}{2}}$ are the central-upwind numerical fluxes and $\bar{\mathbf{S}}_j(t)$ is given by

$$\bar{\mathbf{S}}_j(t) \approx \frac{1}{\Delta x} \int_{C_j} \mathbf{S}(\mathbf{U}) dx, \quad (3.29)$$

and $\bar{\mathbf{S}}_j(t)$ represents the cell averages of the geometric source term. For simplicity in the rest of this section, we drop the notation t for time dependence where appropriate.

The construction of the scheme will be complete once the numerical fluxes $\hat{\mathbf{H}}_{j\pm\frac{1}{2}}$ in (3.30) and the source term $\bar{\mathbf{S}}_j$ in (3.29) are computed such that the resulting method is well-balanced.

Numerical Fluxes. In (3.28), we use the central-upwind fluxes from [50], slightly modifying the local speeds of propagation to \hat{a}^\pm using (3.13) and (3.14):

$$\hat{\mathbf{H}}_{j+\frac{1}{2}}(t) = \frac{\hat{a}_{j+\frac{1}{2}}^+ \hat{\mathbf{F}}(\mathbf{U}_{j+\frac{1}{2}}^-, B_{j+\frac{1}{2}}^-) - \hat{a}_{j+\frac{1}{2}}^- \hat{\mathbf{F}}(\mathbf{U}_{j+\frac{1}{2}}^+, B_{j+\frac{1}{2}}^+)}{\hat{a}_{j+\frac{1}{2}}^+ - \hat{a}_{j+\frac{1}{2}}^-} + \frac{\hat{a}_{j+\frac{1}{2}}^+ \hat{a}_{j+\frac{1}{2}}^-}{\hat{a}_{j+\frac{1}{2}}^+ - \hat{a}_{j+\frac{1}{2}}^-} \left[\mathbf{U}_{j+\frac{1}{2}}^+ - \mathbf{U}_{j+\frac{1}{2}}^- \right]. \quad (3.30)$$

Reconstruction. In equation (3.30), $\mathbf{U}_{j+\frac{1}{2}}^\pm$ are the left and right point values of the piecewise linear reconstructions

$$\tilde{\mathbf{U}}(x) = \sum_j [\bar{\mathbf{U}}_j + (\mathbf{U}_x)_j(x - x_j)] \cdot \chi_{C_j}(x), \quad (3.31)$$

obtained at the midpoint cell interfaces $x = x_{j \pm \frac{1}{2}}$ by

$$\mathbf{U}_{j+\frac{1}{2}}^+ = \bar{\mathbf{U}}_{j+1} - \frac{\Delta x}{2} (\mathbf{U}_x)_{j+1}, \quad \mathbf{U}_{j+\frac{1}{2}}^- = \bar{\mathbf{U}}_j + \frac{\Delta x}{2} (\mathbf{U}_x)_j. \quad (3.32)$$

In (3.31), recall $\chi_{C_j}(x)$ is the characteristic function of the interval C_j , and $(\mathbf{U}_x)_j$ represents the numerical derivatives, which are computed using a nonlinear limiter to reduce oscillations. In our numerical experiments, we use the generalized minmod limiter given in (1.93) and (1.94).

For Formulation S-SNG, after obtaining $\tilde{\mathbf{U}}(x)$ for the reconstruction of \mathbf{U} using (3.31) and (3.32), we approximate the bottom function B using a generally discontinuous piecewise linear reconstruction.

Piecewise Linear Reconstruction of B . In order to capture discontinuities in the bottom in a robust and accurate manner, following [5], we approximate the bottom function B with a generally discontinuous piecewise linear reconstruction

$$\tilde{B}(x) = \sum_j \left[\bar{B}_{j+\frac{1}{2}} + (B_x)_{j+\frac{1}{2}} (x - x_{j+\frac{1}{2}}) \right] \cdot \chi_{C_j}(x), \quad (3.33)$$

with point values obtained on the cell interfaces $x = x_{j \pm \frac{1}{2}}$ by

$$B_{j+\frac{1}{2}}^+ = \bar{B}_{j+1} - \frac{\Delta x}{2} (B_x)_{j+1}, \quad B_{j+\frac{1}{2}}^- = \bar{B}_j + \frac{\Delta x}{2} (B_x)_j. \quad (3.34)$$

The numerical derivatives in (3.33) and (3.34) are calculated using the same midmod limiter in (1.93) and (1.94). We note, in this stage of the splitting, the reconstruction is used to obtain the left and right point values for B at the interfaces for use in (3.30), but the bottom function B is fixed in time during hydrodynamic subsystem evolution.

Well-Balanced Quadrature for the Geometric Source Terms. In order to ensure the method is well-balanced, a special quadrature should be used to discretize the second component $\bar{S}_j^{(2)}$ of the source term in (3.29) such that it balances with the numerical fluxes. The fluxes at the discrete level are given by

$$\frac{\hat{H}_{j+\frac{1}{2}}^{(2)} - \hat{H}_{j-\frac{1}{2}}^{(2)}}{\Delta x} = \frac{g\bar{w}_j}{\Delta x} \left(\frac{\hat{a}_{j+\frac{1}{2}}^+ B_{j+\frac{1}{2}}^- - \hat{a}_{j+\frac{1}{2}}^- B_{j+\frac{1}{2}}^+}{\hat{a}_{j+\frac{1}{2}}^+ - \hat{a}_{j+\frac{1}{2}}^-} - \frac{\hat{a}_{j-\frac{1}{2}}^+ B_{j-\frac{1}{2}}^- - \hat{a}_{j-\frac{1}{2}}^- B_{j-\frac{1}{2}}^+}{\hat{a}_{j-\frac{1}{2}}^+ - \hat{a}_{j-\frac{1}{2}}^-} \right). \quad (3.35)$$

Therefore, the fluxes and source term will balance if the second component of the source term

is discretized as follows:

$$\bar{S}_j^{(2)} \approx -\frac{g\bar{w}_j}{\Delta x} \left(\frac{\hat{a}_{j+\frac{1}{2}}^+ B_{j+\frac{1}{2}}^- - \hat{a}_{j+\frac{1}{2}}^- B_{j+\frac{1}{2}}^+}{\hat{a}_{j+\frac{1}{2}}^+ - \hat{a}_{j+\frac{1}{2}}^-} - \frac{\hat{a}_{j-\frac{1}{2}}^+ B_{j-\frac{1}{2}}^- - \hat{a}_{j-\frac{1}{2}}^- B_{j-\frac{1}{2}}^+}{\hat{a}_{j-\frac{1}{2}}^+ - \hat{a}_{j-\frac{1}{2}}^-} \right). \quad (3.36)$$

Local Speeds of Propagation. Within the hydrodynamic subsystem (3.19), we are only concerned with the fast moving water waves of the shallow water equations. Thus, the local speeds of propagation are given by the largest and smallest of these eigenvalues, corresponding to $\lambda^{(1)}$ and $\lambda^{(3)}$, such that, in this spatial discretization,

$$\begin{aligned} \hat{a}_{j+\frac{1}{2}}^+ &= \max \left\{ \lambda_{j+\frac{1}{2}}^{(1)+}, \lambda_{j+\frac{1}{2}}^{(1)-}, \lambda_{j+\frac{1}{2}}^{(3)+}, \lambda_{j+\frac{1}{2}}^{(3)-}, 0 \right\}, \\ \hat{a}_{j+\frac{1}{2}}^- &= \min \left\{ \lambda_{j+\frac{1}{2}}^{(1)+}, \lambda_{j+\frac{1}{2}}^{(1)-}, \lambda_{j+\frac{1}{2}}^{(3)+}, \lambda_{j+\frac{1}{2}}^{(3)-}, 0 \right\}. \end{aligned} \quad (3.37)$$

Intermediate Computed Solution for \mathbf{U} . After the first stage of our operator splitting in (3.18), we evolved (3.28) to time $t + \Delta t_{spl}/2$ where we obtained the intermediate solution \mathbf{U}_j^* defined as in (3.21). We use this as the initial condition for the second stage of our operator splitting.

3.4.2 Morphodynamic Subsystem

In the second stage of the operator splitting, we evolve the morphodynamic subsystem (3.18), which fixes \mathbf{U}^* in time, and evolve the bottom on a non-staggered discretized grid. The cell averages $\bar{\mathbf{U}}_j^*$ and \bar{B}_j will be defined as in (3.24) and (3.25), respectively. Applying a second order semi-discrete central-upwind formulation to the bottom function B , we have the cell averages will be evolved in time by

$$\frac{d}{dt} \bar{B}_j(t) = -\frac{\mathcal{H}_{j+\frac{1}{2}}(t) - \mathcal{H}_{j-\frac{1}{2}}(t)}{\Delta x}, \quad (3.38)$$

where $\mathcal{H}_{j\pm\frac{1}{2}}$ in (3.38) are the central-upwind numerical fluxes for the bottom given in (3.39).

Numerical Fluxes. In (3.38), we use the central-upwind fluxes from [50]. However, since we are only evolving the bottom, we modify the local speeds of propagation to \hat{c}^\pm using (3.15) and (3.16), which only takes into account the eigenvalue associated with the Exner equation:

$$\mathcal{H}_{j+\frac{1}{2}}(t) = \frac{\hat{c}_{j+\frac{1}{2}}^+ q_b(\mathbf{U}_{j+\frac{1}{2}}^{*-}) - \hat{c}_{j+\frac{1}{2}}^- q_b(\mathbf{U}_{j+\frac{1}{2}}^{*+})}{\hat{c}_{j+\frac{1}{2}}^+ - \hat{c}_{j+\frac{1}{2}}^-} + \frac{\hat{c}_{j+\frac{1}{2}}^+ \hat{c}_{j+\frac{1}{2}}^-}{\hat{c}_{j+\frac{1}{2}}^+ - \hat{c}_{j+\frac{1}{2}}^-} \left[B_{j+\frac{1}{2}}^+ - B_{j+\frac{1}{2}}^- \right]. \quad (3.39)$$

Reconstruction. In equation (3.39), $B_{j+\frac{1}{2}}^{\pm}$ and $\mathbf{U}_{j+\frac{1}{2}}^{*\pm}$ are the left and right point values of the piecewise linear reconstructions

$$\tilde{B}(x) = \sum_j [\bar{B}_j + (B_x)_j(x - x_j)] \cdot \chi_{C_j}(x), \quad (3.40)$$

$$\tilde{\mathbf{U}}^*(x) = \sum_j [\bar{\mathbf{U}}_j^* + (\mathbf{U}_x)_j(x - x_j)] \cdot \chi_{C_j}(x), \quad (3.41)$$

obtained at the midpoint cell interfaces $x = x_{j\pm\frac{1}{2}}$ by

$$B_{j+\frac{1}{2}}^+ = \bar{B}_{j+1} - \frac{\Delta x}{2} (B_x)_{j+1}, \quad B_{j+\frac{1}{2}}^- = \bar{B}_j + \frac{\Delta x}{2} (B_x)_j, \quad (3.42)$$

$$\mathbf{U}_{j+\frac{1}{2}}^{*+} = \bar{\mathbf{U}}_{j+1}^* - \frac{\Delta x}{2} (\mathbf{U}_x^*)_{j+1}, \quad \mathbf{U}_{j+\frac{1}{2}}^{*-} = \bar{\mathbf{U}}_j^* + \frac{\Delta x}{2} (\mathbf{U}_x^*)_j, \quad (3.43)$$

where the numerical derivatives $(B_x)_j$ and $(\mathbf{U}_x)_j$ are computed using a nonlinear limiter to reduce oscillations as was done in (1.93) and (1.94).

Local Speeds of Propagation. Within the morphodynamic subsystem (3.20), we are only concerned with the slow moving sediment waves corresponding to the Exner equation. Thus, the local speeds of propagation are given by the largest and smallest of these eigenvalues corresponding to $\lambda^{(2)}$. Therefore,

$$\begin{aligned} \widehat{c}_{j+\frac{1}{2}}^+ &= \max \left\{ \lambda_{j+\frac{1}{2}}^{(2)+}, \lambda_{j+\frac{1}{2}}^{(2)-}, 0 \right\}, \\ \widehat{c}_{j+\frac{1}{2}}^- &= \min \left\{ \lambda_{j+\frac{1}{2}}^{(2)+}, \lambda_{j+\frac{1}{2}}^{(2)-}, 0 \right\}. \end{aligned} \quad (3.44)$$

Second Intermediate Computed Solution for \mathbf{U} . After the second stage of our operator splitting we evolved (3.38) to time $t + \Delta t_{spl}$ where we obtained the intermediate solution \mathbf{U}_j^{**} as defined in (3.22). These values are used as the initial condition for the hydrodynamic subsystem, and we evolve (3.38) from $t + \Delta t_{spl}/2$ to $t + \Delta t_{spl}$.

3.4.3 Time Evolution of S-NSG

When choosing the splitting time step Δt_{spl} , the choice is not unique, and instead depends on which of our local speeds of propagation $\left(\widehat{c}_{j+\frac{1}{2}}^{\pm} \text{ or } \widehat{a}_{j+\frac{1}{2}}^{\pm} \right)$ we use to define it. If we consider the splitting time step on the morphodynamic time step the CFL condition is satisfied using the

sediment waves speed of propagation $\widehat{c}_{j+\frac{1}{2}}^\pm$. Thus,

$$\Delta t_{spl} \leq \frac{1}{2} \min \left\{ \frac{\Delta x}{|\widehat{c}_{j+\frac{1}{2}}^\pm|} \right\}. \quad (3.45)$$

We may also consider the splitting time step on the hydrodynamic time step, where the CFL condition is satisfied using the water waves speed of propagation $\widehat{a}_{j+\frac{1}{2}}^\pm$. Thus,

$$\Delta t_{spl} \leq \frac{1}{2} \min \left\{ \frac{\Delta x}{|\widehat{a}_{j+\frac{1}{2}}^\pm|} \right\}. \quad (3.46)$$

In Section 3.4.3.1 and Section 3.4.3.2, we further discuss when the CFL condition is constrained by (3.45) and (3.46), respectively.

3.4.3.1 Time Evolution of S-NSG When the Splitting Time-Step Is Chosen Using the Morphodynamic Time-Step (S-NSG-M)

In this section we detail how the time evolution is implemented when the splitting time step is chosen using the morphological time step (3.45). While Δt_{spl} is the overall time step, each individual hydrodynamic subsystem or morphodynamic subsystem may require a smaller time step when the system is evolved for our scheme to remain stable. Consider the first hydrodynamic subsystem in our splitting (3.19) which we evolve to $\Delta t_{spl}/2$. This hydrodynamic subsystem is associated with the one sided local speeds of propagation given by $\widehat{a}_{j+\frac{1}{2}}^\pm$ in (3.37). The values of $\widehat{a}_{j+\frac{1}{2}}^\pm$ are larger than $\widehat{c}_{j+\frac{1}{2}}^\pm$, and thus the hydrodynamic subsystem will require a smaller time step to remain stable. The constraint on this time step is given by

$$\Delta t_w \leq \min \left\{ \frac{\Delta x}{\max_j 2|\widehat{a}_{j\pm\frac{1}{2}}^\pm|}, \frac{\Delta t_{spl}}{2} \right\}, \quad (3.47)$$

where Δt_w is the time step used when evolving the hydrodynamic subsystem. Since Δt_w may be smaller than $\Delta t_{spl}/2$, the end time in the first step of our Strang splitting, the method may require multiple hydrodynamic subsystem evolutions of Δt_w to equal $\Delta t_{spl}/2$.

For the second stage of the splitting, we solve the morphodynamic subsystem until Δt_{spl} . We make sure to satisfy

$$\Delta t_s \leq \min \left\{ \frac{\Delta x}{\max_j 2|\widehat{c}_{j\pm\frac{1}{2}}^\pm|}, \Delta t_{spl} \right\}, \quad (3.48)$$

where Δt_s is the time step used when evolving the morphodynamic subsystem. We note that in

most cases $\Delta t_s = \Delta t_{spl}$, but if, during the evolution, $\Delta t_s < \Delta t_{spl}$, multiple Δt_s time evolutions may be needed.

For the final stage of our splitting, we will evolve the hydrodynamic subsystem from $t + \Delta t_{spl}/2$ to $t + \Delta t_{spl}$ making sure to satisfy (3.47).

3.4.3.2 Time Evolution of S-NSG When the Splitting Time-Step Is Chosen Using the Hydrodynamic Time-Step (S-NSG-H)

In this section we detail how the time evolution is implemented when the the splitting time step is chosen using the hydrodynamic time step (3.46). Then, Δt_{spl} is constrained by the following condition:

$$\Delta t_{spl} \leq \frac{1}{2} \min \left\{ \frac{\Delta x}{\max_j |\hat{a}_{j\pm\frac{1}{2}}^\pm|} \right\} \leq \frac{1}{2} \min \left\{ \frac{\Delta x}{\max_j |\hat{c}_{j\pm\frac{1}{2}}^\pm|} \right\}. \quad (3.49)$$

Since Δt_{spl} is based on the smaller time step associated with the fast moving local speeds of propagation, when evolving the hydrodynamic subsystem to $\Delta t_{spl}/2$, we will always take one step since

$$\Delta t_w \leq \frac{\Delta t_{spl}}{2} < \frac{1}{2} \min \left\{ \frac{\Delta x}{\max_j |\hat{a}_{j\pm\frac{1}{2}}^\pm|} \right\}. \quad (3.50)$$

For the evolution of the morphodynamic subsystem which is evolved to Δt_{spl} , since Δt_s is naturally greater than Δt_{spl} , only take one step in Δt_s . Thus, the CFL is constrained as follows:

$$\Delta t_s < \Delta t_{spl} \leq \frac{1}{2} \min \left\{ \frac{\Delta x}{\max_j |\hat{c}_{j\pm\frac{1}{2}}^\pm|} \right\}. \quad (3.51)$$

For the final stage of our splitting, we will evolve the hydrodynamic subsystem from $t + \Delta t_{spl}/2$ to $t + \Delta t_{spl}$ making sure to satisfy (3.49).

3.5 Numerical Scheme for the Splitting Approach with the Bottom Evolved on a Staggered Discretized Grid (S-SG)

The Formulation S-SG is based on the splitting approach where the bottom evolved on a staggered discretized grid. For this scheme, we use the spatial discretization in Section 3.3.2, where $\bar{\mathbf{U}}$ uses a non-staggered discretized grid and \bar{B} uses a staggered discretized grid.

3.5.1 Hydrodynamic Subsystem

For the hydrodynamic subsystem (3.17) of the Strang splitting (3.20), we fix the bottom function in time and solve the shallow water equations in terms of equilibrium variables. Starting with the cell averages obtained in (3.26) and applying a second order semi-discrete central-upwind formulation to $\bar{\mathbf{U}}_j$, we have the cell averages are evolved in time by

$$\frac{d}{dt} \bar{\mathbf{U}}_j(t) = -\frac{\hat{\mathbf{H}}_{j+\frac{1}{2}}(t) - \hat{\mathbf{H}}_{j-\frac{1}{2}}(t)}{\Delta x} + \bar{\mathbf{S}}_j(t), \quad (3.52)$$

where $\hat{\mathbf{H}}_{j\pm\frac{1}{2}}$ are the central-upwind numerical fluxes and $\bar{\mathbf{S}}_j(t)$ is given by

$$\bar{\mathbf{S}}_j(t) \approx \frac{1}{\Delta x} \int_{C_j} \mathbf{S}(\mathbf{U}) dx, \quad (3.53)$$

and $\bar{\mathbf{S}}_j(t)$ represents the cell averages of the geometric source term. For the rest of this section we will drop the notation t for time dependence for simplicity where it is appropriate.

The construction of the scheme will be complete once the numerical fluxes $\hat{\mathbf{H}}_{j\pm\frac{1}{2}}$ in (3.54) and the source term $\bar{\mathbf{S}}_j$ in (3.53) are computed such that the resulting method is well-balanced.

Numerical Fluxes. In (3.28), we use the central-upwind fluxes from [50], slightly modifying the local speeds of propagation to \hat{a}^\pm using (3.13) and (3.14) so that

$$\hat{\mathbf{H}}_{j+\frac{1}{2}}(t) = \frac{\hat{a}_{j+\frac{1}{2}}^+ \hat{\mathbf{F}}(\mathbf{U}_{j+\frac{1}{2}}^-, B_{j+\frac{1}{2}}) - \hat{a}_{j+\frac{1}{2}}^- \hat{\mathbf{F}}(\mathbf{U}_{j+\frac{1}{2}}^+, B_{j+\frac{1}{2}})}{\hat{a}_{j+\frac{1}{2}}^+ - \hat{a}_{j+\frac{1}{2}}^-} + \frac{\hat{a}_{j+\frac{1}{2}}^+ \hat{a}_{j+\frac{1}{2}}^-}{\hat{a}_{j+\frac{1}{2}}^+ - \hat{a}_{j+\frac{1}{2}}^-} \left[\mathbf{U}_{j+\frac{1}{2}}^+ - \mathbf{U}_{j+\frac{1}{2}}^- \right]. \quad (3.54)$$

Note that, in (3.54), since the bottom is solved on a staggered discretized grid, there is only one value for B at each interface $x = x_{j+\frac{1}{2}}$.

Reconstruction. In equation (3.54), $\mathbf{U}_{j+\frac{1}{2}}^\pm$ are the left and right point values of the piecewise linear reconstructions

$$\tilde{\mathbf{U}}(x) = \sum_j [\bar{\mathbf{U}}_j + (\mathbf{U}_x)_j(x - x_j)] \cdot \chi_{C_j}(x), \quad (3.55)$$

obtained at the midpoint cell interfaces $x = x_{j\pm\frac{1}{2}}$ by

$$\mathbf{U}_{j+\frac{1}{2}}^+ = \bar{\mathbf{U}}_{j+1} - \frac{\Delta x}{2} (\mathbf{U}_x)_{j+1}, \quad \mathbf{U}_{j+\frac{1}{2}}^- = \bar{\mathbf{U}}_j + \frac{\Delta x}{2} (\mathbf{U}_x)_j. \quad (3.56)$$

In (3.55), $\chi_{C_j}(x)$ is the characteristic function of the interval C_j , and $(\mathbf{U}_x)_j$ represents the numerical derivatives, which are computed using a nonlinear limiter to reduce oscillations. In our numerical experiments, we use the generalized minmod limiter (1.93) and (1.94).

For Formulation S-SG after obtaining $\tilde{\mathbf{U}}(x)$ for the reconstruction of \mathbf{U} using (3.31) and (3.32), we approximate B using a continuous piecewise linear approximation.

Piecewise Linear Approximation of B . In contrast to our previous approaches for approximating the bottom, we replace the bottom function B with a continuous piecewise linear approximation following [50]. The continuous piecewise linear approximation is given by

$$\tilde{B}(x) = B_{j-\frac{1}{2}} + \left(B_{j+\frac{1}{2}} - B_{j-\frac{1}{2}} \right) \frac{x - x_{j-\frac{1}{2}}}{\Delta x}, \quad x_{j-\frac{1}{2}} \leq x \leq x_{j+\frac{1}{2}} \quad (3.57)$$

where

$$B_{j+\frac{1}{2}} := \frac{1}{2} \left(B(x_{j+\frac{1}{2}} + 0) + B(x_{j+\frac{1}{2}} - 0) \right). \quad (3.58)$$

$B(x_{j+\frac{1}{2}} + 0)$ and $B(x_{j+\frac{1}{2}} - 0)$ represent the right and left values of the interface, respectively, if B is discontinuous at the interface. However, if B is continuous at the interface it reduces to $B_{j+\frac{1}{2}} = B(x_{j+\frac{1}{2}})$.

This linear approximation results in the cell average of \tilde{B} over the cell C_j equaling the value at the center of the cell and the average of the midpoint values of \tilde{B} . Thus,

$$\bar{B}_j := \tilde{B}(x_j) = \frac{1}{\Delta x} \int_{C_j} \tilde{B}(x) dx = \frac{1}{2} \left(B_{j+\frac{1}{2}} + B_{j-\frac{1}{2}} \right). \quad (3.59)$$

Well-Balanced Quadrature for the Geometric Source Terms. In order to ensure the scheme is well-balanced, a special quadrature should be used to discretize the second component $\bar{S}_j^{(2)}$ of the source term in (3.53) such that it balances with the numerical fluxes. The fluxes at the discrete level are given by

$$\frac{\hat{H}_{j+\frac{1}{2}}^{(2)} - \hat{H}_{j-\frac{1}{2}}^{(2)}}{\Delta x} = \frac{g\bar{w}_j}{\Delta x} \left(\frac{\hat{a}_{j+\frac{1}{2}}^+ B_{j+\frac{1}{2}} - \hat{a}_{j+\frac{1}{2}}^- B_{j+\frac{1}{2}}}{\hat{a}_{j+\frac{1}{2}}^+ - \hat{a}_{j+\frac{1}{2}}^-} - \frac{\hat{a}_{j-\frac{1}{2}}^+ B_{j-\frac{1}{2}} - \hat{a}_{j-\frac{1}{2}}^- B_{j-\frac{1}{2}}}{\hat{a}_{j-\frac{1}{2}}^+ - \hat{a}_{j-\frac{1}{2}}^-} \right), \quad (3.60)$$

$$= \frac{g\bar{w}_j}{\Delta x} \left(B_{j+\frac{1}{2}} - B_{j-\frac{1}{2}} \right). \quad (3.61)$$

Note, when the bottom is discretized on a staggered discretized grid, there is only a value at the interface $x = x_{j+\frac{1}{2}}$ or $x = x_{j-\frac{1}{2}}$. Thus, the $B_{j\pm\frac{1}{2}}^\pm$ which are normally present in (3.60) are reduced to $B_{j\pm\frac{1}{2}}$. Therefore, the fluxes and source term will balance if the second component

of the source term is discretized as follows:

$$\bar{S}_j^{(2)} \approx -\frac{g\bar{w}_j}{\Delta x} \left(B_{j+\frac{1}{2}} - B_{j-\frac{1}{2}} \right). \quad (3.62)$$

Local Speeds of Propagation. Within the hydrodynamic subsystem (3.19), we are only concerned with the fast moving water waves of the shallow water equations. Thus, the local speeds of propagation are given by the largest and smallest of these eigenvalues, corresponding to $\lambda^{(1)}$ and $\lambda^{(3)}$, such that, in this spatial discretization,

$$\begin{aligned} \hat{a}_{j+\frac{1}{2}}^+ &= \max \left\{ \lambda_{j+\frac{1}{2}}^{(1)+}, \lambda_{j+\frac{1}{2}}^{(1)-}, \lambda_{j+\frac{1}{2}}^{(3)+}, \lambda_{j+\frac{1}{2}}^{(3)-}, 0 \right\}, \\ \hat{a}_{j+\frac{1}{2}}^- &= \min \left\{ \lambda_{j+\frac{1}{2}}^{(1)+}, \lambda_{j+\frac{1}{2}}^{(1)-}, \lambda_{j+\frac{1}{2}}^{(3)+}, \lambda_{j+\frac{1}{2}}^{(3)-}, 0 \right\}. \end{aligned} \quad (3.63)$$

Intermediate Computed Solution for \mathbf{U} . After the first stage of our operator splitting (3.18), where we evolved (3.28) to time $t + \Delta t_{spl}/2$, we obtained the intermediate solution \mathbf{U}_j^* , which is used as the initial condition for the second stage of our operator splitting.

3.5.2 Morphodynamic Subsystem

In the second stage of the operator splitting, we evolve the morphodynamic subsystem which fixes \mathbf{U}_j^* in time and evolves the cell average of the bottom function on a staggered discretized grid. While \mathbf{U}_j^* is defined on a non-staggered discretized grid, we need to obtain the cell average values on the interfaces, $\mathbf{U}_{j+\frac{1}{2}}^*$, for use in the numerical scheme. To this end we project \mathbf{U}_j^* onto a staggered discretized grid using the method shown in Nessyahu and Tadmor [68] to obtain

$$\begin{aligned} \bar{\mathbf{U}}_{j+\frac{1}{2}}^* &= \int_{C_{j+\frac{1}{2}}} \mathbf{U}^*(x) dx, \\ &= \frac{1}{2} \left(\bar{\mathbf{U}}_j^* + \bar{\mathbf{U}}_{j+1}^* \right) + \frac{1}{8} \left\{ \left[\left(\bar{\mathbf{U}}_x^* \right)_j - \left(\bar{\mathbf{U}}_x^* \right)_{j+1} \right] \right\}, \end{aligned} \quad (3.64)$$

where $C_{j+\frac{1}{2}}$ is the cell centered at $x = x_{j+\frac{1}{2}}$ of size Δx , and $\left(\bar{\mathbf{U}}_x^* \right)_{j+1}$ and $\left(\bar{\mathbf{U}}_x^* \right)_j$ are numerical derivatives calculated as in (1.93) and (1.94).

The cell averages of the bottom at the interfaces $\bar{B}_{j+\frac{1}{2}}$ for all j will be defined as in (3.27), and, applying a second order semi-discrete central-upwind formulation to \bar{B} , we have the cell averages will be evolved in time by

$$\frac{d}{dt} \bar{B}_{j+\frac{1}{2}}(t) = -\frac{\mathcal{H}_{j+1}(t) - \mathcal{H}_j(t)}{\Delta x}, \quad (3.65)$$

where \mathcal{H}_{j+1} and \mathcal{H}_j are the central-upwind numerical fluxes for the bottom function given in (3.66).

Numerical Fluxes In (3.65), we use the central-upwind fluxes from [50]. However, since we are only evolving the bottom, we modify the local speeds of propagation to \widehat{c}^\pm using (3.15) and (3.16), which only takes into account the eigenvalue associated with the Exner equation. This results in

$$\mathcal{H}_{j+1}(t) = \frac{\widehat{c}_{j+1}^+ q_b(\mathbf{U}_{j+1}^{*-}) - \widehat{c}_{j+1}^- q_b(\mathbf{U}_{j+1}^{*+})}{\widehat{c}_{j+\frac{1}{2}}^+ - \widehat{c}_{j+1}^-} + \frac{\widehat{c}_{j+1}^+ \widehat{c}_{j+1}^-}{\widehat{c}_{j+1}^+ - \widehat{c}_{j+1}^-} [B_{j+1}^+ - B_{j+1}^-]. \quad (3.66)$$

Reconstruction. In (3.66), $B_{j+\frac{1}{2}}^\pm$ and $\mathbf{U}^{*\pm}$ are the left and right point values of the piecewise linear reconstructions

$$\widetilde{B}(x) = \sum_{j+\frac{1}{2}} \left[\overline{B}_{j+\frac{1}{2}} + (B_x)_{j+\frac{1}{2}}(x - x_{j+\frac{1}{2}}) \right] \cdot \chi_{C_{j+\frac{1}{2}}}(x), \quad (3.67)$$

$$\widetilde{\mathbf{U}}^*(x) = \sum_j \left[\overline{\mathbf{U}}_{j+\frac{1}{2}}^* + (\mathbf{U}_x)_{j+\frac{1}{2}}(x - x_{j+\frac{1}{2}}) \right] \cdot \chi_{C_{j+\frac{1}{2}}}(x), \quad (3.68)$$

obtained at cell interfaces $x = x_j$ and $x = x_{j+1}$ by

$$B_{j+1}^+ = \overline{B}_{j+\frac{3}{2}} - \frac{\Delta x}{2} (B_x)_{j+\frac{3}{2}}, \quad B_{j+1}^- = \overline{B}_{j+\frac{1}{2}} + \frac{\Delta x}{2} (B_x)_{j+\frac{1}{2}}, \quad (3.69)$$

$$\mathbf{U}_{j+1}^{*+} = \overline{\mathbf{U}}_{j+\frac{3}{2}}^* - \frac{\Delta x}{2} (\mathbf{U}_x^*)_{j+\frac{3}{2}}, \quad \mathbf{U}_{j+1}^{*-} = \overline{\mathbf{U}}_{j+\frac{1}{2}}^* + \frac{\Delta x}{2} (\mathbf{U}_x^*)_{j+\frac{1}{2}}, \quad (3.70)$$

where the numerical derivatives $(B_x)_{j+\frac{1}{2}}$ and $(\mathbf{U}_x)_{j+\frac{1}{2}}$ are computed using a nonlinear limiter to reduce oscillations as done in (1.93) and (1.94).

Local Speeds of Propagation. Within the morphodynamic subsystem (3.20), we use only the eigenvalues associated with the slow moving sediment waves to determine the local speeds of propagation \widehat{c}_{j+1}^\pm on the staggered discretized grid by

$$\begin{aligned} c_{j+1}^+ &= \max \left\{ \lambda_{j+1}^{(2)+}, \lambda_{j+1, k+\frac{1}{2}}^{(2)-}, 0 \right\}, \\ c_{j+1}^- &= \min \left\{ \lambda_{j+1}^{(2)+}, \lambda_{j+1, k+\frac{1}{2}}^{(2)-}, 0 \right\}. \end{aligned} \quad (3.71)$$

Second Intermediate Computed Solution for \mathbf{U} . After the second stage of the operator splitting, we evolved (3.65) to time $t + \Delta t_{spl}$ where we obtained the intermediate solution $\mathbf{U}^{**}(x)$

as defined in (3.22). $\mathbf{U}^{**}(x)$ is used as the initial condition for the hydrodynamic system as we evolve (3.52) from $t + \Delta t_{spl}$ to $t + \Delta t_{spl}$.

3.5.3 Time Evolution of S-SG

When choosing the splitting time step Δt_{spl} , the choice is not unique, and it depends on which of our local speeds of propagation $\left(\hat{c}_{j+\frac{1}{2}}^{\pm} \text{ or } \hat{a}_{j+\frac{1}{2}}^{\pm}\right)$ we use to define it. If we consider the splitting time step on the morphodynamic time step the CFL condition is satisfied using the sediment waves speed of propagation $\hat{c}_{j+\frac{1}{2}}^{\pm}$. Thus,

$$\Delta t_{spl} \leq \frac{1}{2} \min \left\{ \frac{\Delta x}{|\hat{c}_{j+\frac{1}{2}}^{\pm}|} \right\}. \quad (3.72)$$

We note the splitting time step is calculated using the eigenvalues associated with the non-staggered discretized grid with the interfaces at $x = x_{j+\frac{1}{2}}$.

We also consider the splitting time step on the hydrodynamic time step, where the CFL condition is satisfied using the water waves speed of propagation $\hat{a}_{j+\frac{1}{2}}^{\pm}$. Thus,

$$\Delta t_{spl} \leq \frac{1}{2} \min \left\{ \frac{\Delta x}{|\hat{a}_{j+\frac{1}{2}}^{\pm}|} \right\}. \quad (3.73)$$

In Section 3.5.3.1 and Section 3.5.3.2, we further discuss when the CFL condition is constrained by (3.72) and (3.73), respectively.

3.5.3.1 Time Evolution of S-SG When the Splitting Time-Step Is Chosen Using the Morphodynamic Time-Step (S-SG-M)

In this section we detail how the time evolution is implemented when the splitting time step is chosen using the morphological time step as in (3.72). While Δt_{spl} is the overall time step, each individual hydrodynamic or morphodynamic subsystem, may require a smaller time step when the system is evolved for our scheme to remain stable. Consider the first hydrodynamic subsystem in our splitting from (3.19) which we evolve to $\Delta t_{spl}/2$. This hydrodynamic subsystem is associated with the one sided local speeds of propagation given by $\hat{a}_{j+\frac{1}{2}}^{\pm}$ in (3.63). The values of $\hat{a}_{j+\frac{1}{2}}^{\pm}$ are larger than those of $\hat{c}_{j+\frac{1}{2}}^{\pm}$, and thus the hydrodynamic subsystem will require

a smaller time step to remain stable. The constraint on this time step is given by

$$\Delta t_w \leq \frac{1}{2} \min \left\{ \frac{\Delta x}{\max_j |\hat{a}_{j\pm\frac{1}{2}}^\pm|} \right\} \leq \frac{\Delta t_{spl}}{2}. \quad (3.74)$$

Since Δt_w may be smaller than $\Delta t_{spl}/2$, the end time in the first step of our Strang splitting, the method may require multiple hydrodynamic subsystem evolutions of Δt_w to equal $\Delta t_{spl}/2$.

In the second stage of the splitting, where the morphodynamic subsystem is evolved until Δt_{spl} , we need to satisfy

$$\Delta t_s \leq \Delta t_{spl} \leq \min \left\{ \frac{\Delta x}{2 \max_j |\hat{c}_j^\pm|}, \Delta t_{spl} \right\}. \quad (3.75)$$

In most cases, $\Delta t_s = \Delta t_{spl}$, but if, during the evolution, $\Delta t_s < \Delta t_{spl}$, multiple Δt_s time evolutions may be needed.

For the final stage of our splitting, we will evolve the hydrodynamic subsystem from $t + \Delta t_{spl}/2$ to $t + \Delta t_{spl}$ making sure to satisfy (3.74).

3.5.3.2 Time Evolution of S-SG When the Splitting Time-Step Is Chosen Using the Hydrodynamic Time-Step (S-SG-H)

In this section, we detail how the time evolution is implemented when the splitting time step is chosen using the hydrodynamic time step from (3.73). Then, Δt_{spl} is constrained by the following condition:

$$\Delta t_{spl} \leq \frac{1}{2} \min \left\{ \frac{\Delta x}{\max_j |\hat{a}_{j\pm\frac{1}{2}}^\pm|} \right\} \leq \frac{1}{2} \min \left\{ \frac{\Delta x}{\max_j |\hat{c}_{j\pm\frac{1}{2}}^\pm|} \right\}. \quad (3.76)$$

Since Δt_{spl} is based on the smaller time step associated with the fast moving local speeds of propagation, when evolving the hydrodynamic subsystem to $\Delta t_{spl}/2$, we will always take one step since

$$\Delta t_w \leq \min \left\{ \frac{\Delta x}{2 \max_j |\hat{a}_{j\pm\frac{1}{2}}^\pm|}, \frac{\Delta t_{spl}}{2} \right\}. \quad (3.77)$$

For the evolution of the morphodynamic subsystem which is evolved to Δt_{spl} , since Δt_s is

naturally greater than Δt_{spl} , only take one step in Δt_s . Thus, the CFL is constrained as follows:

$$\Delta t_s < \Delta t_{spl} \leq \min \left\{ \frac{\Delta x}{\max_j |\widehat{a}_{j\pm\frac{1}{2}}^\pm|}, \Delta t_{spl} \right\} \leq \frac{1}{2} \min \left\{ \frac{\Delta x}{\max_j |\widehat{c}_j^\pm|} \right\}. \quad (3.78)$$

For the final stage of our splitting, we will evolve the hydrodynamic subsystem from $t + \Delta t_{spl}/2$ to $t + \Delta t_{spl}$ making sure to satisfy (3.76).

3.6 Numerical Scheme for the Non-Splitting Approach with the Bottom Evolved on a Non-Staggered Discretized Grid (NS-NSG)

The Formulation NS-NSG is based on the non-splitting approach with the bottom evolved on a non-staggered discretized grid. In this scheme the equilibrium variables w, q , and B are solved on the non-staggered discretized grid from Section 3.3.1. In this section, we will be solving all three equations of (3.3) and (3.2) simultaneously. Assuming the solution is know at a time t , the cell averages of the computed solution are

$$\overline{\mathbf{W}}_j^n(t) := \frac{1}{\Delta x} \int_{C_j} \mathbf{W}(x, t^n) dx, \quad (3.79)$$

recalling that \mathbf{W} is composed of the three equilibrium variables w, q , and B . Applying a second order semi-discrete central-upwind formulation to \mathbf{W} , the cell averages are evolved in time based on the following equation:

$$\frac{d}{dt} \overline{\mathbf{W}}_j(t) = \begin{pmatrix} \frac{d}{dt} \overline{\mathbf{U}}_j(t) \\ \frac{d}{dt} \overline{B}_j(t) \end{pmatrix} = \begin{pmatrix} -\frac{\widehat{\mathbf{H}}_{j+\frac{1}{2}}(t) - \widehat{\mathbf{H}}_{j-\frac{1}{2}}(t)}{\Delta x} + \mathbf{S}(t) \\ -\frac{\mathcal{H}_{j+\frac{1}{2}}(t) - \mathcal{H}_{j-\frac{1}{2}}(t)}{\Delta x} \end{pmatrix}, \quad (3.80)$$

where $\widehat{H}_{j\pm\frac{1}{2}}$ and $\mathcal{H}_{j\pm\frac{1}{2}}$ are the numerical fluxes in (3.84) and (3.82) and

$$\overline{\mathbf{S}}_j(t) \approx \frac{1}{\Delta x} \int_{C_j} \mathbf{S}(\mathbf{W}) dx, \quad (3.81)$$

are the cell averages of the source term. For simplicity in the rest of this section, we will drop the notation for t being time dependent where appropriate. The construction of the scheme will

be complete once the numerical fluxes $\widehat{\mathbf{H}}_{j\pm\frac{1}{2}}$ and $\mathcal{H}_{j\pm\frac{1}{2}}$ in (3.82), (3.83), and (3.84), and the source term in (3.81) are computed so that the resulting scheme is well-balanced.

Numerical Fluxes. In (3.80), we use the central upwind fluxes from [50], modifying the local speeds of propagation to \widehat{a}^\pm and \widehat{c}^\pm using (3.13)-(3.16) where appropriate to capture the different speed of the water and sediment waves. These numerical fluxes are given by

$$\begin{aligned} \widehat{H}_{j+\frac{1}{2}}^{(1)}(t) = & \frac{\widehat{a}_{j+\frac{1}{2}}^+ \widehat{F}^{(1)}(\mathbf{W}_{j+\frac{1}{2}}^-) - \widehat{a}_{j+\frac{1}{2}}^- \widehat{F}^{(1)}(\mathbf{W}_{j+\frac{1}{2}}^+)}{\widehat{a}_{j+\frac{1}{2}}^+ - \widehat{a}_{j+\frac{1}{2}}^-} + \frac{\widehat{a}_{j+\frac{1}{2}}^+ \widehat{a}_{j+\frac{1}{2}}^-}{\widehat{a}_{j+\frac{1}{2}}^+ - \widehat{a}_{j+\frac{1}{2}}^-} \left[W_{j+\frac{1}{2}}^{(1)+} - W_{j+\frac{1}{2}}^{(1)-} \right], \quad (3.82) \end{aligned}$$

$$\begin{aligned} \widehat{H}_{j+\frac{1}{2}}^{(2)}(t) = & \frac{\widehat{a}_{j+\frac{1}{2}}^+ \widehat{F}^{(2)}(\mathbf{W}_{j+\frac{1}{2}}^-) - \widehat{a}_{j+\frac{1}{2}}^- \widehat{F}^{(2)}(\mathbf{W}_{j+\frac{1}{2}}^+)}{\widehat{a}_{j+\frac{1}{2}}^+ - \widehat{a}_{j+\frac{1}{2}}^-} + \frac{\widehat{a}_{j+\frac{1}{2}}^+ \widehat{a}_{j+\frac{1}{2}}^-}{\widehat{a}_{j+\frac{1}{2}}^+ - \widehat{a}_{j+\frac{1}{2}}^-} \left[W_{j+\frac{1}{2}}^{(2)+} - W_{j+\frac{1}{2}}^{(2)-} \right], \quad (3.83) \end{aligned}$$

$$\begin{aligned} \mathcal{H}_{j+\frac{1}{2}}(t) = & \frac{\widehat{c}_{j+\frac{1}{2}}^+ q_b(\mathbf{W}_{j+\frac{1}{2}}^-) - \widehat{c}_{j+\frac{1}{2}}^- q_b(\mathbf{W}_{j+\frac{1}{2}}^+)}{\widehat{c}_{j+\frac{1}{2}}^+ - \widehat{c}_{j+\frac{1}{2}}^-} + \frac{\widehat{c}_{j+\frac{1}{2}}^+ \widehat{c}_{j+\frac{1}{2}}^-}{\widehat{c}_{j+\frac{1}{2}}^+ - \widehat{c}_{j+\frac{1}{2}}^-} \left[W_{j+\frac{1}{2}}^{(3)+} - W_{j+\frac{1}{2}}^{(3)-} \right]. \quad (3.84) \end{aligned}$$

Reconstruction. In (3.82)-(3.84), $\mathbf{W}_{j\pm\frac{1}{2}}^\pm$ are the left and right point values of the piecewise linear reconstructions

$$\widetilde{\mathbf{W}}(x) = \sum_j \left[\overline{\mathbf{W}}_j + (\mathbf{W}_x)_j(x - x_j) \right] \cdot \chi_{C_j}(x), \quad (3.85)$$

obtained at the cell interfaces $x = x_{j+\frac{1}{2}}$ by

$$\mathbf{W}_{j+\frac{1}{2}}^+ = \overline{\mathbf{W}}_{j+1} - \frac{\Delta x}{2} (\mathbf{W}_x)_{j+1}, \quad \mathbf{W}_{j+\frac{1}{2}}^- = \overline{\mathbf{W}}_j + \frac{\Delta x}{2} (\mathbf{W}_x)_j.$$

In (3.85), $\chi_{C_j}(x)$ is the characteristic function of the interval C_j , and $(\mathbf{W}_x)_j$ is the numerical derivative computed using a nonlinear limiter in order to reduce oscillations as in (1.93) and (1.94).

Well-Balanced Quadrature for the Geometric Source Terms. In order to ensure the method is well-balanced, a special quadrature should be used to discretize the second component $\overline{S}_j^{(2)}$ of the source term in (3.29) such that it balances with the numerical fluxes. The fluxes at

the discrete level are given by

$$\frac{\widehat{H}_{j-\frac{1}{2}}^{(2)} - \widehat{H}_{j+\frac{1}{2}}^{(2)}}{\Delta x} = \frac{gW_j^{(1)}}{\Delta x} \left(\frac{\widehat{a}_{j+\frac{1}{2}}^+ W_{j+\frac{1}{2}}^{(3)-} - \widehat{a}_{j+\frac{1}{2}}^- W_{j+\frac{1}{2}}^{(3)+}}{\widehat{a}_{j+\frac{1}{2}}^+ - \widehat{a}_{j+\frac{1}{2}}^-} - \frac{\widehat{a}_{j-\frac{1}{2}}^+ W_{j-\frac{1}{2}}^{(3)-} - \widehat{a}_{j-\frac{1}{2}}^- W_{j-\frac{1}{2}}^{(3)+}}{\widehat{a}_{j-\frac{1}{2}}^+ - \widehat{a}_{j-\frac{1}{2}}^-} \right).$$

Therefore, the fluxes and source term will balance if the second component of the source term is discretized as follows:

$$\overline{S}_j^{(2)} \approx -\frac{gW_j^{(1)}}{\Delta x} \left(\frac{\widehat{a}_{j+\frac{1}{2}}^+ W_{j+\frac{1}{2}}^{(3)-} - \widehat{a}_{j+\frac{1}{2}}^- W_{j+\frac{1}{2}}^{(3)+}}{\widehat{a}_{j+\frac{1}{2}}^+ - \widehat{a}_{j+\frac{1}{2}}^-} - \frac{\widehat{a}_{j-\frac{1}{2}}^+ W_{j-\frac{1}{2}}^{(3)-} - \widehat{a}_{j-\frac{1}{2}}^- W_{j-\frac{1}{2}}^{(3)+}}{\widehat{a}_{j-\frac{1}{2}}^+ - \widehat{a}_{j-\frac{1}{2}}^-} \right). \quad (3.86)$$

Local Speeds of Propagation. The local speeds of propagation for the water waves and sediment waves are obtained by using the eigenvalues corresponding to their respective systems given by

$$\begin{aligned} \widehat{a}_{j+\frac{1}{2}}^+ &= \max \left\{ \lambda_{j+\frac{1}{2}}^{(1)+}, \lambda_{j+\frac{1}{2}}^{(3)+}, \lambda_{j+\frac{1}{2}}^{(1)-}, \lambda_{j+\frac{1}{2}}^{(3)-}, 0 \right\}, \\ \widehat{a}_{j+\frac{1}{2}}^- &= \min \left\{ \lambda_{j+\frac{1}{2}}^{(1)+}, \lambda_{j+\frac{1}{2}}^{(3)+}, \lambda_{j+\frac{1}{2}}^{(1)-}, \lambda_{j+\frac{1}{2}}^{(3)-}, 0 \right\}, \\ \widehat{c}_{j+\frac{1}{2}}^+ &= \max \left\{ \lambda_{j+\frac{1}{2}}^{(2)+}, \lambda_{j+\frac{1}{2}}^{(2)-}, 0 \right\}, \\ \widehat{c}_{j+\frac{1}{2}}^- &= \min \left\{ \lambda_{j+\frac{1}{2}}^{(2)+}, \lambda_{j+\frac{1}{2}}^{(2)-}, 0 \right\}. \end{aligned} \quad (3.87)$$

3.6.1 Time Evolution of NS-NSG

To find the time step Δt , we compare all the local speeds of propagation together, and our time step must satisfy the condition given by

$$\Delta t \leq \frac{1}{2} \min \left\{ \frac{\Delta x}{\max_j |\widehat{a}_{j\pm\frac{1}{2}}^\pm|}, \frac{\Delta x}{\max_j |\widehat{c}_{j\pm\frac{1}{2}}^\pm|} \right\}. \quad (3.88)$$

3.7 Numerical Scheme for the Non-Splitting Approach with the Bottom Evolved on a Staggered Discretized Grid (NS-SG)

The Formulation NS-SG is based on the non-splitting approach with the bottom evolved on a staggered discretized grid. In this scheme, the spatial discretization from Section 3.3.2 is used where $\overline{\mathbf{U}}$ is on a non-staggered discretized grid and \overline{B} is on staggered discretized grid. Since the system is not solved using splitting, we need to consider all three equations at once. Therefore, we work simultaneously on the non-staggered and staggered discretized grids. For ease of the

reader, we will refer to the variables on the non-staggered discretized grid by \mathbf{W}^{ns} and the variables on the staggered discretized grid by \mathbf{W}^s . The computed solution for the cell averages on the non-staggered discretized grid,

$$\overline{\mathbf{W}}_j^{ns}(t) \approx \frac{1}{\Delta x} \int_{C_j} \mathbf{W}^{ns}(x, t) dx, \quad (3.89)$$

are assumed to be known at a given time t . The cell averages on the staggered discretized grid are slightly more complicated as the first two values of \mathbf{W}^s are calculated using the method from [68] to obtain

$$\overline{W}_{j+\frac{1}{2}}^{s(1)} = \int_{C_{j+\frac{1}{2}}} W^{s(1)}(x) dx = \frac{1}{2} \left(\overline{W}_j^{ns(1)} + \overline{W}_{j+1}^{ns(1)} \right) + \frac{1}{8} \left[\left(\overline{W}_x^{ns(1)} \right)_j - \left(\overline{W}_x^{ns(1)} \right)_{j+1} \right], \quad (3.90)$$

$$\overline{W}_{j+\frac{1}{2}}^{s(2)} = \int_{C_{j+\frac{1}{2}}} W^{s(2)}(x) dx = \frac{1}{2} \left(\overline{W}_j^{ns(2)} + \overline{W}_{j+1}^{ns(2)} \right) + \frac{1}{8} \left[\left(\overline{W}_x^{ns(2)} \right)_j - \left(\overline{W}_x^{ns(2)} \right)_{j+1} \right], \quad (3.91)$$

where $\left(\overline{W}_x^{ns(1)} \right)_j$, $\left(\overline{W}_x^{ns(1)} \right)_{j+1}$, $\left(\overline{W}_x^{ns(2)} \right)_j$, and $\left(\overline{W}_x^{ns(2)} \right)_{j+1}$ are numerical derivatives calculated in the reconstruction step of this section. For the third value of \mathbf{W}^s , which represents the bottom topography function B , we calculate $W^{s(3)}$ as

$$\overline{W}_j^{s(3)}(t) \approx \frac{1}{\Delta x} \int_{C_{j+\frac{1}{2}}} W^{s(3)}(x, t) dx. \quad (3.92)$$

Applying a second order semi-discrete central-upwind formulation to \mathbf{W} , we solve all three equations simultaneously as

$$\frac{d}{dt} \overline{\mathbf{W}}_j(t) = \begin{pmatrix} \frac{d}{dt} \overline{W}_j^{ns(1)}(t) \\ \frac{d}{dt} \overline{W}_j^{ns(2)}(t) \\ \frac{d}{dt} \overline{W}_{j+\frac{1}{2}}^{s(3)}(t) \end{pmatrix} = \begin{pmatrix} -\frac{\hat{H}_{j+\frac{1}{2}}^{(1)}(t) - \hat{H}_{j-\frac{1}{2}}^{(1)}(t)}{\Delta x} + \overline{S}_j^{(1)}(t) \\ -\frac{\hat{H}_{j+\frac{1}{2}}^{(2)}(t) - \hat{H}_{j-\frac{1}{2}}^{(2)}(t)}{\Delta x} + \overline{S}_j^{(2)}(t) \\ -\frac{\mathcal{H}_{j+1}(t) - \mathcal{H}_j(t)}{\Delta x} \end{pmatrix}, \quad (3.93)$$

where $\widehat{\mathbf{H}}_{j+\frac{1}{2}}$ and \mathcal{H}_{j+1} are the central-upwind fluxes and $\overline{\mathbf{S}}(t)$ is given by

$$\overline{\mathbf{S}}_j(t) \approx \frac{1}{\Delta x} \int_{C_j} \mathbf{S}(\mathbf{W}) dx, \quad (3.94)$$

which represents the cell averages of the geometric source term. For the rest of this section we will drop the notation t for time dependence for simplicity where it is appropriate.

The construction of the scheme will be complete once the numerical fluxes $\widehat{\mathbf{H}}_{j+\frac{1}{2}}$ and \mathcal{H}_{j+1} in (3.95)-(3.97) and the source term $\overline{\mathbf{S}}_j$ in (3.94) are computed such that the resulting method is well-balanced.

Numerical Fluxes. In (3.93), we use the central-upwind fluxes from [50], slightly modifying the local speeds of propagation to $\widehat{a}_{j+\frac{1}{2}}^\pm$ and \widehat{c}_j^\pm using (3.13)-(3.16) where appropriate, to capture the different speeds of the water and sediment. These numerical fluxes are given by

$$\begin{aligned} \widehat{H}_{j+\frac{1}{2}}^{(1)}(t) = & \frac{\widehat{a}_{j+\frac{1}{2}}^+ \widehat{F}^{(1)}(W_{j+\frac{1}{2}}^{ns-}) - \widehat{a}_{j+\frac{1}{2}}^- \widehat{F}^{(1)}(W_{j+\frac{1}{2}}^{ns+})}{\widehat{a}_{j+\frac{1}{2}}^+ - \widehat{a}_{j+\frac{1}{2}}^-} + \frac{\widehat{a}_{j+\frac{1}{2}}^+ \widehat{a}_{j+\frac{1}{2}}^-}{\widehat{a}_{j+\frac{1}{2}}^+ - \widehat{a}_{j+\frac{1}{2}}^-} \left[W_{j+\frac{1}{2}}^{ns(1)+} - W_{j+\frac{1}{2}}^{ns(1)-} \right], \end{aligned} \quad (3.95)$$

$$\begin{aligned} \widehat{H}_{j+\frac{1}{2}}^{(2)}(t) = & \frac{\widehat{a}_{j+\frac{1}{2}}^+ \widehat{F}^{(2)}(W_{j+\frac{1}{2}}^{ns-}) - \widehat{a}_{j+\frac{1}{2}}^- \widehat{F}^{(2)}(W_{j+\frac{1}{2}}^{ns+})}{\widehat{a}_{j+\frac{1}{2}}^+ - \widehat{a}_{j+\frac{1}{2}}^-} + \frac{\widehat{a}_{j+\frac{1}{2}}^+ \widehat{a}_{j+\frac{1}{2}}^-}{\widehat{a}_{j+\frac{1}{2}}^+ - \widehat{a}_{j+\frac{1}{2}}^-} \left[W_{j+\frac{1}{2}}^{ns(2)+} - W_{j+\frac{1}{2}}^{ns(2)-} \right], \end{aligned} \quad (3.96)$$

$$\begin{aligned} \mathcal{H}_{j+1}(t) = & \frac{\widehat{c}_{j+1}^+ q_b(W_{j+1}^{s-}) - \widehat{c}_{j+1}^- q_b(W_{j+1}^{s+})}{\widehat{c}_{j+1}^+ - \widehat{c}_{j+1}^-} + \frac{\widehat{c}_{j+1}^+ \widehat{c}_{j+1}^-}{\widehat{c}_{j+1}^+ - \widehat{c}_{j+1}^-} \left[W_{j+1}^{s(3)+} - W_{j+1}^{s(3)-} \right]. \end{aligned} \quad (3.97)$$

Reconstruction. In (3.95)-(3.97), $\mathbf{W}_{j+\frac{1}{2}}^{ns\pm}$ and $\mathbf{W}_{j+1}^{s\pm}$ are the left and right point values of the piecewise linear reconstructions

$$\widetilde{\mathbf{W}}^{ns}(x) = \sum_j \left[\overline{\mathbf{W}}_j^{ns} + (\mathbf{W}_x^{ns})_j(x - x_j) \right] \cdot \chi_{C_j}(x), \quad (3.98)$$

$$\widetilde{\mathbf{W}}^s(x) = \sum_j \left[\overline{\mathbf{W}}_{j+\frac{1}{2}}^s + (\mathbf{W}_x^s)_{j+\frac{1}{2}}(x - x_{j+\frac{1}{2}}) \right] \cdot \chi_{C_{j+\frac{1}{2}}}(x), \quad (3.99)$$

obtained at the midpoint cell interfaces $x = x_{j+\frac{1}{2}}$, $x = x_{j-\frac{1}{2}}$, $x = x_j$, and $x = x_{j+1}$ on the non-staggered and staggered discretized grids given by

$$\mathbf{W}_{j+\frac{1}{2}}^{ns+} = \overline{\mathbf{W}}_{j+1}^{ns} - \frac{\Delta x}{2} (\mathbf{W}_x^{ns})_{j+1} \quad , \quad \mathbf{W}_{j+\frac{1}{2}}^{ns-} = \overline{\mathbf{W}}_j^{ns} + \frac{\Delta x}{2} (\mathbf{W}_x^{ns})_j \quad , \quad (3.100)$$

$$\mathbf{W}_{j+1}^{s+} = \overline{\mathbf{W}}_{j+\frac{3}{2}}^s - \frac{\Delta x}{2} (\mathbf{W}_x^s)_{j+\frac{3}{2}} \quad , \quad \mathbf{W}_{j+1}^{s-} = \overline{\mathbf{W}}_{j+\frac{1}{2}}^s + \frac{\Delta x}{2} (\mathbf{W}_x^s)_{j+\frac{1}{2}} \quad . \quad (3.101)$$

The numerical derivatives $(\mathbf{W}_x^{ns})_j$ and $(\mathbf{W}_x^s)_{j+\frac{1}{2}}$ are then computed using a nonlinear limiter in order to reduce oscillations as

$$\begin{aligned} (\mathbf{W}_x^{ns})_j &= \text{minmod} \left(\theta \frac{\overline{\mathbf{W}}_j^{ns} - \overline{\mathbf{W}}_{j-1}^{ns}}{\Delta x}, \frac{\overline{\mathbf{W}}_{j+1}^{ns} - \overline{\mathbf{W}}_{j-1}^{ns}}{2\Delta x}, \theta \frac{\overline{\mathbf{W}}_{j+1}^{ns} - \overline{\mathbf{W}}_j^{ns}}{\Delta x} \right), \quad \theta \in [1, 2], \\ (\mathbf{W}_x^s)_{j+\frac{1}{2}} &= \text{minmod} \left(\theta \frac{\overline{\mathbf{W}}_{j+\frac{1}{2}}^s - \overline{\mathbf{W}}_{j-\frac{1}{2}}^s}{\Delta x}, \frac{\overline{\mathbf{W}}_{j+\frac{3}{2}}^s - \overline{\mathbf{W}}_{j-\frac{1}{2}}^s}{2\Delta x}, \theta \frac{\overline{\mathbf{W}}_{j+\frac{3}{2}}^s - \overline{\mathbf{W}}_{j+\frac{1}{2}}^s}{\Delta x} \right), \quad \theta \in [1, 2], \end{aligned}$$

where the minmod limiter is defined as in (1.94).

Well-Balanced Quadrature for the Geometric Source Terms. In order to ensure the method is well-balanced, a special quadrature should be used to discretize the second component $\overline{S}_j^{(2)}$ of the source term in (3.94) such that it balances with the numerical fluxes. The fluxes at the discrete level are given by

$$\frac{\widehat{H}_{j-\frac{1}{2}}^{(2)} - \widehat{H}_{j+\frac{1}{2}}^{(2)}}{\Delta x} = \frac{g\overline{w}_j}{\Delta x} \left(\frac{\widehat{a}_{j+\frac{1}{2}}^+ W_{j+\frac{1}{2}}^{s(3)} - \widehat{a}_{j+\frac{1}{2}}^- W_{j+\frac{1}{2}}^{s(3)}}{\widehat{a}_{j+\frac{1}{2}}^+ - \widehat{a}_{j+\frac{1}{2}}^-} - \frac{\widehat{a}_{j-\frac{1}{2}}^+ W_{j-\frac{1}{2}}^{s(3)} - \widehat{a}_{j-\frac{1}{2}}^- W_{j-\frac{1}{2}}^{s(3)}}{\widehat{a}_{j-\frac{1}{2}}^+ - \widehat{a}_{j-\frac{1}{2}}^-} \right), \quad (3.102)$$

$$= \frac{g\overline{w}_j}{\Delta x} \left(W_{j+\frac{1}{2}}^{s(3)} - W_{j-\frac{1}{2}}^{s(3)-} \right). \quad (3.103)$$

Therefore, the fluxes and source term will balance if the second component of the source term is discretized as follows:

$$\overline{S}_j^{(2)} \approx -\frac{g\overline{w}_j}{\Delta x} \left(W_{j+\frac{1}{2}}^{s(3)} - W_{j-\frac{1}{2}}^{s(3)-} \right). \quad (3.104)$$

Local Speeds of Propagation. The local speeds of propagation for the water waves are obtained from the eigenvalues corresponding to the shallow water equations evaluated on the non-staggered discretized grid. Meanwhile, the local speeds of propagation for the sediment waves are obtained from the eigenvalues corresponding to the Exner equation evaluated on the

staggered discretized grid. Therefore, we have

$$\begin{aligned}
\widehat{a}_{j+\frac{1}{2}}^+ &= \max \left\{ \lambda_{j+\frac{1}{2}}^{(1)+}, \lambda_{j+\frac{1}{2}}^{(3)+}, \lambda_{j+\frac{1}{2}}^{(1)-}, \lambda_{j+\frac{1}{2}}^{(3)-}, 0 \right\}, \\
\widehat{a}_{j+\frac{1}{2}}^- &= \min \left\{ \lambda_{j+\frac{1}{2}}^{(1)+}, \lambda_{j+\frac{1}{2}}^{(3)+}, \lambda_{j+\frac{1}{2}}^{(1)-}, \lambda_{j+\frac{1}{2}}^{(3)-}, 0 \right\}, \\
\widehat{c}_{j+1}^+ &= \max \left\{ \lambda_{j+1}^{(2)+}, \lambda_{j+1}^{(2)-}, 0 \right\}, \\
\widehat{c}_{j+1}^- &= \min \left\{ \lambda_{j+1}^{(2)+}, \lambda_{j+1}^{(2)-}, 0 \right\}.
\end{aligned} \tag{3.105}$$

3.7.1 Time Evolution of NS-SG.

Our time step Δt must satisfy the CFL condition no matter which local speeds of propagation are used. Therefore, the condition our time step must satisfy is given by

$$\Delta t \leq \frac{1}{2} \min \left\{ \frac{\Delta x}{\max_j |\widehat{a}_{j\pm\frac{1}{2}}^\pm|}, \frac{\Delta x}{\max_j |\widehat{c}_j^+|} \right\}. \tag{3.106}$$

3.8 Numerical Examples

In this section, we present six numerical examples. In all examples, a third order Strong Stability Preserving Runge Kutta (SSP-RK3) ODE solver from [29] is used, as well as an adaptive time step strategy from [14], which are outlined in Appendix A and Appendix B, respectively. All the examples, unless otherwise noted, are computed using the minmod limiter with $\theta = 1.3$, $\xi = 5/3$, $g = 9.8$, $\kappa = 0.9$ in the adaptive time evolution, $m = 3$ for Grass's Model in (3.4), N represents the number of computational cells the domain is broken into, and there are free flow boundary conditions on all sides of the domain. All of the computations were performed on a 2013 MacBook Pro running macOS Sierra with a 2.6Ghz Intel Core i5 Processor with 8Gb 1600 Mhz DDR3 Memory.

3.8.1 Example 1 – Comparison of Numerical Formulations

In this example, we recreate the computed results of Cordier et al. in [18] where they compared a splitting and a non-splitting method for solving the combined shallow water system with Exner equation (3.3) and (3.2). The problem statement and initial condition are given by

$$\begin{cases} hu(x, t = 0) = 0.5, \\ B(x, t = 0) = 0.1 + 0.1e^{-(x-5)^2}, \\ \frac{u^2}{2} + g(h + B) = 6.386, \end{cases}$$

with $\xi = 1$, $A = 0.07$, and solved until time $t = 2.1$. Figure 3.3 shows the initial conditions at time $t = 0$ with $N = 400$ cells resulting in $\Delta x = 0.025$.

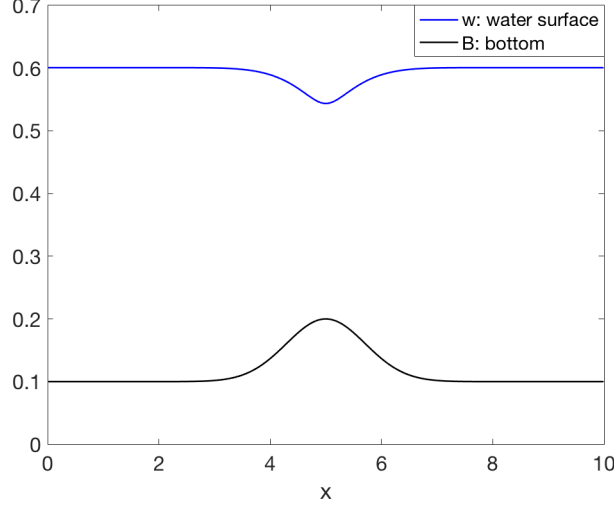


Figure 3.3: Example 1: Initial conditions at $t = 0$ with $N = 400$.

The results of the computed solutions at $t = 2.1$ of the various numerical schemes (S-NSG-M, S-NSG-H, S-SG-M, S-SG-H, NS-NSG, NS-SG) can be seen in Figure 3.4, which plots the computed solutions which use the staggered discretized grid, and Figure 3.5, which plots the computed solutions which use the non-staggered discretized grid.

Comparing the various computed solutions for Example 1, each numerical scheme produced similar results with a large mound propagating to the right and a smaller mound propagating to the left. Both of these results match well with the computed results seen in [18]. Since all of the numerical schemes produced similar results, for the rest of this thesis we will only plot the computed solutions correspond to the NS-NSG numerical scheme. The NS-NSG numerical scheme was found to have the fastest computational run time (see Table 3.1). In addition, since the NS-NSG numerical scheme is based on non-splitting approach, the scheme is capable of handling when the magnitude of the water wave speed and sediment wave speed are either similar or dissimilar in magnitude, making it more robust.

3.8.2 Example 2 – Test of Order

In this example, we consider a test of order problem from [21]. We consider a 1-D channel on the interval $[-10, 10]$ with the sediment interaction of Grass formula set to $A = 0.3$, a final time

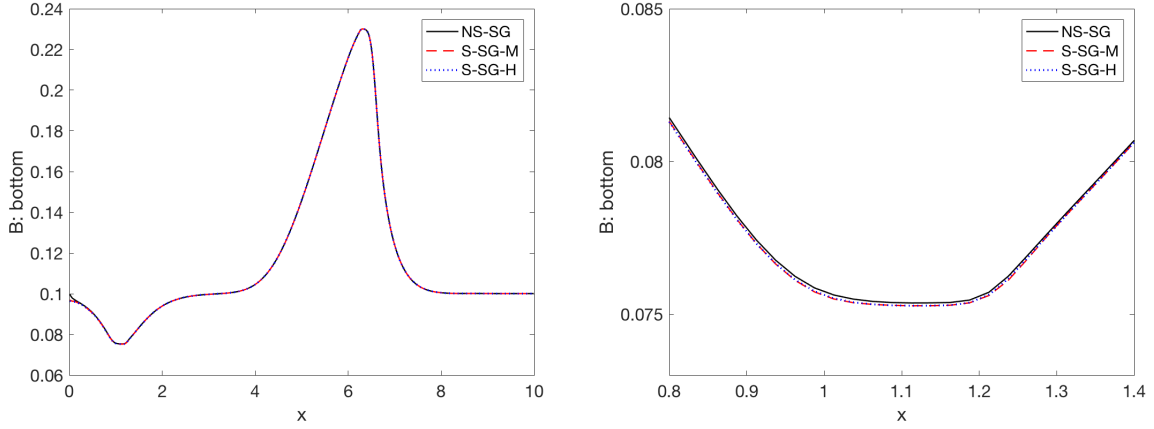


Figure 3.4: Example 1: NS-SG, S-SG-M, and S-SG-H solutions (B) computed using $N = 400$ at $t = 2.1$. Right zoom into the region $x \in [0.8, 1.4]$.

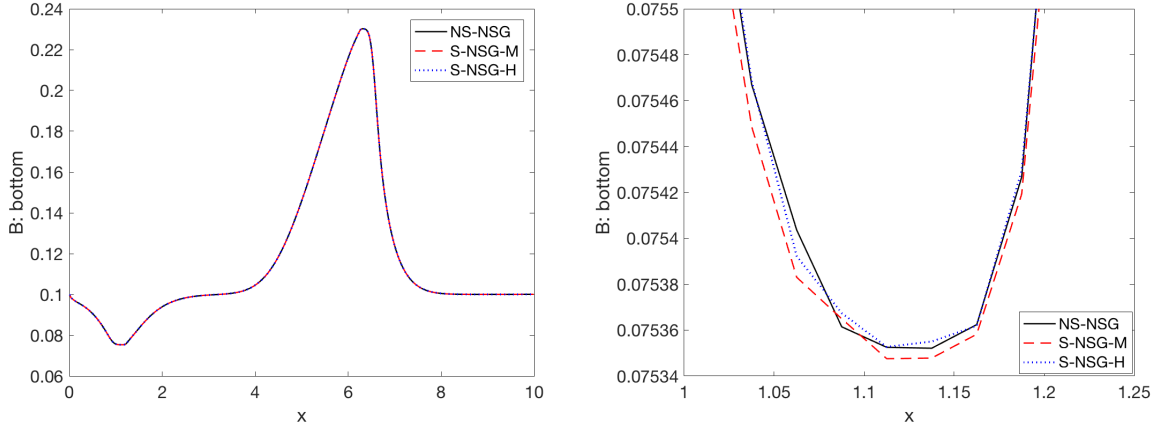


Figure 3.5: Example 1: NS-NSG, S-NSG-M, and S-NSG-H solutions (B) computed using $N = 400$ at $t = 2.1$. Right zoom into the region $x \in [1.0, 1.25]$.

of $t = 0.5$ and with initial conditions given by

$$h(x, 0) = 2 - 0.1e^{-x^2}, \quad q(x, 0) = 0, \quad B(x, 0) = 0.1 - 0.01e^{-x^2}.$$

The exact solution is unknown, so we will compare to a numerical reference solution computed on a fine grid of 6400 cells. The computed results are presented in Figure 3.6. The error and order of convergence for h, q , and B can be seen in Table 3.2.

As one can see in Figure 3.6, as the grid is refined our computed solutions approach the

Table 3.1: Example 1: Computation time for various formulations.

Formulation	Computation Run Time for Example 1 (seconds)
NS-NSG	0.33
NS-SG	0.58
S-SG-M	7.26
S-NSG-M	7.70
S-NSG-H	12.41
S-SG-H	13.36

Table 3.2: Example 2: L^1 Error and Order of Convergence.

N	L^1 err h	L^1 order h	L^1 err q	L^1 order q	L^1 err B	L^1 order B
100	0.0084	–	0.0365	–	7.80E-5	–
200	0.0023	1.88	0.0101	1.86	2.32E-5	1.73
400	6.24E-4	1.89	0.0027	1.92	6.32E-6	1.87
800	1.57E-4	1.99	6.66E-4	2.01	1.49E-6	2.09

numerical reference solution. In Table 3.2, one can also see that h , q , and B all exhibit a second order rate of convergence.

3.8.3 Example 3 – Sediment Mound Interacting Slowly with the Water Flow

In this example, see in [36] we simulate a sediment mound interacting slowly with the water flow when the water is moving slowly. The computational domain is $[0, 1000]$ with initial data,

$$w(x, 0) = 10, \quad hu(x, 0) = 10,$$

and the bottom topography is given by

$$B(x, 0) = \begin{cases} \sin^2 \left(\frac{\pi(x-300)}{200} \right), & 300 \leq x \leq 500, \\ 0, & \text{otherwise.} \end{cases}$$

We also take $A = .001$ and $t = 238079$.

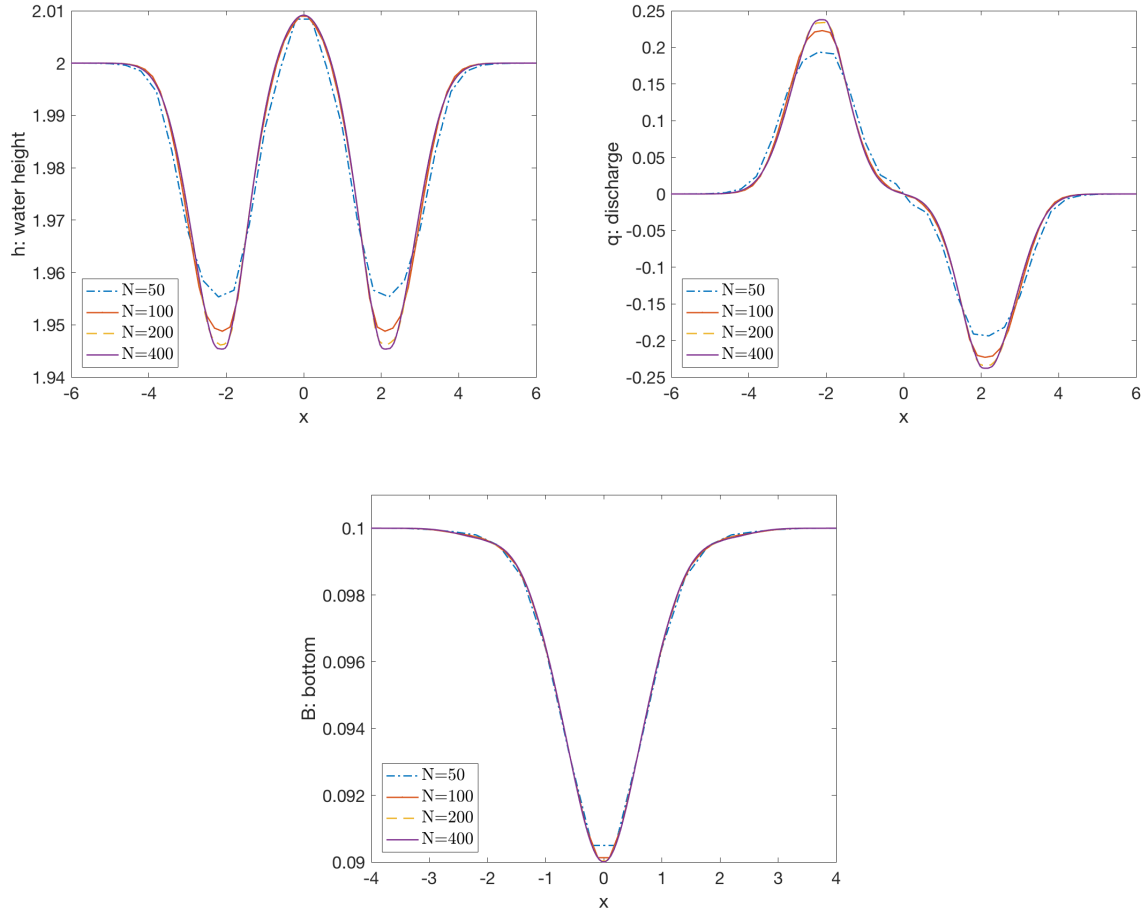


Figure 3.6: Example 2: Solution (h in upper left, u in upper right, and B on bottom) computed with $N = 50$, $N = 100$, $N = 200$, $N = 400$ at $t = 1.05$.

In Figure 3.7, we compare the computed solution for the NS-NSG numerical scheme with a computational domain of 100, 200, and 400 cells, and a computed approximate solution plotted from a formula in [36]. In Figure 3.7, the approximate solution depicts the sediment mound propagating to the right, and the computed numerical solutions with $N = 100$, $N = 200$, and $N = 400$ converging to the approximate solution as the number of computational cells doubles.

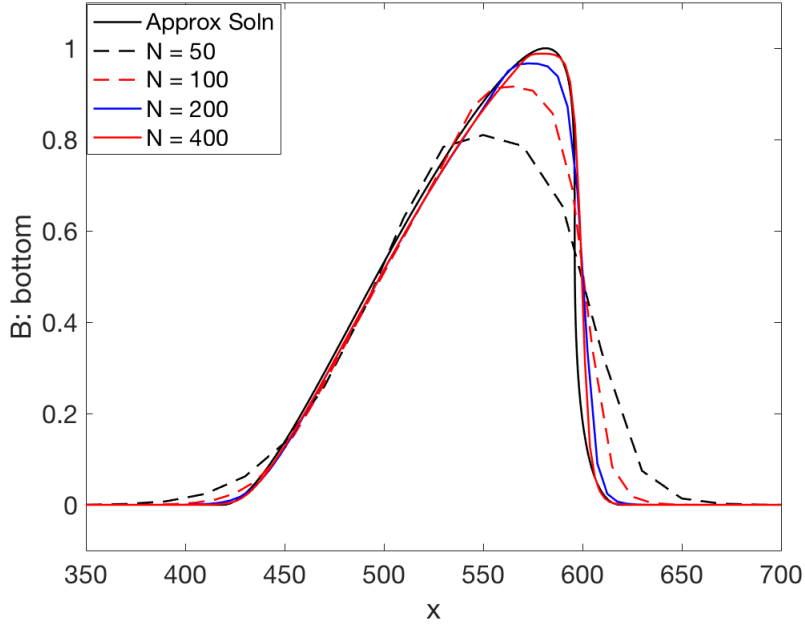


Figure 3.7: Example 3: Solution (B) computed with $N = 50$, $N = 100$, $N = 200$, $N = 400$, and approximate solution at $t = 238709$.

3.8.4 Example 4 – Sediment Mound Interacting Quickly with the Water Flow

In this example, we simulate a sediment mound interacting quickly with the water flow when the water is moving slowly, as seen in [36]. The computational domain is $[0, 1000]$ with initial data

$$w(x, 0) = 10, \quad hu(x, 0) = 10,$$

and the bottom topography is given by

$$B(x, 0) = \begin{cases} \sin^2\left(\frac{\pi(x-300)}{200}\right), & 300 \leq x \leq 500, \\ 0, & \text{otherwise.} \end{cases}$$

We take $A = 1.0$ and compute until $t = 238$.

In Figure 3.8, we plot the initial condition along with the solution computed at time $t = 238$ using $N = 100$, $N = 200$, and $N = 400$ computational cells, using the NS-NSG numerical scheme (right). As well a modified implementation of the NS-NSG scheme, determining the local speeds of propagation by the largest and smallest eigenvalues of the full system from (3.3) and (3.2), not taking into account the difference in wave speeds for the water and sedi-

ment (left). Overall, both of the solutions plotted in Figure 3.8 capture the propagation of the mound moving to the right, matching well with the computed results in [36]. In comparison, the numerical scheme with the local speeds of propagation determined from the eigenvalues of the full system (left) showed additional diffusion in the computed solution for the bottom B . This was not present in the computed solution for the bottom using the NS-NSG scheme (right). This difference in solutions was particularly noticeable on a coarse grid.

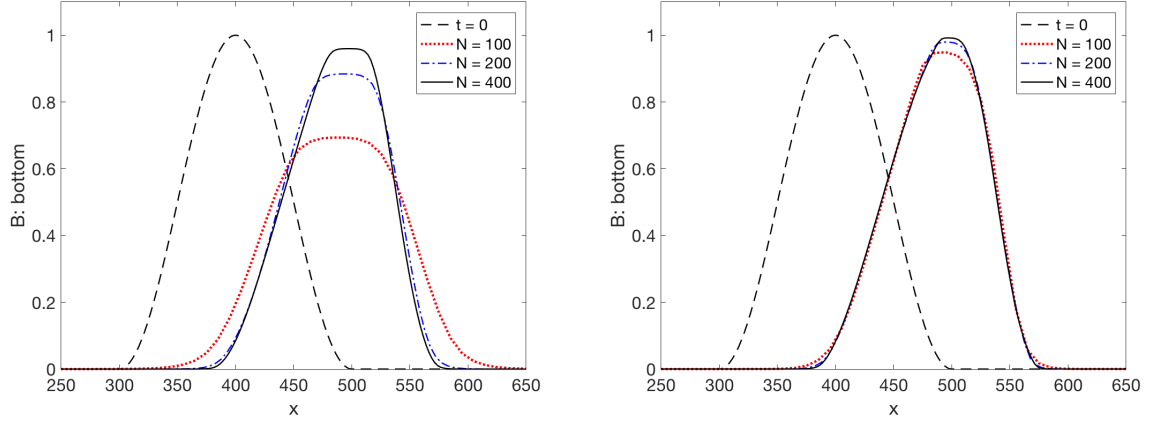


Figure 3.8: Example 4: Solutions (B) computed at $t = 0$ with $N = 400$ and at $t = 238$ with $N = 100$, $N = 200$, and $N = 400$ using water wave speed for the sediment (left) and using the sediment wave speed for the sediment (right).

3.8.5 Example 5 – Sediment Mound Interacting Slowly with a Large Velocity Water Flow

In this example, we simulate a sediment mound interacting quickly with the water flow, but the water flow is also moving quickly (from [36]). The computational domain is $[0, 1000]$ with initial data

$$w(x, 0) = 10, \quad hu(x, 0) = 50,$$

and the bottom topography is given by

$$B(x, 0) = \begin{cases} \sin^2\left(\frac{\pi(x-300)}{200}\right), & 300 \leq x \leq 500, \\ 0, & \text{otherwise.} \end{cases}$$

We take $A = 1.0$ and compute until $t = 1904$.

In Figure 3.9, we plot the initial condition along with the solution computed at time $t = 1904$ using the NS-NSG numerical scheme. The computed solution with $N = 400$ computational cells captures the propagation of the sediment to the right, with the results matching well with the reported results in [36]. This demonstrates that our method is capable of capturing the interaction between water and sediment when water with a large velocity is present.

We note that Grass' formula for bed load sediment transport does not take into account the effects of gravity. This may result in sediment particles located at the front of an advancing dune not falling due to gravity, as they only depend on the sediment constants and the hydrodynamic variable. As a result, a vertical profile at the advancing front of a dune may be observed in numerical simulations which is not physical in nature.

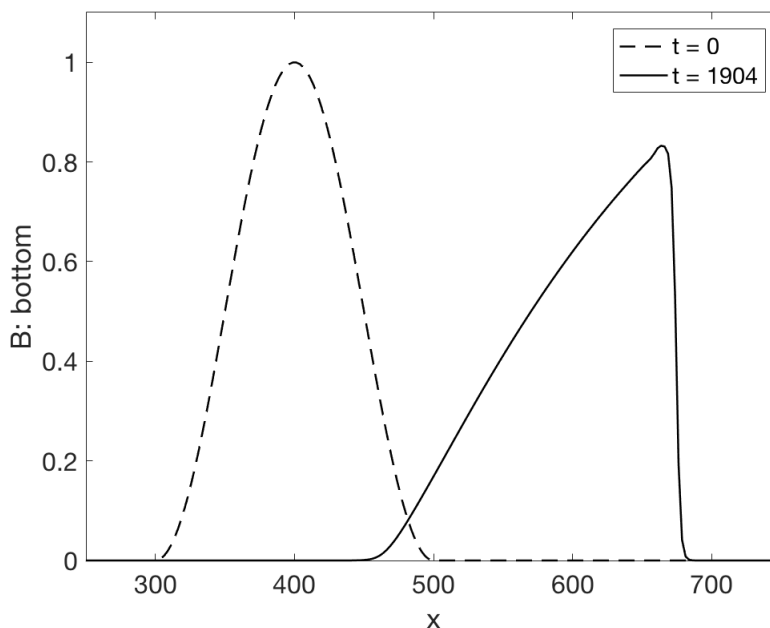


Figure 3.9: Example 5: Solution (B) computed with $N = 400$ at $t = 1904$.

3.8.6 Example 6 – Small Discontinuity in Sediment Bed

In this problem, taken from [36], we run the problem when the bed has a small discontinuity. The computational domain is $[0, 1000]$ with initial data

$$w(x, 0) = 10, \quad hu(x, 0) = 10,$$

and the bottom topography is given by

$$B(x, 0) = \begin{cases} 1, & x \leq 300, \\ 0, & \text{otherwise.} \end{cases}$$

We take $A = .001$ and compute until $t = 900000$.

In Figure 3.10, we plot the initial condition along with the solution computed at $t = 900000$. As one can observe, the discontinuity initially present propagates to the right, indicating proper numerical handling of the discontinuity by the NS-NSG numerical scheme.

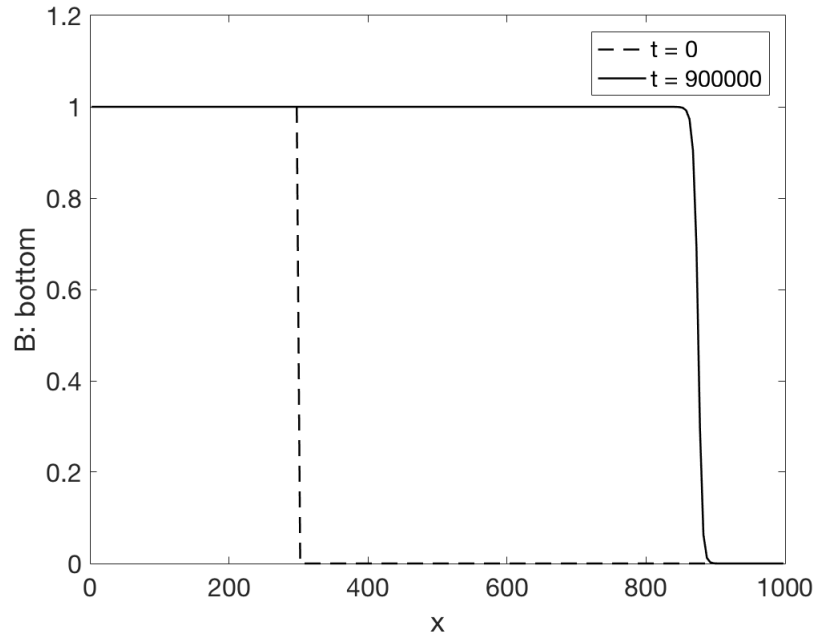


Figure 3.10: Example 6: Solution (B) computed with $N = 200$ at $t = 0$ and $t = 900000$.

3.9 Conclusion

In this chapter, we implemented four second order central-upwind schemes which are well-balanced when applied to the 1-D shallow water equations with 1-D Exner equation to govern sediment transport. We were successful in determining the eigenvalues for our complete system and to which part of the system, shallow water or Exner, the eigenvalues corresponded. We used this information to incorporate only the relevant eigenvalues for the local speeds of propagation

for the water or sediment. We obtained better results than the straightforward implementation of the central scheme, which only takes into account the largest and smallest eigenvalues of the Jacobian. In Section 3.8, we presented a number of numerical results in which we verified that the NS-NSG numerical scheme is second order and can numerically handle when the sediment interaction with the water is slow or fast with a slow moving water flow. For the case of slow sediment interaction, we were also able to obtain a solution when the water flow was fast. Finally, we demonstrated that the NS-NSG numerical scheme was capable of propagating a discontinuity to the correct location, indicating proper numerical handling of the discontinuity and usefulness in capturing shocks.

Chapter 4

2-D Shallow Water Equations with Exner Equation

In this chapter, we discuss a numerical scheme to solve the 2-D system of shallow water equations with a 2-D Exner equation to govern sediment transport. We start by recalling the 2-D system of shallow water equations represented by

$$\begin{pmatrix} h \\ hu \\ hv \end{pmatrix}_t + \begin{pmatrix} hu \\ hu^2 + \frac{g}{2}h^2 \\ huv \end{pmatrix}_x + \begin{pmatrix} hv \\ huv \\ hv^2 + \frac{g}{2}h^2 \end{pmatrix}_y = \begin{pmatrix} 0 \\ -ghB_x \\ -ghB_y \end{pmatrix}, \quad (4.1)$$

with 2-D Exner equation to govern sediment transport given by

$$B_t + (\xi q_{b_1})_x + (\xi q_{b_2})_y = 0, \quad (4.2)$$

where the variable $\xi = \frac{1}{1-\epsilon}$ is a constant with ϵ representing the porosity of the sediment layer.

We can rewrite the complete system of 2-D shallow water equations with 2-D Exner equation in terms of the equilibrium variables by adding (4.2) to the first equation of (4.1) and rearranging the second and third equations of (4.1). This new system of equations can be written using a new unknown vector of equilibrium variables $\mathcal{W} = (w, q, p, B)^\top$:

$$\mathcal{W} + \mathcal{F}(\mathcal{W})_x + \mathcal{G}(\mathcal{W})_y = \hat{S}(\mathcal{W}), \quad (4.3)$$

where $\mathcal{F}(\mathcal{W}) = \left(q + \xi q_{b_1}, \frac{q^2}{w-B} + \frac{g}{2}(w^2 - 2wB), \frac{qp}{w-B}, \xi q_{b_1} \right)^\top$, $\mathcal{G}(\mathcal{W}) = \left(p + \xi q_{b_2}, \frac{qp}{w-B}, \frac{p^2}{w-B} + \right.$

$$\frac{g}{2}(w - B)^2, \xi q_{b_2} \Big)^\top, \text{ and } \widehat{\mathbf{S}}(\mathbf{W}) = (0, -gwB_x, -gwB_y, 0)^\top.$$

Recall, we define $q_{b_1}(h, u, v)$ to be the sediment discharge in the x -direction, and $q_{b_2}(h, u, v)$ is the sediment transport discharge in the y -direction. We define q_{b_1} and q_{b_2} using the sediment fluxes formula proposed by Grass [30] for 2-D by

$$\begin{aligned} q_{b_1} &= Au (u^2 + v^2)^{(m-1)/2}, \\ q_{b_2} &= Av (u^2 + v^2)^{(m-1)/2}, \end{aligned} \tag{4.4}$$

where A is a non-dimensional constant which accounts for the effects of sediment grain size and kinematic viscosity. The value of A is in the interval $[0, 1]$ and the closer A is to zero, the weaker the interaction between the sediment and fluid. The constant A is often computed from experimental data. Lastly, m represents a constant value $1 \leq m \leq 4$, and, in our numerical experiments, we will use $m = 3$.

In Section 4.1, we calculate the eigenvalues of (4.3) for the local speeds of propagation in our numerical scheme. As in Section 3.2, we explain how to distinguish which eigenvalues correspond to the 2-D shallow water system and which eigenvalues correspond to the 2-D Exner equation.

4.1 Eigenvalues for the Jacobian of the 2D Shallow Water System with Exner Equation

To simplify the computations, we use the primitive variables $\mathbf{W}_p = (h, u, v, B)^\top$ and flux functions $\mathcal{F}_p = [hu, hu^2 + \frac{1}{2}, huv, \xi Au(u^2 + v^2)]^\top$ and $\mathcal{G}_p = [hv, huv, hv^2 + \frac{1}{2}gh^2, \xi Av(u^2 + v^2)]$. The Jacobian in the x -direction is given by

$$\frac{\partial \mathcal{F}_p}{\partial \mathbf{W}_p} = \begin{bmatrix} u & h & 0 & 0 \\ g & u & 0 & g \\ 0 & 0 & u & 0 \\ 0 & \xi A(3u^2 + v^2) & \xi A(2uv) & 0 \end{bmatrix}. \tag{4.5}$$

The eigenvalues of this system are $\lambda^{(1)} < \lambda^{(2)} < \lambda^{(3)} < \lambda^{(4)}$, and they are the solutions to the characteristic polynomial given by

$$P_1(\lambda, h, u, v) = [\lambda - u] [\lambda^3 - 2u\lambda^2 + [u^2 - \xi Ag(3u^2 + v^2) - gh]\lambda + \xi Ag(3u^3 + uv^2)] = 0. \tag{4.6}$$

Thus, the eigenvalues are given by the velocity in the x -direction u and the factors of the cubic equation

$$\lambda^3 - 2u\lambda^2 + [u^2 - \xi Ag(3u^2 + v^2) - gh]\lambda + \xi Ag(3u^3 + uv^2) = 0,$$

which can be factored using the same method as in [80] and Section 3.1. Similarly to Section 3.2, we find that as the sediment interaction is reduced, the eigenvalues $\lambda^{(1)}$, $\lambda^{(3)}$, and $\lambda^{(4)}$ reduce to the eigenvalues of the 2-D shallow water equations $u - \sqrt{gh}$, u , and $u + \sqrt{gh}$. To estimate the last eigenvalue $\lambda^{(2)}$, we find the approximate value is given by $A(u^3 + v^2)/B$ and is close to zero. Typically, we find $\lambda^{(2)} \ll \max(|\lambda^{(1)}|, |\lambda^{(3)}|, |\lambda^{(4)}|)$. Thus, we conclude that $\lambda^{(1)}$, $\lambda^{(3)}$, and $\lambda^{(4)}$ correspond to the 2-D shallow water equations and $\lambda^{(2)}$ corresponds to the 2-D Exner equation. We make use of this in defining the local speeds of propagation in the x -direction for the numerical scheme as

$$\hat{a}^+ = \max \left\{ \lambda^{(1)+}, \lambda^{(3)+}, \lambda^{(4)+}, \lambda^{(1)-}, \lambda^{(3)-}, \lambda^{(4)-}, 0 \right\}, \quad (4.7)$$

$$\hat{a}^- = \min \left\{ \lambda^{(1)+}, \lambda^{(3)+}, \lambda^{(4)+}, \lambda^{(1)-}, \lambda^{(3)-}, \lambda^{(4)-}, 0 \right\}, \quad (4.8)$$

and

$$\hat{c}^+ = \max \left\{ \lambda^{(2)+}, \lambda^{(2)-}, 0 \right\}, \quad (4.9)$$

$$\hat{c}^- = \min \left\{ \lambda^{(2)+}, \lambda^{(2)-}, 0 \right\}. \quad (4.10)$$

Similarly, the Jacobian in the y -direction is given by

$$\frac{\partial \mathcal{G}_p}{\partial \mathcal{W}_p} = \begin{bmatrix} v & 0 & h & 0 \\ 0 & v & 0 & 0 \\ g & 0 & v & g \\ 0 & \xi A(2uv) & \xi A(3v^2 + u^2) & 0 \end{bmatrix}. \quad (4.11)$$

The eigenvalues of this system are $\mu^{(1)} < \mu^{(2)} < \mu^{(3)} < \mu^{(4)}$, and they are the solutions to the solutions to the characteristic polynomial given by

$$P_2(\mu, h, u, v) = [\lambda - v] [\mu^3 - 2v\mu^2 + [v^2 - \xi Ag(3v^2 + u^2) - gh]\mu + \xi Ag(3v^3 + vu^2)] = 0. \quad (4.12)$$

Thus, the eigenvalues are the velocity in the y -direction v and the factors of the cubic equation

$$\mu^3 - 2v\mu^2 + [v^2 - \xi Ag(3v^2 + u^2) - gh]\mu + \xi Ag(3v^3 + vu^2) = 0,$$

which we can factor using the method in [80] and Section 3.1. Similarly to Section 3.2, we find that as the sediment interaction is reduced, the eigenvalues $\mu^{(1)}$, $\mu^{(3)}$, and $\mu^{(4)}$ reduce to the eigenvalues of the 2-D shallow water equations $v - \sqrt{gh}$, v , and $v + \sqrt{gh}$. To estimate the last eigenvalue $\mu^{(2)}$, we find the approximate value is given by $A(u^2 + v^3)/B$ and is close to zero. Typically, we find $\mu^{(2)} \ll \max(|\mu^{(1)}|, |\mu^{(3)}|, |\mu^{(4)}|)$. Thus, we conclude that $\mu^{(1)}$, $\mu^{(3)}$, and $\mu^{(4)}$ correspond to the 2-D shallow water equations and $\mu^{(2)}$ corresponds to the 2-D Exner equation. We define the local speeds of propagation in the y -direction for the numerical scheme as

$$\hat{b}^+ = \max \left\{ \mu^{(1)+}, \mu^{(3)+}, \mu^{(4)+}, \mu^{(1)-}, \mu^{(3)-}, \mu^{(4)-}, 0 \right\}, \quad (4.13)$$

$$\hat{b}^- = \min \left\{ \mu^{(1)+}, \mu^{(3)+}, \mu^{(4)+}, \mu^{(1)-}, \mu^{(3)-}, \mu^{(4)-}, 0 \right\}, \quad (4.14)$$

and

$$\hat{d}^+ = \max \left\{ \mu^{(2)+}, \mu^{(2)-}, 0 \right\}, \quad (4.15)$$

$$\hat{d}^- = \min \left\{ \mu^{(2)+}, \mu^{(2)-}, 0 \right\}. \quad (4.16)$$

Now that we have the eigenvalues of (4.3) we can construct our numerical scheme.

4.2 A Modified Second-Order Semi-Discrete Central-Upwind Scheme in Two Dimensions

We start by denoting $C_{j,k}$ to be the computational cell $C_{j,k} := [x_{j-\frac{1}{2}}, x_{j+\frac{1}{2}}] \times [y_{k-\frac{1}{2}}, y_{k+\frac{1}{2}}]$, introducing a uniform grid in the x -direction and y -direction with $x_\alpha := \alpha\Delta x$ and $y_\beta := \beta\Delta y$. The cell average of the computed solution,

$$\overline{\mathbf{w}}_{j,k}(t) \approx \frac{1}{\Delta x \Delta y} \iint_{C_{j,k}} \mathbf{w}(x, y, t) dx dy, \quad (4.17)$$

is assumed to be known at a given time t . The cell averages are evolved in time based on the

following equation:

$$\frac{d}{dt} \overline{\mathbf{W}}_{j,k}(t) = - \frac{\mathbf{H}_{j+\frac{1}{2},k}^x(t) - \mathbf{H}_{j-\frac{1}{2},k}^x(t)}{\Delta x} - \frac{\mathbf{H}_{j,k+\frac{1}{2}}^y(t) - \mathbf{H}_{j,k-\frac{1}{2}}^y(t)}{\Delta y} + \overline{\widehat{\mathbf{S}}}_{j,k}(t), \quad (4.18)$$

where $\mathbf{H}_{j\pm\frac{1}{2},k}^x$ and $\mathbf{H}_{j,k\pm\frac{1}{2}}^y$ are the numerical fluxes and

$$\overline{\widehat{\mathbf{S}}}_{j,k}(t) \approx \frac{1}{\Delta x \Delta y} \iint_{C_{j,k}} \widehat{\mathbf{S}}(\mathbf{w}) dx dy, \quad (4.19)$$

are the cell averages of the source term. For the rest of this chapter, we will drop the notation t for time dependence, for simplicity, where it is appropriate.

The construction of the numerical scheme will be complete once the numerical fluxes $\mathbf{H}_{j\pm\frac{1}{2},k}^x$, and $\mathbf{H}_{j,k\pm\frac{1}{2}}^y$ in (4.20) and the source term $\overline{\widehat{\mathbf{S}}}_{j,k}$ in (4.19) are computed such that the resulting scheme is well-balanced.

4.2.1 Numerical Fluxes

In (4.18), we use the central-upwind numerical fluxes from [50], modifying the local speeds of propagation to $\widehat{a}^\pm, \widehat{c}^\pm, \widehat{b}^\pm$, and \widehat{d}^\pm using (4.7)-(4.10) and (4.13)-(4.16) where appropriate to capture the different speed of water and sediment waves. These numerical fluxes are given by

$$\begin{aligned} H_{j+\frac{1}{2},k}^{x(1)}(t) &= \frac{\widehat{a}_{j+\frac{1}{2},k}^+ \mathcal{F}^{(1)}(\mathbf{W}_{j+\frac{1}{2},k}^-) - \widehat{a}_{j+\frac{1}{2},k}^- \mathcal{F}^{(1)}(\mathbf{W}_{j+\frac{1}{2},k}^+)}{\widehat{a}_{j+\frac{1}{2},k}^+ - \widehat{a}_{j+\frac{1}{2},k}^-} \\ &\quad + \frac{\widehat{a}_{j+\frac{1}{2},k}^+ \widehat{a}_{j+\frac{1}{2},k}^-}{\widehat{a}_{j+\frac{1}{2},k}^+ - \widehat{a}_{j+\frac{1}{2},k}^-} \left[w_{j+\frac{1}{2},k}^+ - w_{j+\frac{1}{2},k}^- \right], \\ H_{j+\frac{1}{2},k}^{x(2)}(t) &= \frac{\widehat{a}_{j+\frac{1}{2},k}^+ \mathcal{F}^{(2)}(\mathbf{W}_{j+\frac{1}{2},k}^-) - \widehat{a}_{j+\frac{1}{2},k}^- \mathcal{F}^{(2)}(\mathbf{W}_{j+\frac{1}{2},k}^+)}{\widehat{a}_{j+\frac{1}{2},k}^+ - \widehat{a}_{j+\frac{1}{2},k}^-} \\ &\quad + \frac{\widehat{a}_{j+\frac{1}{2},k}^+ \widehat{a}_{j+\frac{1}{2},k}^-}{\widehat{a}_{j+\frac{1}{2},k}^+ - \widehat{a}_{j+\frac{1}{2},k}^-} \left[q_{j+\frac{1}{2},k}^+ - q_{j+\frac{1}{2},k}^- \right], \end{aligned}$$

$$H_{j+\frac{1}{2},k}^{x(3)}(t) = \frac{\widehat{a}_{j+\frac{1}{2},k}^+ \mathcal{F}^{(3)}(\mathbf{W}_{j+\frac{1}{2},k}^-) - \widehat{a}_{j+\frac{1}{2},k}^- \mathcal{F}^{(3)}(\mathbf{W}_{j+\frac{1}{2},k}^+)}{\widehat{a}_{j+\frac{1}{2}}^+ - \widehat{a}_{j+\frac{1}{2},k}^-}$$

$$+ \frac{\widehat{a}_{j+\frac{1}{2},k}^+ \widehat{a}_{j+\frac{1}{2},k}^-}{\widehat{a}_{j+\frac{1}{2},k}^+ - \widehat{a}_{j+\frac{1}{2},k}^-} \left[p_{j+\frac{1}{2},k}^+ - p_{j+\frac{1}{2},k}^- \right],$$

$$H_{j+\frac{1}{2},k}^{x(4)}(t) = \frac{\widehat{c}_{j+\frac{1}{2},k}^+ \mathcal{F}^{(4)}(\mathbf{W}_{j+\frac{1}{2},k}^-) - \widehat{c}_{j+\frac{1}{2},k}^- \mathcal{F}^{(4)}(\mathbf{W}_{j+\frac{1}{2},k}^+)}{\widehat{c}_{j+\frac{1}{2},k}^+ - \widehat{c}_{j+\frac{1}{2},k}^-}$$

$$+ \frac{\widehat{c}_{j+\frac{1}{2},k}^+ \widehat{c}_{j+\frac{1}{2},k}^-}{\widehat{c}_{j+\frac{1}{2},k}^+ - \widehat{c}_{j+\frac{1}{2},k}^-} \left[B_{j+\frac{1}{2},k}^+ - B_{j+\frac{1}{2},k}^- \right],$$

$$H_{j,k+\frac{1}{2}}^{y(1)}(t) = \frac{\widehat{b}_{j,k+\frac{1}{2}}^+ \mathcal{G}^{(1)}(\mathbf{W}_{j,k+\frac{1}{2}}^-) - \widehat{b}_{j,k+\frac{1}{2}}^- \mathcal{G}^{(1)}(\mathbf{W}_{j,k+\frac{1}{2}}^+)}{\widehat{b}_{j,k+\frac{1}{2}}^+ - \widehat{b}_{j,k+\frac{1}{2}}^-}$$

$$+ \frac{\widehat{b}_{j,k+\frac{1}{2}}^+ \widehat{b}_{j,k+\frac{1}{2}}^-}{\widehat{b}_{j,k+\frac{1}{2}}^+ - \widehat{b}_{j,k+\frac{1}{2}}^-} \left[w_{j,k+\frac{1}{2}}^+ - w_{j,k+\frac{1}{2}}^- \right],$$

$$H_{j,k+\frac{1}{2}}^{y(2)}(t) = \frac{\widehat{b}_{j,k+\frac{1}{2}}^+ \mathcal{G}^{(2)}(\mathbf{W}_{j,k+\frac{1}{2}}^-) - \widehat{b}_{j,k+\frac{1}{2}}^- \mathcal{G}^{(2)}(\mathbf{W}_{j,k+\frac{1}{2}}^+)}{\widehat{b}_{j,k+\frac{1}{2}}^+ - \widehat{b}_{j,k+\frac{1}{2}}^-}$$

$$+ \frac{\widehat{b}_{j,k+\frac{1}{2}}^+ \widehat{b}_{j,k+\frac{1}{2}}^-}{\widehat{b}_{j,k+\frac{1}{2}}^+ - \widehat{b}_{j,k+\frac{1}{2}}^-} \left[q_{j,k+\frac{1}{2}}^+ - q_{j,k+\frac{1}{2}}^- \right],$$

$$H_{j,k+\frac{1}{2}}^{y(3)}(t) = \frac{\widehat{b}_{j,k+\frac{1}{2}}^+ \mathcal{G}^{(3)}(\mathbf{W}_{j,k+\frac{1}{2}}^-) - \widehat{b}_{j,k+\frac{1}{2}}^- \mathcal{G}^{(3)}(\mathbf{W}_{j,k+\frac{1}{2}}^+)}{\widehat{b}_{j,k+\frac{1}{2}}^+ - \widehat{b}_{j,k+\frac{1}{2}}^-}$$

$$+ \frac{\widehat{b}_{j,k+\frac{1}{2}}^+ \widehat{b}_{j,k+\frac{1}{2}}^-}{\widehat{b}_{j,k+\frac{1}{2}}^+ - \widehat{b}_{j,k+\frac{1}{2}}^-} \left[p_{j,k+\frac{1}{2}}^+ - p_{j,k+\frac{1}{2}}^- \right],$$

$$\begin{aligned}
H_{j,k+\frac{1}{2}}^{y(4)}(t) &= \frac{\widehat{d}_{j,k+\frac{1}{2}}^+ \mathcal{G}^{(4)}(\mathbf{w}_{j,k+\frac{1}{2}}^-) - \widehat{d}_{j,k+\frac{1}{2}}^- \mathcal{G}^{(4)}(\mathbf{w}_{j,k+\frac{1}{2}}^+)}{\widehat{d}_{j,k+\frac{1}{2}}^+ - \widehat{d}_{j,k+\frac{1}{2}}^-} \\
&\quad + \frac{\widehat{d}_{j,k+\frac{1}{2}}^+ \widehat{d}_{j,k+\frac{1}{2}}^-}{\widehat{d}_{j,k+\frac{1}{2}}^+ - \widehat{d}_{j,k+\frac{1}{2}}^-} \left[B_{j,k+\frac{1}{2}}^+ - B_{j,k+\frac{1}{2}}^- \right].
\end{aligned} \tag{4.20}$$

4.2.2 Reconstruction

In (4.20), \mathbf{w}^\pm are the left and right point values of the piecewise bilinear reconstruction

$$\widetilde{\mathbf{w}}(x, y) = \sum_{j,k} [\overline{\mathbf{w}}_{j,k} + (\mathbf{w}_x)_{j,k}(x - x_j) + (\mathbf{w}_y)_{j,k}(y - y_k)] \cdot \chi_{C_{j,k}}(x, y), \tag{4.21}$$

obtained at the midpoint cell interfaces $(x_{j\pm\frac{1}{2}}, y_k)$ and $(x_j, y_{k\pm\frac{1}{2}})$ by

$$\begin{aligned}
\mathbf{w}_{j+\frac{1}{2},k}^+ &= \overline{\mathbf{w}}_{j+1,k} - \frac{\Delta x}{2} (\mathbf{w}_x)_{j+1,k}, & \mathbf{w}_{j+\frac{1}{2},k}^- &= \overline{\mathbf{w}}_{j,k} + \frac{\Delta x}{2} (\mathbf{w}_x)_{j,k}, \\
\mathbf{w}_{j,k+\frac{1}{2}}^+ &= \overline{\mathbf{w}}_{j,k+1} - \frac{\Delta y}{2} (\mathbf{w}_y)_{j,k+1}, & \mathbf{w}_{j,k+\frac{1}{2}}^- &= \overline{\mathbf{w}}_{j,k} + \frac{\Delta y}{2} (\mathbf{w}_y)_{j,k}.
\end{aligned} \tag{4.22}$$

In (4.21) and (4.22), $\chi_{C_{j,k}}(x, y)$, is the characteristic function of the interval $C_{j,k}$, and $(\mathbf{w}_x)_{j,k}$ and $(\mathbf{w}_y)_{j,k}$ are the numerical derivatives in the x -direction and y -direction, respectively, which should be computed using a nonlinear limiter in order to reduce oscillations. In our numerical experiments, we use the generalized minmod limiter (see, e.g., [63, 68, 82, 85]):

$$(\mathbf{w}_x)_{j,k} = \text{minmod} \left(\theta \frac{\overline{\mathbf{w}}_{j,k} - \overline{\mathbf{w}}_{j-1,k}}{\Delta x}, \frac{\overline{\mathbf{w}}_{j+1,k} - \overline{\mathbf{w}}_{j-1,k}}{2\Delta x}, \theta \frac{\overline{\mathbf{w}}_{j+1,k} - \overline{\mathbf{w}}_{j,k}}{\Delta x} \right), \quad \theta \in [1, 2], \tag{4.23}$$

$$(\mathbf{w}_y)_{j,k} = \text{minmod} \left(\theta \frac{\overline{\mathbf{w}}_{j,k} - \overline{\mathbf{w}}_{j,k-1}}{\Delta y}, \frac{\overline{\mathbf{w}}_{j,k+1} - \overline{\mathbf{w}}_{j,k-1}}{2\Delta y}, \theta \frac{\overline{\mathbf{w}}_{j,k+1} - \overline{\mathbf{w}}_{j,k}}{\Delta y} \right), \quad \theta \in [1, 2], \tag{4.24}$$

where the minmod function is defined by

$$\text{minmod}(z_{1,1}, \dots, z_{j,k}) := \begin{cases} \min_{j,k} \{z_{j,k}\}, & \text{if } z_{j,k} > 0 \quad \forall j, k, \\ \max_{j,k} \{z_{j,k}\}, & \text{if } z_{j,k} < 0 \quad \forall j, k, \\ 0, & \text{otherwise.} \end{cases} \tag{4.25}$$

The parameter θ in (4.23) and (4.24) is used to control the amount of numerical viscosity with large θ values resulting in less dissipative results.

4.2.3 Well-Balanced Quadrature for the Geometric Source Terms

In order to ensure the scheme is well-balanced, a special quadrature should be used to discretize the second and third components, $\bar{S}_j^{(2)}$ and $\bar{S}_j^{(3)}$, of the source term in (4.19) such that it balances with the numerical fluxes in the lake-at-rest steady state. The fluxes at the discrete level are given by

$$\frac{H_{j-\frac{1}{2},k}^{x(2)} - H_{j+\frac{1}{2},k}^{x(2)}}{\Delta x} + \frac{H_{j-\frac{1}{2},k}^{y(2)} - H_{j+\frac{1}{2},k}^{y(2)}}{\Delta y} = \frac{g\bar{w}_{j,k}}{\Delta x} \left(\frac{\hat{a}_{j+\frac{1}{2},k}^+ B_{j+\frac{1}{2},k}^- - \hat{a}_{j+\frac{1}{2},k}^- B_{j+\frac{1}{2},k}^+}{\hat{a}_{j+\frac{1}{2},k}^+ - \hat{a}_{j+\frac{1}{2},k}^-} - \frac{\hat{a}_{j-\frac{1}{2},k}^+ B_{j-\frac{1}{2},k}^- - \hat{a}_{j-\frac{1}{2},k}^- B_{j-\frac{1}{2},k}^+}{\hat{a}_{j-\frac{1}{2},k}^+ - \hat{a}_{j-\frac{1}{2},k}^-} \right),$$

$$\frac{H_{j,k-\frac{1}{2}}^{x(3)} - H_{j,k+\frac{1}{2}}^{x(3)}}{\Delta x} + \frac{H_{j,k-\frac{1}{2}}^{y(3)} - H_{j,k+\frac{1}{2}}^{y(3)}}{\Delta y} = \frac{g\bar{w}_{j,k}}{\Delta x} \left(\frac{\hat{b}_{j,k+\frac{1}{2}}^+ B_{j,k+\frac{1}{2}}^- - \hat{b}_{j,k+\frac{1}{2}}^- B_{j,k+\frac{1}{2}}^+}{\hat{b}_{j,k+\frac{1}{2}}^+ - \hat{b}_{j,k+\frac{1}{2}}^-} - \frac{\hat{b}_{j,k-\frac{1}{2}}^+ B_{j,k-\frac{1}{2}}^- - \hat{b}_{j,k-\frac{1}{2}}^- B_{j,k-\frac{1}{2}}^+}{\hat{b}_{j,k-\frac{1}{2}}^+ - \hat{b}_{j,k-\frac{1}{2}}^-} \right).$$

Therefore, the fluxes and source term will balance if the second and third component of the source term are discretized as follows:

$$\bar{S}_{j,k}^{(2)} \approx -\frac{g\bar{w}_{j,k}}{\Delta x} \left(\frac{\hat{a}_{j+\frac{1}{2},k}^+ B_{j+\frac{1}{2},k}^- - \hat{a}_{j+\frac{1}{2},k}^- B_{j+\frac{1}{2},k}^+}{\hat{a}_{j+\frac{1}{2},k}^+ - \hat{a}_{j+\frac{1}{2},k}^-} - \frac{\hat{a}_{j-\frac{1}{2},k}^+ B_{j-\frac{1}{2},k}^- - \hat{a}_{j-\frac{1}{2},k}^- B_{j-\frac{1}{2},k}^+}{\hat{a}_{j-\frac{1}{2},k}^+ - \hat{a}_{j-\frac{1}{2},k}^-} \right), \quad (4.26)$$

$$\bar{S}_{j,k}^{(3)} \approx -\frac{g\bar{w}_{j,k}}{\Delta y} \left(\frac{\hat{b}_{j,k+\frac{1}{2}}^+ B_{j,k+\frac{1}{2}}^- - \hat{b}_{j,k+\frac{1}{2}}^- B_{j,k+\frac{1}{2}}^+}{\hat{b}_{j,k+\frac{1}{2}}^+ - \hat{b}_{j,k+\frac{1}{2}}^-} - \frac{\hat{b}_{j,k-\frac{1}{2}}^+ B_{j,k-\frac{1}{2}}^- - \hat{b}_{j,k-\frac{1}{2}}^- B_{j,k-\frac{1}{2}}^+}{\hat{b}_{j,k-\frac{1}{2}}^+ - \hat{b}_{j,k-\frac{1}{2}}^-} \right). \quad (4.27)$$

4.2.4 Local Speeds of Propagation

The local speeds of propagation for the water waves and the sediment waves are obtained using the eigenvalues corresponding to the 2-D shallow water and 2-D Exner equations given by

$$\begin{aligned}
\hat{a}_{j+\frac{1}{2},k}^+ &= \max \left\{ \lambda_{j+\frac{1}{2},k}^{(1)+}, \lambda_{j+\frac{1}{2},k}^{(3)+}, \lambda_{j+\frac{1}{2},k}^{(4)+}, \lambda_{j+\frac{1}{2},k}^{(1)-}, \lambda_{j+\frac{1}{2},k}^{(3)-}, \lambda_{j+\frac{1}{2},k}^{(4)+}, 0 \right\}, \\
\hat{a}_{j+\frac{1}{2},k}^- &= \min \left\{ \lambda_{j+\frac{1}{2},k}^{(1)+}, \lambda_{j+\frac{1}{2},k}^{(3)+}, \lambda_{j+\frac{1}{2},k}^{(4)+}, \lambda_{j+\frac{1}{2},k}^{(1)-}, \lambda_{j+\frac{1}{2},k}^{(3)-}, \lambda_{j+\frac{1}{2},k}^{(4)-}, 0 \right\}, \\
\hat{b}_{j,k+\frac{1}{2}}^+ &= \max \left\{ \mu_{j,k+\frac{1}{2}}^{(1)+}, \mu_{j,k+\frac{1}{2}}^{(3)+}, \mu_{j,k+\frac{1}{2}}^{(4)+}, \mu_{j,k+\frac{1}{2}}^{(1)-}, \mu_{j,k+\frac{1}{2}}^{(3)-}, \mu_{j,k+\frac{1}{2}}^{(4)+}, 0 \right\}, \\
\hat{b}_{j,k+\frac{1}{2}}^- &= \min \left\{ \mu_{j,k+\frac{1}{2}}^{(1)+}, \mu_{j,k+\frac{1}{2}}^{(3)+}, \mu_{j,k+\frac{1}{2}}^{(4)+}, \mu_{j,k+\frac{1}{2}}^{(1)-}, \mu_{j,k+\frac{1}{2}}^{(3)-}, \mu_{j,k+\frac{1}{2}}^{(4)-}, 0 \right\}, \\
\hat{c}_{j+\frac{1}{2},k}^+ &= \max \left\{ \lambda_{j+\frac{1}{2},k}^{(2)+}, \lambda_{j+\frac{1}{2},k}^{(2)-}, 0 \right\}, \\
\hat{c}_{j+\frac{1}{2},k}^- &= \min \left\{ \lambda_{j+\frac{1}{2},k}^{(2)+}, \lambda_{j+\frac{1}{2},k}^{(2)-}, 0 \right\}, \\
\hat{d}_{j,k+\frac{1}{2}}^+ &= \max \left\{ \mu_{j,k+\frac{1}{2}}^{(2)+}, \mu_{j,k+\frac{1}{2}}^{(2)-}, 0 \right\}, \\
\hat{d}_{j,k+\frac{1}{2}}^- &= \min \left\{ \mu_{j,k+\frac{1}{2}}^{(2)+}, \mu_{j,k+\frac{1}{2}}^{(2)-}, 0 \right\}.
\end{aligned} \tag{4.28}$$

4.2.5 Time Evolution

To find the time step, we compare all of the local speeds of propagation for the water and sediment constrained by the CFL condition, resulting in,

$$\Delta t \leq 0.25 \min \left\{ \frac{\Delta x}{\max_{j,k} |\hat{c}_{j\pm\frac{1}{2},k}^\pm|}, \frac{\Delta x}{\max_{j,k} |\hat{a}_{j\pm\frac{1}{2},k}^\pm|}, \frac{\Delta y}{\max_{j,k} |\hat{b}_{j,k\pm\frac{1}{2}}^\pm|}, \frac{\Delta y}{\max_{j,k} |\hat{d}_{j,k\pm\frac{1}{2}}^\pm|} \right\}. \tag{4.29}$$

4.3 Numerical Example in 2-D – Evolution of Conical Sediment Dune Interacting Slowly with the Water Flow

In this section, we discuss a conical sand dune test problem discussed by [86]. The solution is evolved in time using a third order Strong Stability Preserving Runge Kutta (SSP-RK3) ODE solver from [29] as well as an adaptive time step strategy from [14], which are outlined in Appendix A and Appendix B, respectively. The solutions are computed using the minmod limiter with $\theta = 1.3$, $\xi = 5/3$, $A = .001$, $g = 9.8$, $\kappa = 0.9$ in the adaptive time evolution. We take $m = 3$ from Grass's Model (3.4), and N represents the number of computational cells the domain is broken into. We assume free flow boundary conditions on all sides of the domain.

This example consists of evolving a conical dune where the computational domain is $[0, 1000] \times [0, 1000]$, the initial data are

$$w(x, y, 0) = 10, \quad hu(x, y, 0) = 10, \quad hv(x, y, 0) = 0,$$

and the bottom topography is given by

$$B(x, y, 0) = \begin{cases} \sin^2\left(\frac{\pi(x-300)}{200}\right) \sin^2\left(\frac{\pi(y-400)}{200}\right), & 300 \leq x \leq 500, 400 \leq y \leq 600, \\ 0, & \text{otherwise.} \end{cases}$$

DeVriend in [86] derived an approximate solution for the angle of spread for a small conical dune in a river bed interacting slowly with the water flow ($A < 0.01$). He states that as time is evolved the conical dune will spread out gradually into a star shaped pattern, approximating the angle of the spread for the dune as $\alpha \approx 21.79$ degrees from the line of symmetry. This can be seen in Figure 4.1.

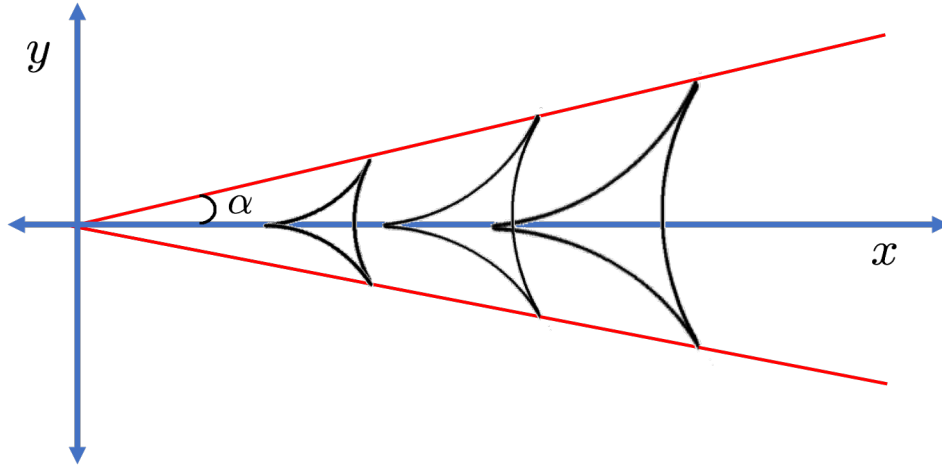


Figure 4.1: Example 1: Approximate solution for the angle of spread.

In Figure 4.2 and 4.3, we plot the initial condition (left) as well as the computed solution at $t = 360000$ (right). As one can see, our computed solution for the bottom is propagating to the right and expanding into a star shape as is expected. In Figure 4.4, we plot a level curve at the base of the dune at time $t = 0$, $t = 90000$, $t = 180000$, $t = 270000$, and $t = 360000$, as well as the approximate solution where the angle between the dashed lines is given by 21.79 degrees. The spread of the bottom exhibited in the computed solution, seen in Figure 4.4, extends past the

desired angle of spread marked by the approximate solution, but it is largely contained within them. This demonstrates that the solution is propagating and forming into a star pattern. We found the computed results for the bottom to be similar to the results reported in [24, 36].

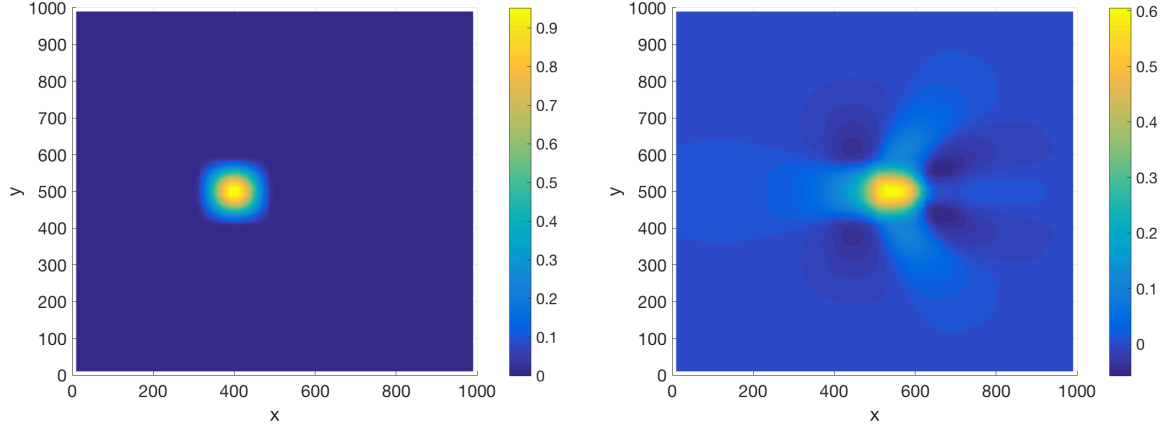


Figure 4.2: Example 1: Solution (B) computed at $t = 0$ (left) and $t = 360000$ (right) with $\Delta x = 50$ and $\Delta y = 50$.

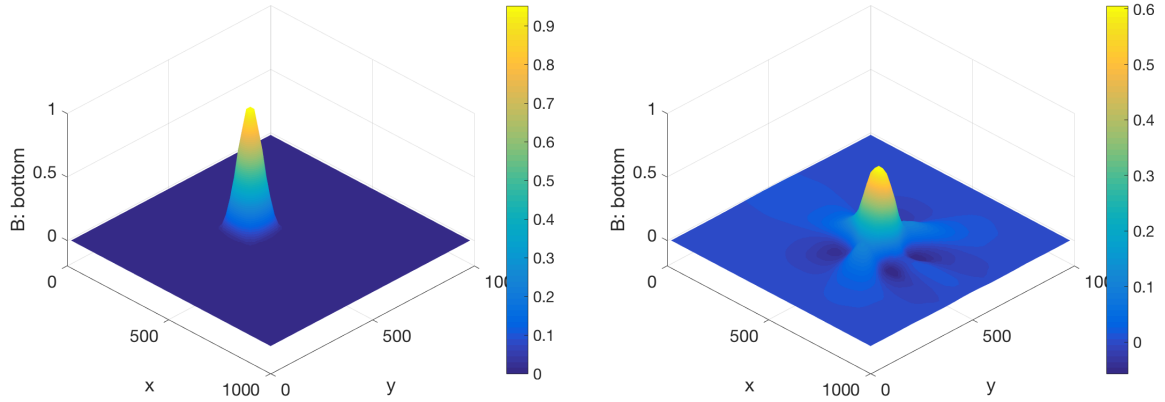


Figure 4.3: Example 1: Solution (B) computed at $t = 0$ (left) and $t = 360000$ (right) with $\Delta x = 50$ and $\Delta y = 50$.

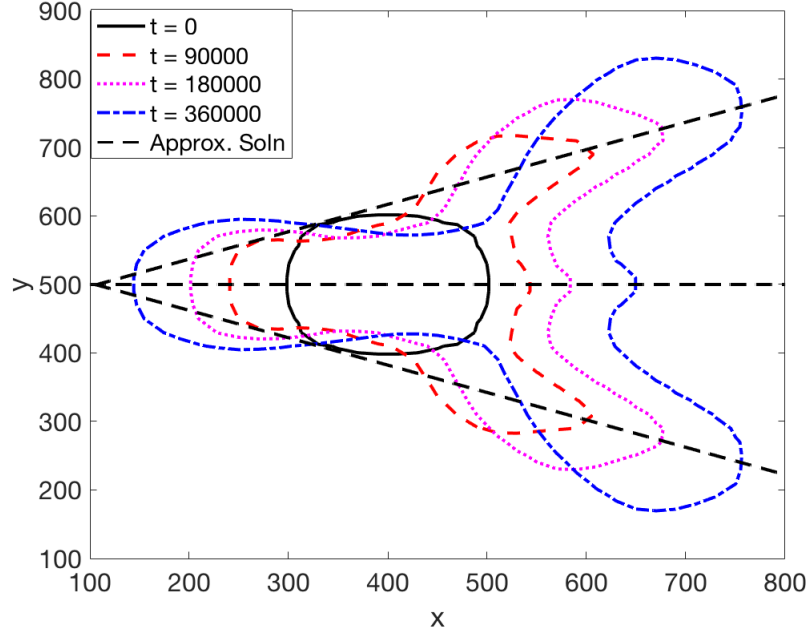


Figure 4.4: Example 1: Evolution of Conical Dune (B) at $t = 0$, $t = 90000$, $t = 180000$, $t = 360000$ and approximate spread angle with $\Delta x = 50$ and $\Delta y = 50$.

4.4 Conclusion

In this chapter, we extended our non-staggered non-splitting scheme into two dimensions, implementing a second order central-upwind scheme, which is well-balanced when applied to the 2-D shallow water equations with 2-D Exner equation to govern sediment transport. We successfully determined the eigenvalues for the complete 2-D system in (4.3) and determined to which equations of the system they corresponded. We then incorporated them as the local speeds of propagation for the respective water and sediment waves to obtain better results than the straightforward implementation of the central-upwind scheme, which only uses the largest and smallest eigenvalues of the complete system. In Section 4.3, we presented a numerical result for the propagation of a small conical dune in two dimensions, demonstrating the numerical scheme described in this chapter produced a smooth, star-like pattern, which propagated to the right, largely within the angle of spread.

Chapter 5

Conclusions and Future Work

Throughout this thesis we have discussed a variety of numerical schemes for approximating the shallow water equations with Exner equation to govern sediment transport in one and two dimensions. In Chapter 1, the shallow water equations and Exner equations were derived from physical principles, and six different formulations for computing the sediment transport fluxes were discussed.

In Chapter 2, we implemented a second-order well-balanced positivity preserving central-upwind scheme for the 1-D shallow water equations with discontinuous bottom topography. The central-upwind scheme presented relied on a discontinuous piecewise linear reconstruction of the bottom topography function B , and thus it is suitable for functions B containing large jumps and can be extended to models with moving, time-dependent bottom topography function B . We presented three numerical results for the numerical scheme in Chapter 2, demonstrating that the numerical scheme remains smooth while handling a small perturbation of steady state and accurately converge to the solution of a Riemann problem when there is a unique solution and when multiple solutions are present.

In Chapter 3, we implemented four second order central-upwind schemes, which are well-balanced when applied to the 1-D shallow water equations with Exner equation to govern sediment transport. We were successful in determining the eigenvalues for our complete system and to which part of the system they corresponded. We then incorporated the eigenvalues as the local speeds of propagation for the respective water and sediment waves to obtain better results than the straightforward implementation of the central-upwind scheme, which only uses the largest and smallest eigenvalues of the complete system. We compared the four numerical schemes to each other, obtaining similar results for each of the schemes. We then demonstrated the NS-NSG numerical scheme on a number of numerical examples showing the scheme is second orders and can numerically handle when the sediment interaction is large with a fast water flow and when the sediment interaction is small and the water flow is fast or slow. Finally, we

demonstrated that the NS-SNG numerical scheme was capable of propagating a discontinuity to the correct location, indicating proper numerical handling of the discontinuity and usefulness in capturing shocks.

In Chapter 4, we extended our non-staggered non-splitting scheme into two dimensions. Implementing a second order central-upwind scheme, which is well-balanced when applied to the 2-D shallow water equations with 2-D Exner equation to govern sediment transport. We successfully determined the eigenvalues for the complete 2-D system given in (4.3), and we determined to which equations of the system they corresponded, incorporating them as the local speeds of propagation for the water and sediment waves to obtain better results than the straightforward implementation of the central upwind scheme. We then presented a numerical result for the propagation of a small conical dune in two dimensions, demonstrating the numerical scheme described in Chapter 4 produced a smooth, star-like pattern, which propagated to the right, largely within the angle of spread.

In future work, we intend to modify the numerical schemes in Chapter 3 and Chapter 4 to implement different sediment transport fluxes beyond those discussed by Grass [30]. In addition, we intend to investigate the dry bed case, where the water height is initially zero, which poses numerical difficulties in constructing the numerical schemes to be positivity preserving.

REFERENCES

- [1] R. Abgrall. On essentially non-oscillatory schemes on unstructured meshes: analysis and implementation. *J. Comput. Phys.*, 114:45–58, 1994.
- [2] P. Arminjon, M.C. Viallon, and A. Madrane. A finite volume extension of the Lax-Friedrichs and Nessyahu-Tadmor schemes for conservation laws on unstructured grids. *Int. J. Comput. Fluid Dyn.*, 9:1–22, 1997.
- [3] E. Audusse, F. Bouchut, M.-O. Bristeau, R. Klein, and B. Perthame. A fast and stable well-balanced scheme with hydrostatic reconstruction for shallow water flows. *SIAM J. Sci. Comput.*, 25:2050–2065, 2004.
- [4] M. Ben-Artzi and J. Falcovitz. *Generalized Riemann problems in computational fluid dynamics*, volume 11 of *Cambridge Monographs on Applied and Computational Mathematics*. Cambridge University Press, Cambridge, 2003.
- [5] Andrew Bernstein, Alina Chertock, and Alexander Kurganov. Central-upwind scheme for shallow water equations with discontinuous bottom topography. *Bulletin of the Brazilian Mathematical Society, New Series*, 47(1):91–103, 2016.
- [6] F. Bianco, G. Puppo, and G. Russo. High order central schemes for hyperbolic systems of conservation laws. *SIAM J. Sci. Comput.*, 21:294–322, 1999.
- [7] A. Bollermann, G. Chen, A. Kurganov, and S. Noelle. A well-balanced reconstruction of wet/dry fronts for the shallow water equations. *J. Sci. Comput.*, 56(2):267–290, 2013.
- [8] A. Bollermann, S. Noelle, and M. Lukáčová-Medvidová. Finite volume evolution Galerkin methods for the shallow water equations with dry beds. *Commun. Comput. Phys.*, 10(2):371–404, 2011.

- [9] F. Bouchut. *Nonlinear stability of finite volume methods for hyperbolic conservation laws and well-balanced schemes for sources*. Frontiers in Mathematics. Birkhäuser Verlag, Basel, 2004.
- [10] R. Briganti, N. Dodd, D. Kelly, and D. Pokrajac. An efficient and flexible solver for the simulation of the morphodynamics of fast evolving flows on coarse sediment beaches. *Internat. J. Numer. Meth. Fluids*, 69(859-877), 2012.
- [11] S. Bryson, Y. Epshteyn, A. Kurganov, and G. Petrova. Well-balanced positivity preserving central-upwind scheme on triangular grids for the Saint-Venant system. *M2AN Math. Model. Numer. Anal.*, 45(3):423–446, 2011.
- [12] S. Bryson, A. Kurganov, D. Levy, and G. Petrova. Semi-discrete central-upwind schemes with reduced dissipation for Hamilton-Jacobi equations. *IMA J. Numer. Anal.*, 25:113–138, 2005.
- [13] S. Bryson and D. Levy. High-order semi-discrete central-upwind schemes for multi-dimensional Hamilton-Jacobi equations. *J. Comput. Phys.*, 189(1):63–87, 2003.
- [14] A. Chertock, S. Cui, A. Kurganov, and T. Wu. Well-balanced positivity preserving central-upwind scheme for the shallow water system with friction terms. *Internat. J. Numer. Meth. Fluids*, 2015.
- [15] I. Christov and B. Popov. New nonoscillatory central schemes on unstructured triangulations for hyperbolic systems of conservation laws. *J. Comput. Phys.*, 227:5736–5757, 2008.
- [16] B. Cockburn, C. Johnson, C.-W. Shu, and E. Tadmor. Advanced numerical approximation of nonlinear hyperbolic equations. In A. Quarteroni, editor, *CIME Lecture Notes*, volume 1697 of *Lecture Notes in Mathematics*. Springer-Verlag, 1998.

- [17] L. A. Constantin and A. Kurganov. Adaptive central-upwind schemes for hyperbolic systems of conservation laws. In *Hyperbolic problems: theory, numerics and applications. I*, pages 95–103. Yokohama Publ., Yokohama, 2006.
- [18] S. Cordier, M.H. Le, and T. Morales de Luna. Bedload transport in shallow water models: Why splitting (may) fail and how hyperbolicity (can) help. *Advances in Water Resources*, 34(8):980–989, August 2011.
- [19] J.A. Cunge, F.M. Holly, and A. Verwey. *Practical Aspects of Computational River Hydraulics*. Pitman, 1980.
- [20] A. J. C. de Saint-Venant. Théorie du mouvement non-permanent des eaux, avec application aux crues des rivières et à l’introduction des marées dans leur lit. *C.R. Acad. Sci. Paris*, 73:147–154, 1871.
- [21] M.J. Castro Diaz, E.D. Fernandez-Nieto, and A.M. Ferreiro. Sediment transport models in shallow water equations and numerical approach by high order finite volume methods. *Computers and Fluids*, 37:299–316, 2008.
- [22] MJ Castro Diaz, Enrique D Fernández-Nieto, AM Ferreiro, and C Parés. Two-dimensional sediment transport models in shallow water equations. A second order finite volume approach on unstructured meshes. *Computer Methods in Applied Mechanics and Engineering*, 198(33):2520–2538, 2009.
- [23] Felix M Exner. *Zur physik der dünen*. Hölder, 1920.
- [24] M. Seaid F. Benkhaldoun, S. Sahmim. A two-dimensional finite volume morphodynamic model on unstructured grids. *Internat. J. Numer. Methods Fluids*, 63:1296–1327, 2010.
- [25] K. O. Friedrichs. Symmetric hyperbolic linear differential equations. *Comm. Pure Appl. Math.*, 7:345–392, 1954.

- [26] J. M. Gallardo, C. Parés, and M. Castro. On a well-balanced high-order finite volume scheme for shallow water equations with topography and dry areas. *J. Comput. Phys.*, 227(1):574–601, 2007.
- [27] E. Godlewski and P. A. Raviart. *Numerical approximation of hyperbolic systems of conservation laws*, volume 118 of *Applied Mathematical Sciences*. Springer-Verlag, New York, 1996.
- [28] S. K. Godunov. A difference method for numerical calculation of discontinuous solutions of the equations of hydrodynamics. *Mat. Sb. (N.S.)*, 47 (89):271–306, 1959.
- [29] S. Gottlieb, D. Ketcheson, and C. W. Shu. *Strong stability preserving Runge-Kutta and multistep time discretizations*. World Scientific Publishing Co. Pte. Ltd., Hackensack, NJ, 2011.
- [30] A. J. Grass. *Sediment transport by waves and currents*. University College, London, Dept. of Civil Engineering, 1981.
- [31] J. M. Greenberg and A. Y. Leroux. A well-balanced scheme for the numerical processing of source terms in hyperbolic equations. *SIAM J. Numer. Anal.*, 33(1):1–16, 1996.
- [32] S. Harig, S. Pranowo, and J. Behrens. Tsunami simulations on several scales: Comparison of approaches with unstructured meshes and nested grids. *Ocean Dynamics*, 58(5):429–440, 2008.
- [33] A. Harten, B. Engquist, S. Osher, and S. R. Chakravarthy. Uniformly high-order accurate essentially nonoscillatory schemes. III. *J. Comput. Phys.*, 71(2):231–303, 1987.
- [34] A. Harten and S. Osher. Uniformly high-order accurate nonoscillatory schemes. I. *SIAM J. Numer. Anal.*, 24(2):279–309, 1987.
- [35] Peng Hu, Wei Li, Zhiguo He, Thomas Pähtz, and Zhiyuan Yue. Well-balanced and flexible morphological modeling of swash hydrodynamics and sediment transport. *Coastal Engineering*, 96(27-37), 2015.

- [36] Justin Hudson. *Numerical techniques for morphodynamic modelling*. PhD thesis, University of Reading, 2001.
- [37] Justin Hudson and Peter K Sweby. Formulations for numerically approximating hyperbolic systems governing sediment transport. *Journal of Scientific Computing*, 19(1-3):225–252, 2003.
- [38] G. S Jiang and C. W. Shu. Efficient implementation of weighted ENO schemes. *J. Comput. Phys.*, 126(1):202–228, 1996.
- [39] G. S. Jiang and E. Tadmor. Nonoscillatory central schemes for multidimensional hyperbolic conservation laws. *SIAM J. Sci. Comput.*, 19(6):1892–1917 (electronic), 1998.
- [40] S. Jin. A steady-state capturing method for hyperbolic systems with geometrical source terms. *M2AN Math. Model. Numer. Anal.*, 35(4):631–645, 2001.
- [41] S. Jin and X. Wen. Two interface-type numerical methods for computing hyperbolic systems with geometrical source terms having concentrations. *SIAM J. Sci. Comput.*, 26(6):2079–2101, 2005.
- [42] D. Kröner. *Numerical schemes for conservation laws*. Wiley-Teubner Series Advances in Numerical Mathematics. John Wiley & Sons Ltd., Chichester, 1997.
- [43] A. Kurganov and D. Levy. Third-order semi-discrete central scheme for conservation laws and convection-diffusion equations. *SIAM J. Sci. Comput.*, 22:1461–1488, 2000.
- [44] A. Kurganov and C. T. Lin. On the reduction of numerical dissipation in central-upwind schemes. *Commun. Comput. Phys.*, 2:141–163, 2007.
- [45] A. Kurganov, S. Noelle, and G. Petrova. Semi-discrete central-upwind scheme for hyperbolic conservation laws and Hamilton-Jacobi equations. *SIAM J. Sci. Comput.*, 23:707–740, 2001.

- [46] A. Kurganov and G. Petrova. Central schemes and contact discontinuities. *M2AN Math. Model. Numer. Anal.*, 34(6):1259–1275, 2000.
- [47] A. Kurganov and G. Petrova. A third-order semi-discrete genuinely multidimensional central scheme for hyperbolic conservation laws and related problems. *Numer. Math.*, 88(4):683–729, 2001.
- [48] A. Kurganov and G. Petrova. Central-upwind schemes on triangular grids for hyperbolic systems of conservation laws. *Numer. Methods Partial Differential Equations*, 21:536–552, 2005.
- [49] A. Kurganov and G. Petrova. Adaptive central-upwind schemes for Hamilton-Jacobi equations with nonconvex hamiltonians. *J. Sci. Comput.*, 27:323–333, 2006.
- [50] A. Kurganov and G. Petrova. A second-order well-balanced positivity preserving central-upwind scheme for the Saint-Venant system. *Commun. Math. Sci.*, 5:133–160, 2007.
- [51] A. Kurganov and G. Petrova. A central-upwind scheme for nonlinear water waves generated by submarine landslides. In S. Benzoni-Gavage and D. Serre, editors, *Hyperbolic problems: theory, numerics, applications (Lyon 2006)*, pages 635–642. Springer, 2008.
- [52] A. Kurganov, G. Petrova, and B. Popov. Adaptive semi-discrete central-upwind schemes for nonconvex hyperbolic conservation laws. *SIAM J. Sci. Comput.*, 29:2381–2401, 2007.
- [53] A. Kurganov and E. Tadmor. New high resolution central schemes for nonlinear conservation laws and convection-diffusion equations. *J. Comput. Phys.*, 160:241–282, 2000.
- [54] A. Kurganov and E. Tadmor. New high-resolution semi-discrete central scheme for Hamilton-Jacobi equations. *J. Comput. Phys.*, 160:720–742, 2000.
- [55] A. Kurganov and E. Tadmor. Solution of two-dimensional riemann problems for gas dynamics without riemann problem solvers. *Numer. Methods Partial Differential Equations*, 18:584–608, 2002.

- [56] P. D. Lax. Weak solutions of nonlinear hyperbolic equations and their numerical computation. *Comm. Pure Appl. Math.*, 7:159–193, 1954.
- [57] P. G. LeFloch and M. D. Thanh. A Godunov-type method for the shallow water equations with discontinuous topography in the resonant regime. *Journal of Computational Physics*, 230:7631–7660, 2011.
- [58] R. J. LeVeque. Balancing source terms and flux gradients in high-resolution Godunov methods: the quasi-steady wave-propagation algorithm. *J. Comput. Phys.*, 146(1):346–365, 1998.
- [59] R. J. LeVeque. *Finite volume methods for hyperbolic problems*. Cambridge Texts in Applied Mathematics. Cambridge University Press, Cambridge, 2002.
- [60] D. Levy, G. Puppo, and G. Russo. Central WENO schemes for hyperbolic systems of conservation laws. *M2AN Math. Model. Numer. Anal.*, 33(3):547–571, 1999.
- [61] D. Levy, G. Puppo, and G. Russo. Compact central WENO schemes for multidimensional conservation laws. *SIAM J. Sci. Comput.*, 22(2):656–672 (electronic), 2000.
- [62] K. A. Lie and S. Noelle. An improved quadrature rule for the flux-computation in staggered central difference schemes in multidimensions. *J. Sci. Comput.*, 63:1539–1560, 2003.
- [63] K. A. Lie and S. Noelle. On the artificial compression method for second-order nonoscillatory central difference schemes for systems of conservation laws. *SIAM J. Sci. Comput.*, 24(4):1157–1174, 2003.
- [64] S. F. Liotta, V. Romano, and G. Russo. Central schemes for balance laws of relaxation type. *SIAM J. Numer. Anal.*, 38:1337–1356, 2000.
- [65] X. D. Liu and E. Tadmor. Third order nonoscillatory central scheme for hyperbolic conservation laws. *Numer. Math.*, 79(3):397–425, 1998.

- [66] R. Fernandez Luque and R. Van Beek. Erosion and transport of bed-load sediment. *Journal of Hydraulic Research*, 14(2):127–144, 1976.
- [67] E. Meyer-Peter and R. Müller. Formulas for bed-load transport. In *Proceedings of the 2nd Meeting of the International Association for Hydraulic Structures Research*, pages 39–64. Stockholm, 1948.
- [68] H. Nessyahu and E. Tadmor. Nonoscillatory central differencing for hyperbolic conservation laws. *J. Comput. Phys.*, 87(2):408–463, 1990.
- [69] P. Nielsen. *Coastal bottom boundary layers and sediment transport*, volume 4. World Scientific, 1992.
- [70] S. Noelle, Y. Xing, and C.-W. Shu. High-order well-balanced schemes. In *Numerical methods for balance laws*, volume 24 of *Quad. Mat.*, pages 1–66. Dept. Math., Seconda Univ. Napoli, Caserta, 2009.
- [71] L. Pareschi. Central differencing based numerical schemes for hyperbolic conservation laws with relaxation terms. *SIAM J. Numer. Anal.*, 39:1395–1417, 2001.
- [72] L. Pareschi, G. Puppo, and G. Russo. Central Runge-Kutta schemes for conservation laws. *SIAM J. Sci. Comput.*, 26(3):979–999 (electronic), 2005.
- [73] N. Perdreau and J.A. Cunge. Sedimentation dans les estuaries et les embouchures bouchonno marin et bouchin fluvial. Paris, 1971. I.A.H.R. International Seminar on Hydraulics of Alluvial Streams.
- [74] B. Perthame and C. Simeoni. A kinetic scheme for the Saint-Venant system with a source term. *Calcolo*, 38(4):201–231, 2001.
- [75] David Pritchard and Andrew J. Hogg. On the transport of suspended sediment by a swash event on a plane beach. *Coastal Engineering*, 52(1):1–23, 2005.

- [76] M. Ricchiuto and A. Bollermann. Stabilized residual distribution for shallow water simulations. *J. Comput. Phys.*, 228(4):1071–1115, 2009.
- [77] G. Russo and A. Khe. High order well-balanced schemes based on numerical reconstruction of the equilibrium variables. In *Proceedings “WASCOM 2009” 15th Conference on Waves and Stability in Continuous Media*, pages 230–241. World Sci. Publ., Hackensack, NJ, 2010.
- [78] C.-W. Shu. Essentially non-oscillatory and weighted essentially non-oscillatory schemes for hyperbolic conservation laws. In *Advanced numerical approximation of nonlinear hyperbolic equations (Cetraro, 1997)*, volume 1697 of *Lecture Notes in Math.*, pages 325–432. Springer, Berlin, 1998.
- [79] R. Soulsby. *Dynamics of Marine Sands*. Thomas Telford Publications, 1997.
- [80] M.R. Spiegel and J. Liu. *Mathematical Handbook of Formulas and Tables*. Schaum’s Outline Series. McGraw-Hill, second edition, 1999.
- [81] G. Strang. On the construction and comparison of difference schemes. *SIAM J. Numer. Anal.*, 5:506–517, 1968.
- [82] P. K. Sweby. High resolution schemes using flux limiters for hyperbolic conservation laws. *SIAM J. Numer. Anal.*, 21(5):995–1011, 1984.
- [83] P.A. Tassi, S. Rhebergen, C.A. Vionneth, and O. Bokhove. A discontinuous galerkin finite element model for river bed evolution under shallow flows. *CMAME*, 197((33-40)):2930–2947, 2008.
- [84] E. F. Toro. *Riemann solvers and numerical methods for fluid dynamics: A practical introduction*. Springer-Verlag, Berlin, Heidelberg, third edition, 2009.
- [85] B. van Leer. Towards the ultimate conservative difference scheme. V. A second-order sequel to Godunov’s method. *J. Comput. Phys.*, 32(1):101–136, 1979.

- [86] H.J. De Vriend. 2dh mathematical modelling of morphological evolutions in shallow water. *Coastal Engineering*, 11:1–27, 1987.
- [87] Y. Xing, C. W. Shu, and S. Noelle. On the advantage of well-balanced schemes for moving-water equilibria of the shallow water equations. *J. Sci. Comput.*, 48(1-3):339–349, 2011.

APPENDICES

Appendix A

Third Order Strong Stability Preserving Runge Kutta Method

In this appendix we discuss a third order Strong Stability Preserving Runge Kutta (SSP-RK3) method from [29].

We start by considering the following 1-D semi-discrete system of ordinary differential equations given by

$$\frac{d}{dt} \bar{\mathbf{U}}_j = -\frac{\mathbf{H}_{j+\frac{1}{2}} - \mathbf{H}_{j-\frac{1}{2}}}{\Delta x} + \mathbf{S}_j, \quad (\text{A.1})$$

where \mathbf{U} is a vector of unknowns, \mathbf{H} are numerical fluxes, \mathbf{S} are the source terms, and $j = 1 \dots n$ corresponds to the cells in the computational domain. We start by rewriting the right hand side of (A.1) such that

$$\mathcal{L} [\bar{\mathbf{U}}_j]_j := -\frac{\mathbf{H}_{j+\frac{1}{2}} - \mathbf{H}_{j-\frac{1}{2}}}{\Delta x} + \mathbf{S}_j.$$

The SSP-RK3 procedure, which entails evolving the system as a convex combination of forward Euler steps, is given by

$$\begin{aligned} \mathbf{U}_j^I &= \bar{\mathbf{U}}_j(t) + \Delta t \mathcal{L} [\bar{\mathbf{U}}_j(t)]_j, \\ \mathbf{U}_j^{II} &= \frac{3}{4} \bar{\mathbf{U}}_j(t) + \frac{1}{4} \left(\bar{\mathbf{U}}_j^{(I)}(t) + \Delta t \mathcal{L} [\bar{\mathbf{U}}_j^I(t)]_j \right), \\ \mathbf{U}_j^{III} &= \frac{1}{3} \bar{\mathbf{U}}_j(t) + \frac{2}{3} \left(\bar{\mathbf{U}}_j^{(II)}(t) + \Delta t \mathcal{L} [\bar{\mathbf{U}}_j^{II}(t)]_j \right), \\ \bar{\mathbf{U}}_j(t + \Delta t) &= \bar{\mathbf{U}}_j^{III}, \end{aligned}$$

Now consider the 2-D semi-discrete system of ordinary differential equations given by

$$\frac{d}{dt} \bar{\mathbf{U}}_{j,k} = - \frac{\mathbf{H}_{j+\frac{1}{2},k}^x - \mathbf{H}_{j-\frac{1}{2},k}^x}{\Delta x} - \frac{\mathbf{H}_{j,k+\frac{1}{2}}^y - \mathbf{H}_{j,k-\frac{1}{2}}^y}{\Delta y} + \mathbf{S}_{j,k}, \quad (\text{A.2})$$

where \mathbf{U} is a vector of unknowns, \mathbf{H}^x are numerical fluxes in the x -direction, \mathbf{H}^y are numerical fluxes in the y -direction, \mathbf{S} are the source terms, and $j = 1, \dots, n$, $k = 1, \dots, m$ corresponds to the cells in the computational domain. To solve start by rewriting the right hand side of (A.2) such that

$$\mathcal{L} [\bar{\mathbf{U}}_{j,k}]_{j,k} := - \frac{\mathbf{H}_{j+\frac{1}{2},k}^x - \mathbf{H}_{j-\frac{1}{2},k}^x}{\Delta x} - \frac{\mathbf{H}_{j,k+\frac{1}{2}}^y - \mathbf{H}_{j,k-\frac{1}{2}}^y}{\Delta y} + \mathbf{S}_{j,k}.$$

The SSP-RK3 procedure, which entails evolving the system as a convex combination of forward Euler steps, is given by

$$\begin{aligned} \mathbf{U}_{j,k}^I &= \bar{\mathbf{U}}_{j,k}(t) + \Delta t \mathcal{L} [\bar{\mathbf{U}}_{j,k}(t)]_j, \\ \mathbf{U}_{j,k}^{II} &= \frac{3}{4} \bar{\mathbf{U}}_{j,k}(t) + \frac{1}{4} \left(\bar{\mathbf{U}}_{j,k}^{(I)}(t) + \Delta t \mathcal{L} [\bar{\mathbf{U}}_{j,k}^I(t)]_j \right), \\ \mathbf{U}_{j,k}^{III} &= \frac{1}{3} \bar{\mathbf{U}}_{j,k}(t) + \frac{2}{3} \left(\bar{\mathbf{U}}_{j,k}^{(II)}(t) + \Delta t \mathcal{L} [\bar{\mathbf{U}}_{j,k}^{II}(t)]_{j,k} \right), \\ \bar{\mathbf{U}}_{j,k}(t + \Delta t) &= \bar{\mathbf{U}}_{j,k}^{III}. \end{aligned}$$

Appendix B

Adaptive Time Step Strategy

In this appendix we discuss the implementation of an adaptive time step strategy from [14] that modifies the SSP-RK3 method described in Appendix A.

We consider the time step restriction for the 1-D system given by

$$\Delta t \leq \min \left\{ \frac{\Delta x}{2 \max_i |\lambda^{(i)}|} \right\}, \quad (\text{B.1})$$

where i is the number of eigenvalues λ for the Jacobian of the flux. The procedure for the adaptive time step strategy is then given by the following:

1. Given the solution $\bar{\mathbf{U}}(t)$, set $\Delta t := \kappa(\Delta t)_*$, where $\kappa \in (0, 1)$ and $(\Delta t)_*$ is given by (B.1);
2. Use Δt to compute $\bar{\mathbf{U}}^I$;
3. Given the intermediate solution $\bar{\mathbf{U}}^I$, compute $(\Delta t)_*^I$ using (B.1);
4. If $(\Delta t)_*^I < \Delta t$, set $\Delta t := \kappa(\Delta t)_*^I$ and go back to Step 2;
5. Use Δt to compute $\bar{\mathbf{U}}^{II}$;
6. Given the intermediate solution $\bar{\mathbf{U}}^{II}$, compute $(\Delta t)_*^{II}$ using (B.1);
7. If $(\Delta t)_*^{II} < \Delta t$, set $\Delta t := \kappa(\Delta t)_*^{II}$ and go back to Step 2;
8. Use Δt to compute $\bar{\mathbf{U}}^{III}$ and $\bar{\mathbf{U}}(t + \Delta t)$.

In two dimensions we consider the time restriction for the 2-D system given by

$$\Delta t \leq \min \left\{ \frac{\Delta x}{4 \max_i |\lambda^{(i)}|}, \frac{\Delta y}{4 \max_j |\mu^{(j)}|} \right\}, \quad (\text{B.2})$$

where i is the number of eigenvalues λ , for the Jacobian of the flux in the x -direction and j is the number of eigenvalues μ for the Jacobian of the flux in the y -direction. The procedure for the adaptive time step strategy is then given by the following:

1. Given the solution $\bar{\mathbf{U}}(t)$, set $\Delta t := \kappa(\Delta t)_*$, where $\kappa \in (0, 1)$ and $(\Delta t)_*$ is given by (B.2);
2. Use Δt to compute $\bar{\mathbf{U}}^I$;
3. Given the intermediate solution $\bar{\mathbf{U}}^I$, compute $(\Delta t)_*^I$ using (B.2);
4. If $(\Delta t)_*^I < \Delta t$, set $\Delta t := \kappa(\Delta t)_*^I$ and go back to Step 2;
5. Use Δt to compute $\bar{\mathbf{U}}^{II}$;
6. Given the intermediate solution $\bar{\mathbf{U}}^{II}$, compute $(\Delta t)_*^{II}$ using (B.2);
7. If $(\Delta t)_*^{II} < \Delta t$, set $\Delta t := \kappa(\Delta t)_*^{II}$ and go back to Step 2;
8. Use Δt to compute $\bar{\mathbf{U}}^{III}$ and $\bar{\mathbf{U}}(t + \Delta t)$.